TECHNICKÁ UNIVERZITA V LIBERCI
Fakulta mechatroniky, informatiky
a mezioborových studií

Depth-resolved quantitative phase imaging using lensfree interferometric microscopy

Diplomová práce

Studijní program: N3942 – Nanotechnologie
Studijní obor: 3942T002 – Nanomateriály

Autor práce: **Bc. Matěj Hejda**
Vedoucí práce: prof. Ing. Pavel Mokrý, Ph.D.
Konzultant: Luc Dümpelmann, Ph.D.

Liberec 2019

Technická univerzita v Liberci
Fakulta mechatroniky, informatiky a mezioborových studií
Akademický rok: **2018/2019**

ZADÁNÍ DIPLOMOVÉ PRÁCE

(PROJEKTU, UMĚLECKÉHO DÍLA, UMĚLECKÉHO VÝKONU)

Jméno a příjmení:	**Bc. Matěj Hejda**
Osobní číslo:	**M16000159**
Studijní program:	**N3942 Nanotechnologie**
Studijní obor:	**Nanomateriály**
Název tématu:	**Depth-resolved quantitative phase imaging using lensfree interferometric microscopy**
Zadávající katedra:	**Ústav mechatroniky a technické informatiky**

Zásady pro vypracování:

1. Study and review literature in related fields such as lensfree microscopy, digital holography and image processing.
2. Build compact LIM setup; verify, test and assess optimal parameters of the setup.
3. Perform, analyze and evaluate 2D measurements on weakly scattering structures using the LIM.
4. Assess the possibility of acquiring structure depth information with the LIM setup.

Rozsah grafických prací:	**dle potřeby dokumentace**
Rozsah pracovní zprávy:	**40–50 stran**
Forma zpracování diplomové práce:	**tištěná/elektronická**
Jazyk zpracování diplomové práce:	**Angličtina**

Seznam odborné literatury:

[1] **FIALA, Pavel a Ivan RICHTER, 2004. Fourierovská optika a optické zpracování signálů. Praha: Vydavatelství ČVUT. ISBN 978-80-01-02895-7.**

[2] **TERBORG, R. A.; PELLO, J.; MANNELLI, I.; TORRES, J. P.; PRUNERI, V. Ultrasensitive interferometric on-chip microscopy of transparent objects. Science Advances. 2016, vol. 2, no. 6, pp. e1600077.**

[3] **ISIKMAN, S. O.; BISHARA, W.; MAVANDADI, S.; YU, F. W.; FENG, S.; LAU, R.; OZCAN, A. Lens-free optical tomographic microscope with a large imaging volume on a chip. Proceedings of the National Academy of Sciences. 2011, vol. 108, no. 18, pp. 7296.**

[4] **SU, T.-W.; XUE, L.; OZCAN, A. High-throughput lensfree 3D tracking of human sperms reveals rare statistics of helical trajectories. Proceedings of the National Academy of Sciences. 2012, vol. 109, no. 40, pp. 16018.**

Vedoucí diplomové práce:	**prof. Ing. Pavel Mokrý, Ph.D.**
	Ústav mechatroniky a technické informatiky
Konzultant diplomové práce:	**Luc Dümpelmann, Ph.D.**
	ICFO - The Institute of Photonic Sciences, Barcelona

Datum zadání diplomové práce:	**10. října 2018**
Termín odevzdání diplomové práce:	**30. dubna 2019**

L.S.

prof. Ing. Zdeněk Plíva, Ph.D.
děkan

doc. Ing. Milan Kolář, CSc.
vedoucí ústavu

V Liberci dne 10. října 2018

Prohlášení

Byl jsem seznámen s tím, že na mou diplomovou práci se plně vztahuje zákon č. 121/2000 Sb., o právu autorském, zejména § 60 – školní dílo.

Beru na vědomí, že Technická univerzita v Liberci (TUL) nezasahuje do mých autorských práv užitím mé diplomové práce pro vnitřní potřebu TUL.

Užiji-li diplomovou práci nebo poskytnu-li licenci k jejímu využití, jsem si vědom povinnosti informovat o této skutečnosti TUL; v tomto případě má TUL právo ode mne požadovat úhradu nákladů, které vynaložila na vytvoření díla, až do jejich skutečné výše.

Diplomovou práci jsem vypracoval samostatně s použitím uvedené literatury a na základě konzultací s vedoucím mé diplomové práce a konzultantem.

Současně čestně prohlašuji, že tištěná verze práce se shoduje s elektronickou verzí, vloženou do IS STAG.

Datum:

Podpis:

Hloubkově rozlišené kvantitativní fázové zobrazování pomocí bezobjektivové interferometrické mikroskopie

Abstrakt

Schopnost zkoumat slabě rozptylující vzorky je klíčová například pro odvětví zabývající se studiem buněk nebo optickou analýzou povrchů. Tyto tzv. fázové objekty však neprodukují dostatečný signál na to, aby mohly být zobrazovány pomocí klasické optické mikroskopie. Řešením tohoto problému je využití interferometrie. Bezobjektivový interferometrický mikroskop (LIM) je zařízením, které využívá dvojlomných krystalů a částečně koherentních, kolimovaných zdrojů světla ke zkoumání plošného rozložení indexu lomu ve vzorcích s vysokým axiálním rozlišením. Schopnost získat informace o třírozměrném rozložení fázových objektů v objemu vzorku by umožnila využití tohoto mikroskopu v nových vědeckých i průmyslových odvětvích, například biomedicínském zobrazování, datových úložištích na bázi skla nebo monitorování defektů v optických elementech.

Tato diplomová práce se zabývá rozšířením funkčnosti bezobjektivového interferometrického mikroskopu do oblasti tomografického zobrazování. Toho je dosaženo realizací hloubkového rozlišování pro fázové objekty ve zkoumaných vzorcích. Pro umožnění měření byl sestaven prototyp mikroskopu a ověřen vliv různých parametrů optického uspořádání na kvalitu pořízeného obrazu. Současně byla navržena nová metoda k získání nakloněného, kolimovaného osvětlení. Kombinací několika úhlů osvitu a následného algoritmického zpracování získaných dat byly pořízeny kvantitativní fázové snímky se zorným polem 35 mm^2, plošným rozlišením $\sim$ 10 μm a axiálním rozlišením menším než 1 nm. Následně bylo navrženo několik metod umožňujících hloubkové rozlišování zobrazovaných objektů. Tyto postupy, využívající nakloněného osvitu a numerické propagace optického pole, byly implementovány a ověřeny měřením na vícevrstvých vzorcích. Nejlepší výsledky byly získány pomocí metody *backpropagated pixel-by-pixel verification* (β-PbP). Tato nově navržená metoda byla úspěšně využita pro třírozměrnou rekonstrukci rozložení fázových objektů ve vzorcích objemu $V \approx 0.5\ cm^3$ s axiální přesností menší než 1 mm. Společně s ostatními navrženými metodami se jedná o první demonstraci využití LIM jako tomografické zobrazovací techniky.

Klíčová slova: bezobjektivová interferometrická mikroskopie, kvantitativní fázové zobrazování, hloubkové rozlišování, třírozměrné zobrazování

Depth-resolved quantitative phase imaging using lensfree interferometric microscopy

Abstract

Examining of weakly scattering transparent structures is highly desirable especially in areas such as cell imaging and quality control of transparent surfaces. However, such structures can not be efficiently imaged in conventional light microscopes due to low scattering signal. To measure such structures, techniques such as interferometry are more suitable. The lensfree interferometric microscope (LIM) is a compact device that utilizes birefringent crystals and partially coherent collimated light beams to acquire information about refractive index distribution of planar samples with sub-nanometer precision. Extending the phase imaging ability of such device from two to three dimensions would allow multitude of new applications across various research and industrial fields including biomedical imaging, physical data storage systems, defect mapping in glasses or holographic security element validation.

This thesis focuses on expanding the measurement capabilities of the LIM device into the field of tomographical imaging by enabling depth resolving of transparent (phase) objects. First, an overview of the LIM, its design and related computational methods is provided. The microscope prototype was built, all the optical setup parameters were assessed and the influence of different components was evaluated, laying the foundation for further development of commercial prototypes. To emphasize the potential for a point-of-care portable device, all the hardware controls and data processing were implemented on a single-board computer. Simultaneously, a novel solution to obtain different illumination angles was proposed using multicore optical fiber bundle. Utilizing a combination of the multiple illumination angles and computational post-processing, phase maps were reconstructed across a field-of-view of 35 mm^2 with spatial resolution of $\sim$ 10 μm and axial resolution in the sub-nanometer region. To enable depth resolving, multiple techniques were proposed for the LIM, taking advantage of both digital holographic refocusing and the angled illumination. These proposed methods were verified by measuring real, custom-made multilayered transparent samples. The best results were obtained by a self-developed algorithm named *backpropagated pixel-by-pixel verification* (β-PbP). This new method enables layer-by-layer phase map reconstruction in the sample volume $V \approx 0.5\ cm^3$ with axial accuracy of for preliminary results being below 1 mm. Together with the other introduced techniques, this demonstrates the first proof-of-concept of using the LIM for tomographical imaging.

Keywords: lensfree interferometric microscopy, quantitative phase imaging, depth resolving, three-dimensional imaging

Acknowledgements

This thesis would never come into existence just by the means of my own work. The LIM (lensfree interferometric microscope) is a result of collective scientific endeavour, and the same applies to the process of further developing it. Hence, I want to express my immense gratitude to all of the people who helped me in the process of making and finishing this thesis.

At the foremost, I would like to thank **Prof. Valerio Pruneri** for accepting me as a visiting student to his *Optoelectronics* group at the *Institute of Photonics Sciences* (ICFO) in Barcelona, and for later allowing me to extended my stay there to conduct this thesis while also helping me as a supervisor. Special thanks then go mainly to my LIM team:

- to **Luc Dümpelmann** for being both a great friend and excellent mentor that provided me with thesis guidance, valuable insights and endless energy and motivation to push our research forward;
- to **Roland Terborg**, whom I thank for more than the space here allows me to mention, particularly: for being a wonderful friend, for sparking my interest in this research field, for introducing me to ICFO, for never missing a chance to have a laugh together and for always being willing to answer my pressing questions about the LIM and then have a cold cerveza afterwards.

Sincere thanks also go to **Alican Mehmet Noyan**, **Vittoria Finazzi** and **Nestor Bareza** for their precious help in sample preparation. At the same time, many thanks also go to the rest of the *Optoelectronics* group, as my stay in Barcelona would surely not be such a memorable experience if I were a member of a different ICFO group.

I would also like to thank to **prof. Ing. Pavel Mokrý, Ph.D.** for his help in organizing the collaboration between TUL and ICFO and being the supervisor at the side of the university. Last but not least, my most profound thanks go to **my family** and **my girlfriend**. Despite the fact that I spent most of my Master thesis time far away from them, their continuous support and belief in me always gave me the strength and helped me to keep on moving forward, even in the most challenging times.

Contents

List of used abbreviations and symbols

A.D.	anno Domini
2D	two dimensional
3D	three dimensional
AFM	atomic force microscopy
AR	antireflective (coating)
B	blue
B_i	BRIEF descriptor
BRIEF	Binary Robust Independent Elementary Features
B/W	black and white
β-PbP	backpropagated pixel-by-pixel verification method
CAM	camera
CMOS	complementary metal–oxide semiconductor
CNC	computer numerical control
COLL	collimator
c	speed of light
DC	direct current
d	distance
d_H	Hamming distance
d_{pix}	pixel size
d_{SP}	Savart plate thickness
$\mathcal{D}$	sampling distance of a function
δ	object (frame) displacement
Δ''	second derivative of function describing map difference
$\hat{\Delta}$	normalized function describing map difference
$\varnothing$	diameter
E_0	amplitude of electromagnetic wave
FFT	Fast Fourier transform
FoV	field-of-view
FPS	frames-per-second
F	focal length
f_{NX}	Nyquist frequency
$\mathcal{F}$, $\mathcal{F}^{-1}$	Fourier transform, inverse Fourier transform
f_x, f_y	coordinates in frequency space
GUI	graphical user interface
G	green
$\gamma(\vec{r}, t+\tau)$	normalized temporal correlation function
$\Gamma(\vec{r}, t+\tau))$	temporal correlation function
h	object thickness
$h(x, y)$	impulse function
$\mathcal{H}(f_X, f_Y)$	transfer function
$\vec{k}$, k	wavevector, wavenumber
κ	distance-to-displacement proportionality constant

LED	light emmiting diode
l_c	coherence length
λ	wavelength
λ_0	central wavelength of a source
Δ	difference (general meaning)
$\Delta\lambda$	full-width half maximum of a source
$\Lambda(\vec{\rho}, \tau)$	spatiotemporal coherence function
ICFO	Institute of Photonic Sciences
iFFT	inverse Fast Fourier transform
I	light intensity (irradiance)
$\mathfrak{I}$	imaginary part of a complex number
LFM	lensfree microscopy
LIM	lensfree interferometric microscope
MZI	Mach-Zehnder interferometer
M, N	number of samples in discrete sampled function
μ	mean value of a set
NA	numerical aperture
n	refractive index; numbering index
n_c	number of acquired frames
OTF	optical transfer function
O	object wave electric field
PbP	pixel-by-pixel verification method
PSDH	Phase-shifting digital holography
PSI	Phase-shifting interferometry
PSR	pixel super resolution
P1, **P2**	polarizers
p	pixel value
p_{pol}, p_{Sx}, p_{Sx}	electric field projections (in simulations)
ψ	phase difference between waves (Savart plate induced)
$\Psi_{\sin}$, $\Psi_{\cos}$	phase-shifting integrals
QPI	quantitative phase imaging
φ	phase
R	red
RFL	reflected focal length
r_{12}	distance between investigated points (in diffraction integral)
$\Re$	real part of complex number
$\mathbb{R}$	set of real numbers
R	reference wave electric field
$\vec{r}$	vector of position
$\vec{\rho}$	increment of position
SP1	upper Savart plate
SP2	lower Savart plate
s/n	signal-to-noise ratio
s	Savart plate shearing distance
S(X,Y)	image processed with the Sobel filter

σ	standard deviation
σ^2	variance
T	transmittance; threshold
t	time
τ	increment of time
τ_c	correlation time
θ	optical element rotation; beam angle
U	complex amplitude
ω	angular frequency
Ω	integration area
$W(\vec{\rho}, t)$	spatial correlation function
x, y	position (in real space)
X, Y	position (in discrete space)
χ	distance between projections; projected hexagon size
z_f	focus distance
z, z_p	propagation distance
Z	light source to camera distance
Z_0	free space impedance
Z_1	light source-sample distance
Z_2	sample-camera distance
Z_{SP}	distance between Savart plates

1 Introduction

The desire to examine objects smaller than what our eyes can see has been around for as long as mankind itself. Already in the first century A.D., the roman philosopher Seneca described how handwritten letters can be magnified by the use of glass sphere filled with water [1]. Later, approximately in the 13th century, the first modern optical systems - the reading glasses - were designed in the Italian city of Florence. It didn't take long for reading glasses to become a widespread tool improving life quality for many people. Simultaneously, the science of optics became of interest for the philosophers who started noticing how combining various glasses (optical lenses) can yield unexpected behavior of light. The first optical microscope (combining at least two lenses) is generally attributed to Dutch optician Zacharias Jansen (1588-1632) [1]. Conventional lens-based optical microscopy, which is based on contrast formed by light being absorbed by the sample, since then proved to be an indispensable tool for scientists, industrial researches and medical personnel. However, since the contrast in those is based on amplitude attenuation, very thin or weakly scattering and absorbing objects are difficult to properly image with such devices. One of the common approaches for imaging e.g. cells in biology is by staining with fluorescent dyes and imaging the signal produced while exciting the dye. The use of dyes unfortunately involves additional preparation work and the dyes can have negative effect on the cells and their viability.

While weakly scattering and absorbing structures do not produce significant signal by modulating the intensity of light, they introduce phase shifts to the light traveling through them due to having different refractive index. For this reason, they can also be called *phase objects*. Unfortunately, all known photodetectors respond only to light intensity $I \propto E^2$ and not the phase φ of the light fields (the actual phase of the field varies extremely fast, at the scale of femtoseconds for visible light) [2]. For this reason, information about phase can be accessed only by the means of phase **difference** measurements between two interfering fields using techniques such as interferometry or holography.

Nowadays, we live in an age of unprecedented technological advancement. Cheap computing power has become widely spread and available in the form of smartphones and personal computers, while complementary metal–oxide semiconductor (CMOS) photodetectors (driven by the smartphone camera market) became simultaneously very efficient and significantly cheaper due to mass production [3]. Combination of these two factors led to the inception of a new field of *lensfree microscopy*, where the ocular lens is replaced by a digital camera and the objective lens is replaced by numerical algorithms. Lensfree microscopes bring many interesting advantages to the field of microscopy (like utilization of holographic contrast) while offering significantly reduced form factor (in comparison to the lens-based microscopes).

1.1 Thesis outline

In this Master thesis, I focus on reviewing, building, measuring on and expanding the functionality of the *lensfree interferometric microscope* (LIM), a device based on the concept of the lensfree microscope. My main goal is to enable depth resolving for phase objects with the LIM by combining hardware modifications to the setup and data post-processing. Knowledge of three-dimensional distribution of phase objects in transparent samples can open the doors towards modern solid-state glass-based data storage methods, enable industrial optics manufacturers to precisely detect and localize spatial defects in transparent specimen (such as lenses), give information of cell movements and mobility over time, or enable rapid detection of biomolecules attached to antibody-modified substrates by measuring multiple stacked samples simultaneously.

In **Chapter 2**, I introduce some general concepts from physics, optics and imaging that are necessary to properly explain methods and approaches used in the following chapters.

In **Chapter 3**, I describe a specific modification of the LFM called lensfree interferometric microscope (LIM). This device was developed by members of the *Optoelectronics* group (V. Pruneri) at ICFO and is the main device used and further developed in this thesis.

In **Chapter 4**, I discuss building of the LIM, and various setup parameter optimization. I also introduce some new functionality to improve the performance in terms of two-dimensional imaging. Standard resolution target measurements are then conducted to assess the imaging performance.

In the final **Chapter 5**, I propose multiple methods on how to enable object depth resolving with the LIM. I test the methods on simulated and real datasets and evaluate the results.

Chapters 2 and 3 serve to review scientific fundamentals, state-of-the-art and current landscape of the technology. Therefore they are based on results of other researchers. The following chapters 4 and 5 are mainly based on my own research, experiments and results.

1.2 Contributions

This thesis relies and builds on the previous work of my colleagues from the *Optoelectronic* (Prof. Valerio Pruneri) group at ICFO. Hence, the work of other researchers is used in some of the chapters. Namely, these contributions from others include:

- the complete software package of the LIM, including implementation of the phase-shifting interferometry algorithm and user interface (GUI), which was done by Dr. Roland A. Terborg, Dr. Josselin Pello and other members within the European Union's Horizon 2020 research and innovation program under grant agreement no. 644956 (RAIS Project);
- the twin image suppression approach, which was proposed by Dr. Roland A. Terborg;
- the simulated optical elements, described in Sec. 3.5, which were implemented by Dr. Roland A. Terborg;
- the robust autofocusing method described in Sec. 4.4, which was proposed and implemented by Dr. Roland A. Terborg,
- all the measured transparent samples (dot arrays and resolution targets), which were fabricated and prepared by Dr. Alican Mehmet Noyan, Dr. Vittoria Finazzi and Nestor Bareza;
- the 3D renders (Fig. 4.4, Fig. 5.1) and final design of the hardware enclosure for the LIM prototype, which were made by Dr. Luc Dümpelmann.

2 Selected chapters from optics and imaging

In this introductory chapter, some general concepts from the fields of optics, holography and image processing are introduced. The goal of this is to give foundation and description to methods and approaches used throughout the thesis.

2.1 Nature and coherence of light

Light is a form of transverse electromagnetic radiation. To represent general electromagnetic radiation, ranging from γ-rays and X-rays to microwaves, two distinctive physical models can be utilized: **(i)** particle model, where electromagnetic radiation is assumed to propagate by the means of elementary particles called photons, and **(ii)** wave model, where light is described by the means of propagating electromagnetic field disturbance. Each of these approaches describes light in specific situations and effects, such as Compton's or photoelectric effect (particle-like character) and interference, diffraction or Doppler's effect (wave-like character). This is why light is described as exhibiting *wave-particle dualism*. In this thesis, the wave-like character of light is the key concept that enables the proposed microscopy techniques. Since light is a specific form of general electromagnetic radiation, it is fully described by Maxwell's equations. From these, the wave equation can be derived. The simplest solution to the wave equation is a planar wave, usually described by the electric field $\vec{E}(\vec{r},t)$:

$$\vec{E}(\vec{r},t) = E_0 \cos(\vec{k}\cdot\vec{r} - \omega t) \tag{2.1}$$

where E_0 is the wave amplitude, ω is the angular temporal frequency and $\vec{k}$ is the wave vector For practical reasons, it's common to instead use the so-called *complex amplitude* $U(\vec{r},t)$:

$$U(\vec{r},t) = E_0 e^{i(\vec{k}\cdot\vec{r}-\omega t)} \tag{2.2}$$

such that

$$\vec{E}(\vec{r},t) = \Re(U(\vec{r},t)) \tag{2.3}$$

where $\Re(\dots)$ represents a real-part of complex valued function.

The exponent $(\vec{k}\cdot\vec{r}-\omega t)$ is the *phase* φ of a given wave:

$$\varphi = \vec{k}\cdot\vec{r} - \omega t \tag{2.4}$$

Since Maxwell's equations are linear, the superposition principle says that for any two solutions $\vec{E}_1(\vec{r},t)$ and $\vec{E}_2(\vec{r},t)$ to the wave equation, their linear combination $\alpha\vec{E}_1(\vec{r},t) + \beta\vec{E}_2(\vec{r},t)$, where $\alpha, \beta in\mathbb{R}$ is also a solution to the wave equation. This principle is essential to describe the phenomena of light interference.

Interference refers to the effect when the superposition of multiple waves causes redistribution of energy. Whenever any experiment is performed based on a superposition of light fields, the outcome of the averaging performed by a photodetector is strongly dependent on how the waves hold their properties over some propagation distance. This behavior is described by the theory of *coherence*. An ideal monochromatic planar wave would have infinite coherence length and time, however, such waves can not exist due to the existence of fluctuations in the real light sources [2].

To quantify the wave coherence, two autocorrelation functions are introduced. The first function is called *spatial correlation function* (denoted $W(\vec{\rho},t)$) and relates the behavior of a wave $\vec{E}(\vec{r},t)$ to its spatially shifted version $\vec{E}(\vec{r}+\vec{\rho},t)$ at a specific point in time:

$$W(\vec{\rho},t) = \langle \vec{E}(\vec{r},t) \cdot \vec{E}^*(\vec{r}+\vec{\rho},t) \rangle \tag{2.5}$$

where $\vec{\rho}$ is the spatial shift, * denotes the complex conjugate and angular brackets represent averaging over a set of measurements. Spatial coherence tells us how uniform the phase of a wavefront is.

The second autocorrelation function is called *temporal correlation function* $\Gamma(\vec{r},\tau)$. This function relates the behavior of a wave $\vec{E}(\vec{r},t)$ to its temporally shifted version $\vec{E}(\vec{r},t+\tau)$ at specific point in space:

$$\Gamma(\vec{r},\tau) = \langle \vec{E}(\vec{r},t) \cdot \vec{E}^*(\vec{r},t+\tau) \rangle \tag{2.6}$$

These two functions can be recombined into one *spatiotemporal coherence function* $\Lambda(\vec{\rho},\tau)$:

$$\Lambda(\vec{\rho},\tau) = \langle \vec{E}(\vec{r},t) \cdot \vec{E}^*(\vec{r}+\vec{\rho},t+\tau) \rangle \tag{2.7}$$

In practical terms, the spatial coherence is a measure of the correlation between the phases of a light wave at different points transverse to the direction of propagation. Temporal coherence is a measure of the correlation between the phases of a light wave at different points along the direction of propagation, and is also one of the factors defining the spatial resolution of a holography-based imaging techniques [4, 5]. By normalizing the temporal correlation function $\Gamma(\vec{r},t+\tau)))$ using the light

intensity, the *normalized temporal correlation function* $\gamma(\vec{r}, t+\tau))$ is obtained:

$$\gamma(\vec{r}, t+\tau) = \frac{\langle \vec{E}(\vec{r}, t) \cdot \vec{E}^*(\vec{r}, t+\tau) \rangle}{\langle \vec{E}(\vec{r}, t) \cdot \vec{E}^*(\vec{r}, t) \rangle} \tag{2.8}$$

The absolute value of this function is bound: $0 \leq |\gamma(\vec{r}, t+\tau)| \leq 1$. For real sources, it reaches $|\gamma(\vec{r}, t+\tau)| = 1$ for $\tau = 0$, and gradually decreases to 0 with increasing $|\tau|$. The time for which the wave correlates to a certain extent with it's time-shifted version (for example $|\gamma(\vec{r}, t+\tau)| = 1/2$) is called *correlation time* τ_c. Using the correlation time, a *coherence length* l_c can be defined:

$$l_c = \tau_c \cdot c \tag{2.9}$$

where c is the speed of light. The *coherence length* can be also estimated from the spectral width of the source:

$$l_c \approx \frac{2 \ln 2}{\pi} \frac{\lambda_0}{\Delta\lambda} \tag{2.10}$$

where λ_0 is the central wavelength of the source, $\Delta\lambda$ is the full-width half-maximum spectral bandwidth of the source and n is the refractive index [5].

2.2 Fourier Optics

Fourier optics is a field studying optical phenomena in the frequency spectrum and the transmission of light field's spectral components through optical systems. This is based on the wave nature of light and, unlike simple ray optics, accounts for wave-based phenomena (such as diffraction). Nowadays, computational Fourier optics offer a powerful way of describing and modeling light behavior such as diffraction, coherence, propagation through random media and holography [6].

Essential tool for investigating signals in the frequency domain is the Fourier transform. In the simplest form, a continuous, one-dimensional **Fourier transform** $\mathcal{F}_c\{\}$ of a continuous, periodic function $g(x)$ has a form of another function $G(f)$:

$$\mathcal{F}_c\{g(x)\} = G(f) = \int_{-\infty}^{\infty} g(x) e^{-i2\pi f x} \mathrm{d}x \tag{2.11}$$

Term $e^{-i2\pi f x}$ can be considered a Fourier-specific *kernel* of a generalized integral transform [7]. This formula can be further extended into two-dimensions:

$$\mathcal{F}_c\{g(x,y)\} = G(f_x, f_y) = \iint_{-\infty}^{\infty} g(x,y) e^{-i2\pi(f_x x + f_y y)} \mathrm{d}x\mathrm{d}y \tag{2.12}$$

For digitally sampled function $\tilde{g}(m,n)$ over $M \times N$ sample points, continuity can not be longer assumed and instead, discrete Fourier transform $\mathcal{F}_d\{\}$ is used [6]:

$$\mathcal{F}_d\{\tilde{g}(m,n)\} = \tilde{G}(p,q) = \sum_{m=-M/2}^{M/2-1} \sum_{n=-N/2}^{N/2-1} \tilde{g}(m,n) e^{-i2\pi(\frac{pm}{M}+\frac{qn}{N})} \tag{2.13}$$

One of the interesting properties of the Fourier transform is that a shift of function in the spatial domain equals to multiplication by a linear phase term in the frequency domain. This is described by the *Fourier shift theorem* [6]:

$$\mathcal{F}\{g(x-\Delta x, y-\Delta y)\} = G(f_x, f_y) \cdot e^{-i2\pi(\Delta x f_x + \Delta y f_y)} \tag{2.14}$$

Thanks to the prevalent use of computers for modeling and computations, Fourier optics is closely intertwined with the field of digital signal processing. The most common representation of light fields in computational Fourier optics is in the form of two-dimensional discrete arrays describing the complex amplitude of a real wavefront $U(x,y)$ by $U(X,Y)$, where $(X,Y) \in \mathbb{Z}^2$ denotes the pixel position. Since these arrays are discrete, they are sampled representations of the real (continuous) fields. As such, they are subject to the *Nyquist–Shannon sampling theorem* [8], which gives the relation between the sampling distance (in real space) $\mathcal{D}$ and maximal reconstructed frequency in the Fourier domain $f_{NX} = \frac{1}{2\mathcal{D}}$. Since the sampling distance in digital microscopy is always limited by the camera pixel size d_{pix}, this poses a limit on maximal resolving power of these devices.

As mentioned before, the field of Fourier optics spans a wide array of optical phenomena. One of the main interests of the thesis related to this field lies in the capability of numerically propagating light fields along their propagation direction, enabling digital refocusing of acquired holographic microscope images. This method will be described in more detail in the following section.

2.2.1 Fresnel approximation for scalar diffraction

The ability to describe the evolution of an optical field while it propagates can be regarded as one of the fundamental tasks in Fourier optics. The main focus while describing the propagation is on diffraction. Assuming multiple properties of the environment such as *linearity* (fields from separate sources can be summed), *isotropicity* (behavior independent on polarization), *homogeneity* (permittivity is position independent) and *non-dispersivity* (permittivity is wavelength independent), a simplified theory of *scalar diffraction* can be used [6]. These conditions apply for free space propagation and also for "well-behaved" materials, where scalar diffraction theory provides sufficient approximation to the real situation.

Assuming a monochromatic field represented by a complex amplitude U propagating through an isotropic medium along the z-axis. The state of the complex amplitude

in a specific z plane is thus:

$$U_z(x,y) = E_0(x,y)e^{i\varphi(x,y)} \tag{2.15}$$

A light field source of area Ω can be considered as a set of infinitesimally small point sources, each creating spherical waves. In each point (a,b), the field is thus defined by $U_1(a,b)$ and their collective superposition describes the actual field. To obtain the field $U_2(x,y)$ created by this source in some distant observation plane (parallel to the source plane), the general *Rayleigh-Sommerfield diffraction integral* [8] can be used:

$$U_2(x,y) = \frac{z}{i\lambda}\iint_{\Omega} U_1(a,b)\frac{e^{ikr_{12}}}{r_{12}^2}dadb \tag{2.16}$$

where the distance r_{12} from (a,b) to (x,y) is equal to

$$r_{12} = \sqrt{z^2 + (x-a)^2 + (y-b)^2} \tag{2.17}$$

.

This can be rewritten in the form of a *convolution integral*

$$U_2(x,y) = \frac{z}{i\lambda}\iint_{\Omega} U_1(a,b)h(x-a,y-b)dadb \tag{2.18}$$

.

with the *Rayleigh-Sommerfield impulse function* $h(x,y)$ being defined as:

$$h(x,y) = \frac{z}{i\lambda r}e^{kr} \tag{2.19}$$

where r is the Euclidean distance $r = \sqrt{x^2+y^2+z^2}$. By taking Fourier transform of $h(x,y)$, the convolution operation can be simply written as a multiplication by $\mathcal{H}(f_X, f_Y) = \mathcal{F}\{h(x,y)\}$ in the frequency domain.

The **Fresnel (near-field) approximation** of scalar diffraction simplifies the expression of r_{12}. Assuming

$$\lambda \ll z \tag{2.20}$$

and

$$\frac{\sqrt{(x-a)^2+(y-b)^2}}{z} \ll 1 \tag{2.21}$$

the distance term r_{12} can be approximated using only first two terms of binomial expansion $(x+y)^{1/2} = x^{1/2} + \frac{1}{2}x^{-1/2}y$

$$r_{12} \approx z + \frac{1}{2z}\Big[(x-a)^2 + (y-b)^2\Big] \tag{2.22}$$

By substituting the original term for r_{12} with the approximated one in the denominator of Eq. 2.16, a similar convolution integral is obtained. The Fresnel impulse function [8] is then:

$$h_F(x,y) = \frac{e^{ikz}}{i\lambda z} e^{\frac{ik}{2z}[x^2+y^2]} \tag{2.23}$$

and its Fourier transform (the Fresnel transfer function) [6] is thus:

$$\mathcal{H}_F(f_X, f_Y) = e^{ikz} \cdot e^{i\pi\lambda z(f_X^2+f_Y^2)} \tag{2.24}$$

The e^{ikz} terms represents a constant phase delay to all plane-wave components traveling between the two planes, while the second term describes the additional phase delays induced to components traveling in different directions.

2.3 Digital holography and quantitative phase imaging

To properly image transparent or weakly scattering objects, the information about phase needs to be acquired. Unfortunately, all photodetectors (including human eyes) are only capable of capturing light intensity (proportional to square of wave amplitude) and not directly phase or electric field information. This challenge was first solved by Gabor, who had the idea of converting the phase information into intensity by interfering the (object) wave with a second known (so called *reference*) wave [9], giving birth to the field of *holography*.

Holography is, generally speaking, a technique that enables acquiring information of a light field phase and amplitude using the interference between object wave $U_{obj}(x,y)$ and reference wave $U_{ref}(x,y)$:

$$I_H(x,y) = |U_{ref}(x,y) + U_{obj}(x,y)|^2 \tag{2.25}$$

Although the exact notation varies for specific holography techniques (in-line, off-axis, Fourier holography) [10], the general Eq. 2.25 can be expanded using a simplified notation where * denotes complex conjugate, $\mathbf{O} = U_{obj}(x,y)$ and $\mathbf{R} = U_{ref}(x,y)$ as:

$$I_H = |\mathbf{R}|^2 + |\mathbf{O}|^2 + \mathbf{R}\mathbf{O}^* + \mathbf{O}\mathbf{R}^* \tag{2.26}$$

The terms $\mathbf{RO}^*$ and $\mathbf{OR}^*$ encode the complex amplitude of the object. In classical holography, the interferogram $I_H(x, y)$ is recorded in photosensitive media. When it was later illuminated by a so-called reconstruction beam (same as the reference beam), the hologram acts a diffraction grating. The reconstruction beam is thus diffracted after going through the hologram, producing two images (one from each term complex amplitude encoding term) of the object (real and *twin* image). However, the need for recording media such as photoresists, photopolymers or photographic plates proved limiting for the potential uses of the technology. At the same time, the interferograms in interferometry had to be analyzed using imprecise methods such as fringe width measurement or fringe counting. This was solved with the advent of digital imaging sensors, which gave birth to the field of *digital holography*.

Digital holography is a branch of imaging science, dealing with the numerical reconstruction of digitally recorded holograms and with generating and simulating of holograms and wave fields [11]. In digital holography, a digital camera is used to capture the holograms, replacing the photographic plate or polymeric films from classical holography. This eliminated the need for chemical development and enabled quick and advanced hologram analysis using the principles of Fourier optics, providing full information about recorded phase and intensity distributions.

Quantitative phase imaging (QPI) is a name given to a family of techniques capable of obtaining the optical phase modulations caused by the light passing through the sample [12]. This information can convey quantitative information about the object, such as its physical thickness or refractive index n. Digital holography is a very effective process for achieving high-precision quantitative phase microscopy. The phase image is directly available from the calculated 2D complex array of the holographic image [4]. The QPI techniques are mainly used to obtain marker-free, wide-field images of cells and tissues in biomedical imaging [13].

2.3.1 Twin-image artifacts in holography

Twin-image is a specific imaging artifact exhibiting itself as a virtual object localized behind the camera plane. It is an inherent feature of all digital holography setups [14] arising from the additional amplitude-encoding term $\mathbf{RO}^*$ in Eq. 2.26. Twin-images in digital holography appear because there are actually two objects (one real and one virtual, placed in conjugate plane) with the same light intensity distribution recorded in the hologram.

In the object plane, the twin-image typically appears as a mirror-symmetric out-of-focus object. Though the nature of the object is virtual, it's presence lowers the signal-to-noise ratio of the of the readout. There is a wide variety of techniques of both experimental [15, 16] and numerical nature [16, 17, 18, 19] on how to remove twin images in holography.

2.4 Image processing

Gray scale digital images, commonly represented in the spatial domain, consist of rectangular array of pixels (X,Y,p), combining location $(X, Y) \in \mathbb{Z}^2$ and the pixel value p, which can be a binary, float or complex value. Throughout this thesis, all the data is acquired and processed in the form of general, discrete 2D numerical arrays, mostly in the form of complex or float values. Complex representation is used for the representation of the light fields $U(X, Y) \in \mathbb{C}$. Since complex numbers encompass two degrees of freedom, two characteristics of the light fields can be directly accessed from the complex-valued fields:

i) the field light intensity information $I(X, Y)$, represented as a float-valued 2D array by computing the square of absolute value $|U(X, Y)|^2$ in each pixel position (X,Y);

ii) the field phase information $\varphi(X, Y)$, represented as a $[0, 2\pi)$ value 2D array by computing the angle

$$\varphi(X, Y) = \arctan\left(\frac{\mathfrak{I}(U(X, Y))}{\mathfrak{R}(U(X, Y))}\right) \tag{2.27}$$

in each pixel position (X,Y), where $X \in [0, M]$, $Y \in [0, N]$, $M \times N$ is the total number of image pixels in both dimensions, $\mathfrak{I}(\dots)$ represents the imaginary part of a complex number, $\mathfrak{R}(\dots)$ represents the real part of a complex number.

Both the intensity and phase-representing arrays can be handled in fashion very similar to gray scale digital images. They can be exported as black and white images after normalization to [0,1] range:

$$I_{IMG} = \frac{I(X, Y) - min\big(I(X, Y)\big)}{max\big(I(X, Y)\big) - min\big(I(X, Y)\big)} \tag{2.28}$$

Statistical analysis can be performed on the pixel values, such as the calculation of variance:

$$\sigma_I^2(I) = \left[\frac{1}{MN - 1}\sum_{X=0}^{M}\sum_{Y=0}^{N} I(X, Y)^2\right] - \mu_I^2 \tag{2.29}$$

where μ_I is the mean of all pixel values. When multiple images of the same scene are present, simple pixel-wise value averaging can improve the signal-to-noise ratio.

This can be realized using a formula:

$$I_{AVG}(X,Y) = \frac{1}{n}\sum_{N=1}^{n} I_n(X,Y) \tag{2.30}$$

This method is used extensively in the later chapters to combine multiple microscope images into one image with improved quality.

In specific situations, features may need to be highlighted and/or separated from the background. This can be done in a process called *image segmentation*. Edges constitute one of the image features that can be highlighted. This is commonly done by convolution with discrete differential operator. A typical example is the **Sobel filter**, which is an edge-enhancing image processing filter calculating the magnitude of picture gradient value at each (X,Y) pixel [20]. The Sobel filter has two integer-valued kernels, x-direction kernel (Fig. 2.1) and y-direction kernel.

-1	0	1
-2	0	2
-1	0	1

(a) The x-direction Sobel kernel.

-1	-2	-1
0	0	0
1	2	1

(b) The y-direction Sobel kernel.

Figure 2.1: Both of the Sobel kernels that are used for edge-enhancing in images.

The two convolutions return approximations of the partial derivatives along the rows and columns S_x and S_y. Then, the value of Sobel filtered image I at position (X,Y) approximately equals to the magnitude of the gradient of the image intensity ∇I:

$$|S_x(X,Y)| + |S_y(X,Y)| \approx |\nabla I(X,Y)| \tag{2.31}$$

2.5 Lensfree microscopy (LFM)

Lensfree microscopy (LFM) is a modern imaging technique enabling imaging of objects without the need for conventional lenses. Thanks to the simplistic nature of their core design, the LFM techniques gained significant interest of the scientific community mostly in recent decade. This can be explained by two factors: **(i)** decreasing prices of powerful imaging sensors like CMOS and CCD arrays (driven mainly by the smartphone camera market) and **(ii)** readily available and low-cost computational power. In case of lensfree imaging, the computations effectively replace the lenses, enabling the LFMs to be very compact and easily portable devices, but at the cost of always needing computer to process the data.

A conventional lensfree microscope in general consists of three main parts: **(i)** a suitable light source, usually coupled to a multimode fiber or spatially filtered by a pinhole, placed relatively far ($> 5\ cm$) from the sample to achieve (quasi)planar

wavefronts [21], **(ii)** a transmissive sample placed $< 1\ mm$ to the sensor and **(iii)** the imaging sensor in form of digital camera. Partial coherence of the light source is generally agreed to be optimal for lensfree imaging, since highly coherent sources lead to speckles, pronounced interference-based artifacts (such as multiple reflection interference). On the other hand, some degree of coherence is necessary to enable light interference. The usual solution is to use LEDs, which have low spatial and temporal coherence. The low temporal coherence is advantageous since it reduces the speckle, while the spatial coherence needs to be increased, usually be the means of spatial filters such as pinholes or adjustable irises. It was observed that spatial coherence is significant for the contrast and sharpness of the hologram [22]. Lower coherence also reduces the area where a cross-talk between signals from different objects is possible, which is desirable for dense packed samples (like cell colonies) [23].

The family of lensfree microscopy techniques includes many different methods. As suggested by [24], most of these microscopes can be characterized as **(i)** contact shadow-imaging based microscopes or **(ii)** holography-based lensfree microscopes. In the first group, samples are placed directly at the camera sensor to minimize the diffraction effects. Then, the recorded image is a direct transmission projection (shadow) of the sample. In the second group, samples are placed further from the sensor, thus diffraction effects can no longer be ignored. The image recorded on the camera then has a form of a Gabor (inline) hologram [25], formed by interference between light diffracted from the sample and non-diffracted background light. This is also the working principle of the lensfree interferometric microscope, the main device used in this thesis. This thesis is focused only on the holographic approach to lensfree microscopy.

The omission of lenses in the lensfree imaging system defines both the unique advantages and disadvantages of the technique. Unlike in conventional microscopes (which rely on focused light), LFM uses non-focused light. This leads to decoupling of field-of-view (FoV) from the maximal resolution. In most lensfree systems, the resolution is defined by the physical size of pixels of the imaging sensors and can be further increased by the means of pixel super-resolution [26, 27], or special sample-preparation methods [21]. Signal-to-noise ratio can also be improved by using refractive-index matching liquids [21]. Still, limited spatial resolution is one of the main downsides of lensfree microscopes. All holographic techniques require coherent light (to allow interference and hologram formation). However, optimal results in LFM are achieved by light sources that are only partially coherent (such as LEDs) [28], with highly coherent sources (lasers) leading to image degradation by excessive interference-based noise. This is a significant advantage, as LEDs are substantially cheaper, safer and smaller than laser systems. Lensfree systems are also usually robust and don't require precise aligning to function properly [26]. Because holograms are produced, post-measurement refocusing is possible by numerical backpropagation (see 2.2.1).

Since the resolving power of all lensfree imaging techniques is limited by the cam-

era pixel size d_{pix} (which is usually in the range of microns), there is significant interest in increasing the resolution. Since there are physical limits in manufacturing smaller image sensor pixels, alternative approaches need to be utilized. Using data processing, the *pixel super resolution* (PSR) approaches can digitally synthesize a high-resolution image with much smaller effective pixel size from a set of low-resolution, undersampled measurements with sub-pixel shifts with respect to each other [14].

To obtain multiple shifted frames, both mechanical and non-mechanical approaches can be utilized. Mechanical approaches utilize shifting of the specimen or imaging sensor [29, 30]. Non-mechanical approaches use e.g. LED arrays to achieve multiple angles of illumination [26], special light-shifting devices [31] or illumination wavelength scanning [14].

The PSR methods consist of two steps: **(i)** image registration (where the shifts between images are estimated) and **(ii)** image reconstruction, where the undersampled low-resolution frames are combined to produce a single, high resolution frame. The shifts between low resolution frames don't need to be known *a priori* and also don't have to be equal in both dimensions [26]. Image registration with subpixel accuracy can be realized in frequency domain, for instance by counting the fringe frequency in the cross-power spectrum [32] or through calculation of phase difference slope [33]. The reconstruction can be done both iteratively [34] and non-iteratively [35, 36]. In case sub-pixel shifting of images can not be realized, machine learning offers a very interesting alternative of increasing the image resolution [37, 38].

Uses of lensfree microscopes

Holographic lens-free microscopy is promising as a technique to enable colorimetric phenotyping of tissues [30], various types of cells [39] and small animals [28] in a compact form-factor and over large field-of-view. Using two separated light sources with different illumination angles, a lensfree microscope was utilized to track and characterize the three-dimensional movement of human sperm cells with submicron spatial accuracy [40]. Malaria parasites inside red blood cells were also successfully detected using LFM [26], same as invasive carcinoma cells within human breast sections [41], which were imaged with resolution sufficient for clinical evaluation by a pathologist. Thanks to the wide field-of-view, the lensfree systems are capable of monitoring cell functions such as cell-substrate adhesion, spreading, division and death for each cell in monitored cell culture [42].

3 Lensfree interferometric microscope (LIM)

This chapter focuses on the main device used throughout this thesis: *the lensfree interferometric microscope*. This device was proposed, designed and built by the team of Prof. Valerio Pruneri of the *Optoelectronics* group at ICFO Spain, with the main development done by Dr. Roland A. Terborg as one of the central aims of his doctoral thesis [43]. First, an overview of the design, advantages and limitations of the device is provided. Subsequently, the core principles of the main methods and algorithms used to obtain the quantitative phase and transmittance sample maps are laid out. At the end of the chapter, it is shown how certain optical components can be numerically modeled to simulate the LIM behaviour.

3.1 Overview of the method

Lensfree interferometric microscope (LIM) is a modern imaging device. It builds on the main design proposed by the lensfree microscope and extends its functionality to imaging of phase objects such as transparent and very weakly scattering structures (e.g. cells). This is possible thanks to the incorporation of linear polarizers and beam-splitting birefringent elements before and after the sample. These elements (called Savart plates) are the key components enabling the function of the LIM. Typically, a Savart plate consists of two stacked uni-axial crystals (calcite or quartz) of equal thickness, that split any incoming light into two parallel beams with perpendicular polarizations. Those beams are laterally sheared by distance s (Fig. 3.1). The stacked crystals are rotated 90° with respect to each other and their optical axes are oriented 45° to the normal of the surface. The shear distance s is linearly dependent on the crystal thickness d_{SP} of the crystals, as described by Eq. 3.1 from [44]:

$$s = \sqrt{2} d_{SP} \, |n_e^2 - n_o^2| (n_e^2 + n_o^2) \tag{3.1}$$

where n_o and n_e are refractive indexes of ordinary and extraordinary beams respectively.

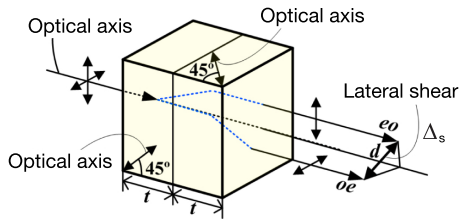

Figure 3.1: Schematic of beam-shearing properties of a Savart plate.

Thanks to the Savart plates, the LIM basically functions as a balanced shearing interferometer, similar to the principle of Mach-Zehnder interferometer (MZI, see Fig. 3.2). Instead of having two arms as in the MZI, the two laterally sheared beams in the LIM are created (and later joined) again in an in-line geometric configuration. The same approach was later also utilized in e.g. differential interference contrast microscopy by [45]

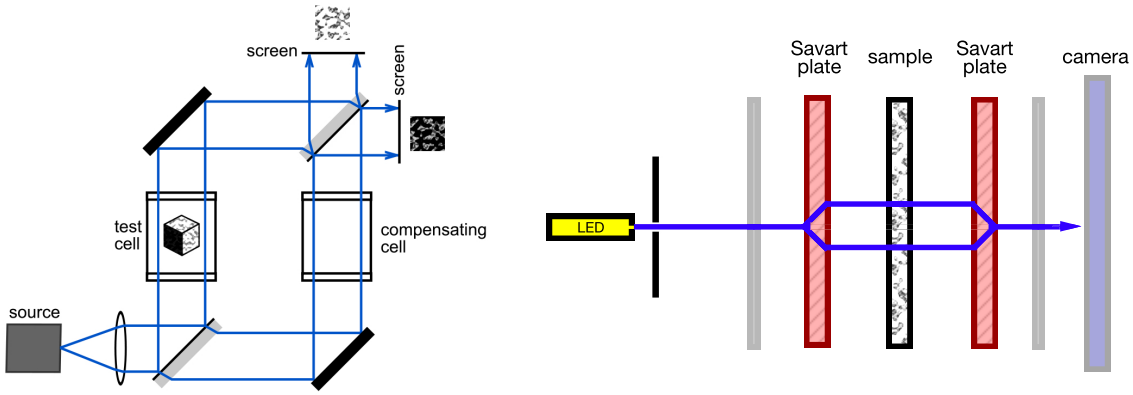

Figure 3.2: Comparison of the optical schemes for the Mach-Zehnder interferometer *(left)* and the lensfree interferomeric microscope (LIM) *(right)*.

3.1.1 Optical setup of the LIM

As mentioned before, the LIM setup builds on the foundation of the LFM (see Fig. 3.3). In a naming convention similar to what is generally used in LFM [46], Z_1 is distance between the light source and the sample plane, while Z_2 is the distance between the sample plane and the image sensor of digital camera.

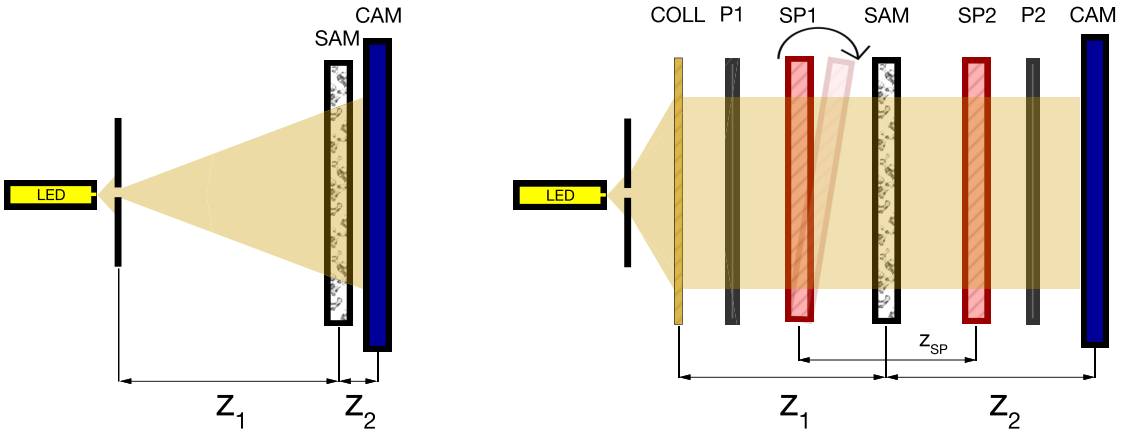

Figure 3.3: Scheme of a typical LFM optical setup *(left)* and the LIM setup *(right)*.

First, a collimated illumination (**LED,COLL**) is polarized with a linear polarizer **P1** oriented at 45°. The light enters the first Savart plate **SP1** and is split into two ⊥-polarized beams sheared by distance s. Thanks to the 45° orientation of **P1**, the two sheared components have equal intensity. These two beams then interact with the sample **SAM**, which can introduce a relative phase difference between the two components. The second Savart plate **SP2** then joins the beams back together. Since the phase difference was introduced between perpendicular polarizations, a second polarizer **P2** is needed for recombination of the two polarizations. This leads to light interference contrast (constructive or destructive, depending on the phase difference) that is recorded by a digital camera **CAM**. The **P2** polarizer can either be in crossed orientation with the first one (which results in "dark field" holograms) or parallel to the first one ("bright field" holograms). Both of these configurations are suitable for the measurements. The space between the two Savart plates (denoted as Z_{SP}) represents the sample chamber (and maximal volume of measured specimen).

3.1.2 Holographic contrast formation

This technique belongs to the family of *quantitative phase-contrast imaging* techniques (QPI). In those techniques, a 2D map of phase differences is reconstructed for the specimen for each point within the field of view [2]. By definition, a relative phase shift of a wave by an object is proportional to the object thickness h and its refractive index (RI) n (or more specifically, difference of RI in relation to the surrounding medium Δn). These two variables are coupled in the resulting phase map. As is shown on Fig. 3.4, the interferometric contrast appears when one of the sheared beams is shifted in phase. Since the second Savart plate **SP2** is located after the specimen, the LIM phase maps exhibit typical doubled images, separated by the shearing distance. These two phase images have same magnitude, but opposite sign. Objects smaller than the shearing distance s appear twice, while for objects larger than shearing distance, only some edges are shown.

It is not uncommon for phase-shifting interferometry techniques to detect phase differences in the range of $\lambda/1000$ [48]. LIM has similar phase sensitivity in the region of ångstroms [47]. Thanks to the differential character of images being governed by the shearing distance, LIM is especially well suited for imaging objects smaller or comparable to the shearing distance s, which was utilized to measure height changes in arrays of microdots [47], biosensing using plasmonics [49] and refractive index changes due to thermo-optic effects [43].

3.1.3 Advantages and disadvantages

The LIM preserves many of the characteristics of the LFM and adds some additional improvements. Notably, some of the advantages include:

i) the ability to show phase contrast and transmittance maps;

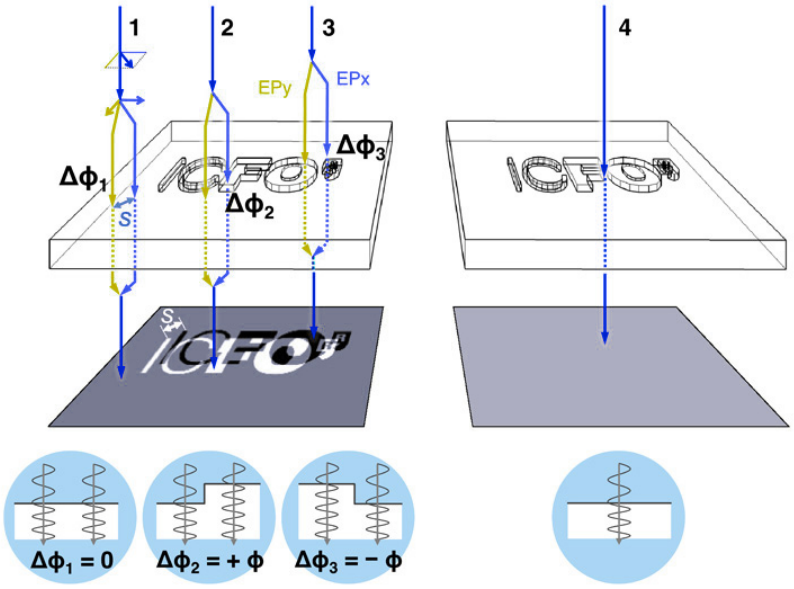

Figure 3.4: Contrast formation scheme from transparent objects for the LIM *(left)* and for non-interferometric method such as optical microscopy *(right)*. Reproduced from [47].

ii) the capability of acquiring images of the whole field-of-view at once, without the need to scan through the sample (like in confocal microscopy);

iii) decoupling of the field-of-view from spatial resolution. The field-of-view is defined by the sensor area, while the spatial resolution is defined (among other factors) by the pixel-size d_{pix}, which are two independent parameters. Simply replacing the sensor with one having bigger surface area will increase the examined field-of-view;

iv) compact dimensions and lower weight thanks to not relying on glass lenses;

v) general flexibility of the optical setup, enabling easy resizing of specimen chamber to fit the needs of the end user;

vi) capability to digitally refocus into different plane *after* acquiring the datasets;

vii) in comparison to conventional phase-shifting approaches [50], there's no need for high precision in the introduced phase differences;

viii) easy alignment due to the use of non-coherent light sources.

Some of the disadvantages include:

i) limited spatial resolution. This is the inherent trade-off stemming from the use of non-focused light. Spatial resolution can be increased by using cameras with smaller pixel pitch and by post-processing methods;

ii) reliance on computer to acquire and show the results (requires data post-processing);

iii) limited illumination angle range due to the need to preserve the condition of balance for the common path interferometer;

iv) unlike the LFM [51], the LIM method is not suitable for imaging real-time processes due to the need to perform Savart plate tilting, multiple frames acquisition and computationally intensive post-processing (including the phase-shifting algorithm) for every measurement.

3.2 Terborg's Phase-shifting interferometry (PSI)

This method is based on the conventional *Phase-shifting digital holography* (PSDH) method, which utilizes multiple holograms with precisely specified phase difference between the reference and object wave to allow point-by-point phase reconstruction [4]. A set of at least three measurements is necessary, with more measurements providing better performance [52]. However, there are situations where precise readjustments of phase difference between reference and object wavefront are not possible. The above-mentioned approach is also not optimal for measurements with multiple illumination wavelengths, as every wavelength will require its own set of measurements.

In the paper of Terborg et al. [47], a different phase-shifting interferometry (PSI) approach is proposed which utilizes a large set of interferograms with varying phase-shifts introduced by gradually tilting one of the Savart plates in the setup.

To introduce the mechanism of this method, let's assume a linearly polarized (45°) beam entering the Savart plate. At the output, two parallel beams with same amplitude and perpendicular polarization will be present. For simplicity, assume one-dimensional waves propagating along x. Those can be characterized by complex-valued phasor representations $U_1(x,t) = E_0 e^{i\varphi_1}$ and $U_2(x,t) = E_0 e^{i\varphi_2}$, where $\varphi = kx - \omega t + \Phi$ is the *phase* of the wave. The actual real-valued physical electric field E is equal to the real part of the complex amplitude: $E(x,t) = \Re(U(x,t))$

Due to the differential nature of the technique, it can be assumed that one of the beams interacts with a sample, while the second sheared beam passes through a free region. This can be regarded as an analogy of sample and reference beams in Mach-Zehnder interferometer. After interaction, these two beams are sheared back into the original position by a reversely oriented Savart plate and passed through polarizer to cause interference between the perpendicularly polarized elements. This interference is a result of superposition between those two beams which can be expressed as:

$$U(x,t) = U_1(x,t) + U_2(x,t) = E_0(e^{i\varphi_1} + e^{i\varphi_2}) \tag{3.2}$$

The light intensity I is proportional to the square of the light electric field:

$$I(x) = \frac{1}{Z_0}\int^t U(x,t)\cdot U^*(x,t)\mathrm{d}t \propto E_0^2 \cdot (e^{i\varphi_1} + e^{i\varphi_2})(e^{-i\varphi_1} + e^{-i\varphi_2}) \tag{3.3}$$

where $Z_0 \approx 377\Omega$ is the impedance of free space [53]. Factoring out this constant to simplify the formulas (while keeping this change in mind), Eq. 3.3 can be rewritten as:

$$I(x) = E_0^2 \cdot (1 + e^{i(\varphi_1 - \varphi_2)} + e^{-i(\varphi_1 - \varphi_2)} + 1) \tag{3.4}$$

Using the trigonometric identity

$$\cos(x) = \frac{e^{ix} + e^{-ix}}{2} \tag{3.5}$$

the Eq. 3.4 can be directly expressed as:

$$I(x) = E_0^2(2 + 2\cos(\varphi_1 - \varphi_2)) = 2E_0^2(1 + \cos(\varphi_1 - \varphi_2)) \tag{3.6}$$

Since φ_1 and φ_2 are the phases of both waves, and both waves were initially in phase, we can express those with a set of two new arguments

$$\varphi_1 + \varphi_2 = \Delta\varphi + \psi \tag{3.7}$$

where $\Delta\varphi$ is the phase difference of the two waves introduced by the sample and ψ is the phase difference between the two waves introduced by tilting of the Savart plate. It was confirmed by Terborg et al. [47] that small tilts of the Savart plate translate linearly into change of phase between the two beams, while not causing any unwanted side-effects like measurable change of shearing distance.

Combining Eq. 3.7 into 3.6 results in new formula:

$$I(x) = 2E_0^2(1 + \cos(\Delta\varphi + \psi)) \tag{3.8}$$

which can be rewritten using trigonometric identity $\cos(\alpha + \beta) = \cos(\alpha)\cos(\beta) - \sin(\alpha)\sin(\beta)$ as:

$$I(x) = 2E_0^2 + 2E_0^2(\cos(\Delta\varphi)\cos(\psi) - \sin(\Delta\varphi)\sin(\psi)) \tag{3.9}$$

The aim is to reconstruct the phase information $\Delta\varphi$, which means separating the cross-terms in Eq. 3.9. This can be done by integrating $I(\psi)$ with either sine or cosine of ψ.

Lets define two new functions $\Psi_{\sin}$ and $\Psi_{\cos}$ (in a specific point x) as:

$$\Psi_{\sin} = \frac{1}{\pi}\int_0^{2\pi} I(\psi)\sin(\psi)\mathrm{d}\psi \tag{3.10}$$

$$\Psi_{\cos} = \frac{1}{\pi}\int_0^{2\pi} I(\psi)\cos(\psi)\mathrm{d}\psi \tag{3.11}$$

Combining Eq. 3.10 and Eq. 3.9 leads to:

$$\begin{aligned}\Psi_{\sin} = \frac{2E_0^2}{\pi}\Big(\int_0^{2\pi}\sin(\psi)\mathrm{d}\psi + \cos(\Delta\varphi)\int_0^{2\pi}\sin(\psi)\cos(\psi)\mathrm{d}\psi \\ -\sin(\Delta\varphi)\int_0^{2\pi}\sin(\psi)^2\mathrm{d}\psi\Big) = -2E_0^2\sin(\Delta\varphi)\end{aligned} \tag{3.12}$$

Similarly, for $\Psi_{\cos}$ we obtain:

$$\Psi_{\cos} = 2E_0^2\cos(\Delta\varphi) \tag{3.13}$$

Finally, since we have two variables and two equations, we can obtain the phase difference $\Delta\varphi$ from:

$$\Delta\varphi = -\arctan\left(\frac{\Psi_{\sin}}{\Psi_{\cos}}\right) = -\arctan\left(\frac{-2E_0^2\sin(\Delta\varphi)}{2E_0^2\cos(\Delta\varphi)}\right) \tag{3.14}$$

The intensity distribution I_{sam} can be obtained from:

$$\sqrt{\Psi_{\sin}^2 + \Psi_{\cos}^2} = \sqrt{4E_0^4(\sin^2(\Delta\varphi) + \cos^2(\Delta\varphi))} = 2E_0^2 = 2I_{sam} \tag{3.15}$$

Since this method is differential, we need reference measurement (without a sample) to assess the transmittance of the specimen. Knowing the intensity map of reference I_{ref}, we can finally express the *transmittance* T as:

$$T = \frac{I_{sam}}{I_{ref}} \tag{3.16}$$

It's also important to keep in mind that since all of the integration operations above are (in our case) done numerically, it's crucial to ensure that the ψ argument of $\sin(\psi)$ and $\cos(\psi)$ is extrapolated with high precision. Doing otherwise results in improper cancellation of cross-terms in the PSI integrals, leading to imprecise readouts in the measurements.

3.3 Holographic focusing *via* field backpropagation

This Fresnel diffraction algorithm (introduced in Sec. 2.2.1) is used in the LIM to digitally reverse the effect of light diffraction and obtain a sharp, focused image of inspected objects. It consists of multiple steps.

First, the optical wavefront, represented by discrete complex-valued 2D electric field $U(X, Y)$, is padded with zero valued pixels. There are two reasons why padding of the field is applied. When an electric field of a finite size is back-propagated using the frequency domain based approach, the diffraction effects "reflect" from the field edges and cause additional noise in the final results [54]. Second reason is due to the nature of 2D FFT algorithms, which provide increased performance for fields with dimensions equal to a power of two (2^n). Hence, padding the field to the nearest (or second nearest[1]) higher power of two improves the performance and suppresses artifacts.

The padded field $U_p(X, Y)$ is then transformed into frequency domain by the means of discrete 2D Fast Fourier Transform (FFT) algorithm.

$$\mathcal{U}(f_X, f_Y) = \mathcal{F}\{U_p(x, y)\} \tag{3.17}$$

In the frequency domain, $\mathcal{U}(f_x, f_y)$ is then shifted by the means of standard function *fftshift* to center the frequency spectrum around the DC element. Then, the field is multiplied by the Fresnel transfer function $\mathcal{H}_F(f_X, f_Y)$ in the form of:

$$\mathcal{H}_F(f_X, f_Y) = e^{i\pi\lambda z_p(f_X^2 + f_Y^2)} \tag{3.18}$$

where z_p is the distance the field should be propagated. The frequency-domain representation of the field in plane z_p, represented as $\mathcal{U}_{z_p}(f_X, f_Y)$, is then equal to:

$$\mathcal{U}_{z_p}(f_X, f_Y) = \mathcal{U}(f_X, f_Y) \cdot \mathcal{H}_F(f_X, f_Y) \tag{3.19}$$

Following that, the field is unshifted by the means of standard *ifftshift* and transformed back into the spatial domain by inverse 2D discrete Fast Fourier Transform (iFFT) algorithm to obtain the amplitude and phase of the resulting optical wave, corresponding to a certain distance from the sensor.

$$U_{z_p}(X, Y) = \mathcal{F}^{-1}\{\mathcal{U}_{z_p}(f_X, f_Y)\} \tag{3.20}$$

In the final step, the array padding added in the first step is removed and the result is returned as the backpropagated field.

[1] This improves the reflection elimination for fields with dimensions very close to the nearest power of two, such as 1023×1023.

3.4 Twin image suppression

In classical in-line holography, the real and virtual images are in the same position [16]. This is not the case of LIM setup where, even though the geometry is also in-line, the real and twin-images are shifted by the used Savart plates (see Fig. 3.5). The twin image has negative magnitude compared to the original and is located at the same propagation distance, only with opposite sign (the so called *conjugate plane*).

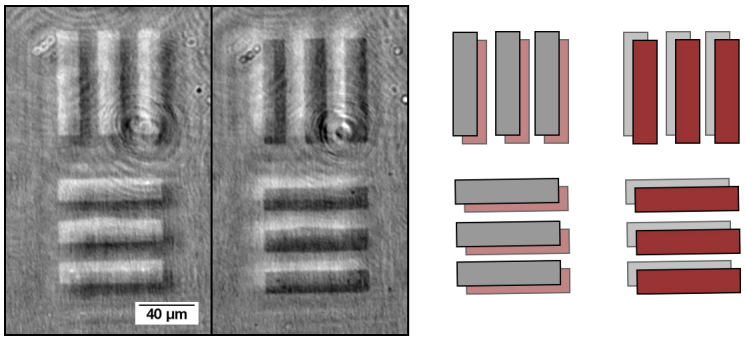

Figure 3.5: Twin images in the OPD maps measured by LIM *(left)*. Propagating to the conjugate plane, the twin clearly comes out from the background while the original image becomes defocused. The scheme on the right illustrates the situation.

One of the solutions to this problem could be the use of a deconvolution algorithm since it can be assumed that the readout of the LIM has a character of two opposite-valued δ-functions separated by shear s. However, due to significant noise of the images, deconvolution performs very poorly. A more intuitive approach defined by Terborg [43] utilizes the knowledge of real-image focus distance z_f and shearing direction. By refocusing the image into the conjugate plane $-z_f$, the twin image gets in focus and the original image becomes a twin image in the original position (Fig. 3.5, *left*). By changing the sign of the now-focused twin image, shifting it spatially to the position of the original and averaging both images, we bring out the desired features while reducing the intensity of the twin images by half, at the cost of gaining the reduced twin also in the other direction of the shear. This results in improved signal-to-noise ratio (see Fig. 3.6).

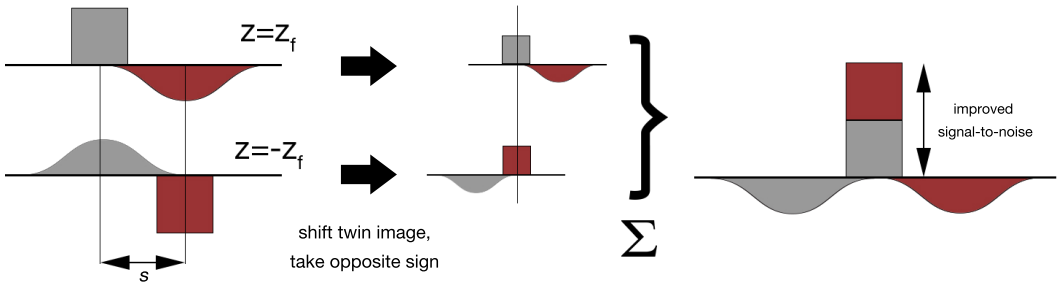

Figure 3.6: Scheme of the twin image suppression process.

3.5 Numerical models of optical elements

Using the *numpy* package in Python3, all of the elements in the LIM setup were modeled to allow simulations and testing of the microscope behavior. The simulations in this chapter are mostly based on the models developed of Dr. Roland Terborg. Each of the following subchapters describes one element of the optical setup.

3.5.1 Collimated light source

The collimated source is the primary light source of the LIM. The light source was modeled using a non-polarized beam with modified Gaussian profile. The E_x and E_y polarization components of the electric field $\vec{E}$ for each point in space were calculated using:

$$E_x = E_y = e^{-(X^2+Y^2)/r^2} \tag{3.21}$$

where X, Y represents position in pixel array and r represents the beam radius.

3.5.2 Linear polarizer

The wavefront in the LIM then travels through the first polarizer. For arbitrarily rotated polarizer rotated by angle θ, the input light polarizations have to be first projected to the axis of the polarizer and then projected back from this axis to the original coordinate system.

The field p_{pol} after the polarizer has a form of:

$$p_{pol} = E_{x0}\cos(\theta) + E_{y0}\sin(\theta_p) \tag{3.22}$$

The output electric field $\vec{E} = (E_x, E_y)$ can then be represented as:

$$E_x = p_{pol}\cos(\theta) \tag{3.23}$$

$$E_y = p_{pol}\sin(\theta) \tag{3.24}$$

3.5.3 Savart plate

Next element is the **Savart plate**. The Savart plate is a type of birefringent polarizer that splits an incoming beam into two laterally shifted beams of perpendicular polarization, with shear distance s and shear angle θ.

First, the input polarizations have to be first projected on the on the x and y axes of the Savart plate. For a Savart plate orientation θ defined as 0°, the two axes p_{Sx} and p_{Sy} are oriented at 245° and 315°, respectively. Projections to the axes of the Savart plates are then:

$$p_{Sx} = E_x \cos(\theta_{Sx}) + E_y \sin(\theta_{Sx}) \tag{3.25}$$

$$p_{Sy} = E_x \cos(\theta_{Sy}) + E_y \ sin(\theta_{Sy}) \tag{3.26}$$

Following that, two projection are then laterally shifted. The shear distance in both axes is the same and equal to:

$$s_x = s_y = \frac{s}{\sqrt{2}} \tag{3.27}$$

Projections p_{Sx} and p_{Sy} are shifted with distances s_x and s_y in directions defined by angles θ_{Sx} and θ_{Sy}. Optionally, a phase shift in one of the polarizations can be introduced by multiplying with complex exponential:

$$p_{Sy} = p_{Sy} \cdot e^{i\psi} \tag{3.28}$$

where ψ is the introduced phase shift. After the shifting, the electric fields are reconstructed by projecting from p_{Sx}, p_{Sy} back to the real coordinate system:

$$E_x = p_{Sx} \cos(\theta_{Sx}) + p_{Sy} \sin(\theta_{Sy}) \tag{3.29}$$

$$E_y = p_{Sx} \sin(\theta_{Sx}) + p_{Sy} \cos(\theta_{Sy}) \tag{3.30}$$

3.5.4 Phase and intensity objects

The measured sample can influence light using the combination of two effects: by changing intensity (by absorption/scattering) or by shifting the phase. While intensity objects can be viewed with conventional light microscopes or naked eye, phase imaging requires special methods usually relying on light interference (like holography).

Considering a 2D pixel array representing the polarized wavefront, an intensity object can be simply modeled by multiplying the complex amplitude U (with amplitude E_0 and phase φ) by transmittance coefficient T of the intensity object.

$$U_{att} = U \cdot T = E_0 e^{(i\varphi)} \cdot T \tag{3.31}$$

On the other hand, a phase shift ψ can be introduced by multiplying the complex amplitude by appropriate complex exponential:

$$U_{ph} = U \cdot e^{i\psi} = E_0 e^{[i(\varphi+\psi)]} \tag{3.32}$$

To introduce a specific increase d in optical path difference (OPD), similar formula can be used:

$$U_{ph} = U e^{\frac{2i\pi d}{\lambda}} = E_0 e^{i(\varphi+\frac{2\pi d}{\lambda})} \tag{3.33}$$

To preserve notation from previous sections, same approach can be applied on both numerical 2D arrays E_x, E_y representing perpendicular polarization elements of the light source by replacing the complex amplitude U in previous equations with E_x and E_y.

4 Single-plane LIM imaging

In first part of this chapter, the focus is on building the prototype of LIM device and optimizing various parameters of the setup. Based on the findings, the optimal setup geometry is proposed and the main prototype is built. This optimized LIM prototype is the device that is used for all the subsequent measurements in this thesis. Following that, the prototype's performance was verified on a resolution target. In the second part of the chapter, different approaches are introduced and evaluated regarding the image focusing and imaging quality improving, both with the use of data post-processing.

4.1 Measured samples

The main sample used for testing and measuring in this chapter was a custom USAF1951 resolution test target made in-house by the members of my group using photolithography. The target differs from conventional resolution targets with intensity objects, since it consists of quartz glass plate with transparent silica structures (acting as phase objects). Resolution targets with uniform feature height of $h = 5\ nm$ and $10\ nm$ were prepared. The feature sizes can be seen on Fig. 4.1.

4.2 Measurement procedure

Every LIM measurement consists of two main steps: **(i)** reference acquisition and **(ii)** sample acquisition. During each of these steps, a dataset of $n_c = 30$ frames is captured for each color while gradually tilting the first Savart plate, **SP1** (resulting in 90 captures in total when using red, green and blue illumination). The tilt introduces a phase shift between the two polarization components of light [47]. When those polarizations are later recombined by **SP2** and **P2**, they create an interferogram on the camera. Because of that, a sine-shaped pixel intensity modulation is observed on the camera while tilting the **SP1**. The movement range is adjusted so that a full interference fringe for all the colors was captured while tilting the Savart plate (see Fig. 4.2). After finishing the acquisition, the pixel intensity optical transfer function (OTF) curves are calculated and fitted with cosine to acquire the necessary frequency ψ for Eq. 3.10. Using this parameter, the PSI method is performed (Chap. 3.2). This method returns a complex light electric field in the camera plane $z_p = 0$. These calculated electric fields (sample and reference) are then subtracted to obtain the differential information about the 2D phase changes in the specimen. To acquire information from the sample plane $z_f = Z_2$, numerical back-propagation algorithm is used on the electric field (see Chap. 2.2.1). After back-propagating, the desired optical path difference and transmittance maps are returned in the graphical user interface (GUI) for each illumination color. In the

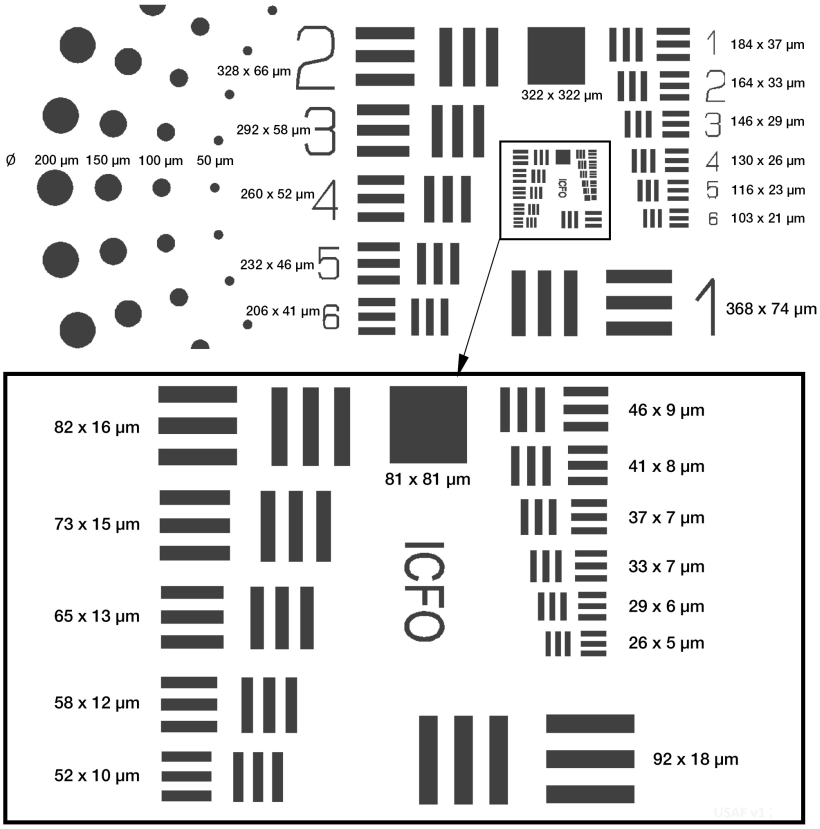

Figure 4.1: Dimensions of structures on the custom USAF resolution target made by lithography.

final step, the different illumination maps can be averaged to improve signal-to-noise ratio and suppress diffraction fringes of dust and out-of-focus objects. This is the original procedure used to obtain images in the LIM.

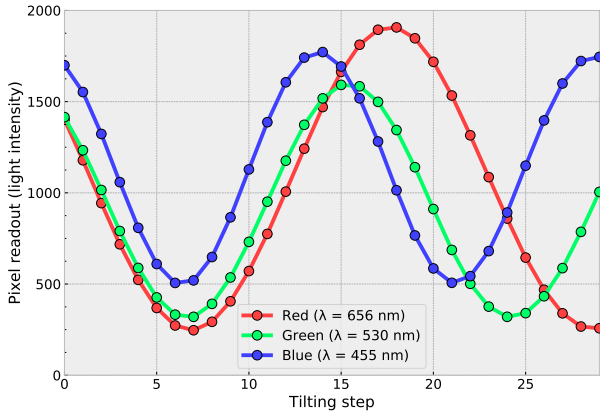

Figure 4.2: Optical transfer functions (OTFs) of all the used colors. The tilting range and step were adjusted to capture a full (minima to minima) range of interference.

4.3 Building and optimizing the LIM setup

The optical setup of the LIM was built according to the scheme provided by Terborg et al. [47] that can seen on Fig. 4.3.

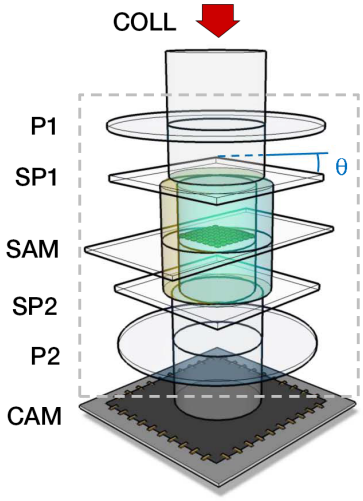

Figure 4.3: The components of the optical setup of the LIM. *Reproduced from* [47].

Light from a multi-wavelength ($\lambda = 455\ nm, 530\ nm, 656\ nm$) LED source (*Mightex Systems*) was directed using an optical fiber to a fiber-coupled reflective collimator (RC08SMA-P01, *Thorlabs*). A subsequent aperture was adjusted to remove unwanted internal reflections. The collimated output beam was polarized by a linear polarizer **P1** (*Thorlabs*) and passed through first calcite Savart plate **SP1** (10×10 mm AR-coated, *United Crystals*). Calcite was selected due to larger beam displacement per thickness, enabling the usage of thinner plates compared to quartz. The Savart plate (**SP1**) was mounted in custom CNC-made aluminum holder in a kinematic mount (KC2/M, *Thorlabs*) to enable tilting. The movements were provided by a DC actuator (Z812, *Thorlabs*) via the computer-connected controller (Kinesis KDC101, *Thorlabs*). Below the mount, a sample was placed in a simple aluminum holder. The light then passes through a second Savart plate **SP2** with the same properties placed inversely in comparison to the first one. The two beams sheared by **SP1** have perpendicular polarization. To obtain contrast, they were combined together by a second polarizer **P2** (placed in crossed orientation in relation to the first one **SP2**) and sampled using a visible light imaging sensor array (digital camera, UI-3882LE-M, *IDS*). The optical setup was designed using a cage system (30 *mm and* 60 *mm, Thorlabs*) to allow easier Savart plate alignment (which has to be done by eye) while preserving the advantage of compact size.

The acquisition of images, control of the LEDs and movements of motors were all automated using Python 3.6 on a Linux-running single board computer (UPboard2, *AAEON*). This makes the system fully self-sustained, not requiring external computer to control the device or process the data. All the electronic components, the

computer, controller and power supply were mounted together in a single aluminum enclosure (EC1C, *Thorlabs*, see Fig. 4.4).

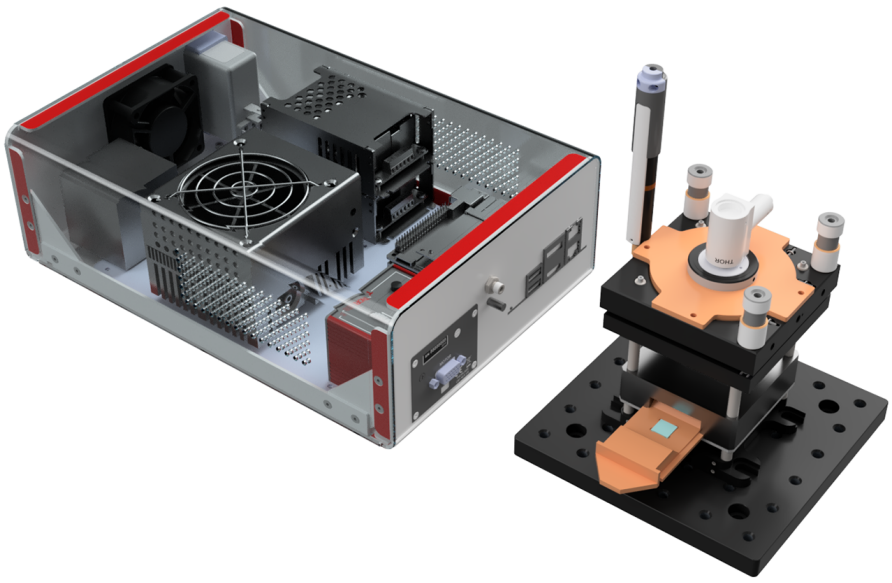

Figure 4.4: Digital render of the setup (with enclosure) and box with electronics.

It is worth mentioning that the precision of the actuator moving the Savart plate has significant effect on the final image quality. It was observed that poor movement precision results in distorted sine curve of the OTF, which in turn results in sub-optimal cross-term cancellation in the PSI (see Chap. 3.2), leading to noisy images with artifacts. Other setup parameters (such as distances between elements) also influence the final readout quality. In the following sections, various parameters of the setup were measured and evaluated to find the optimal geometry and best performing components.

4.3.1 Optical fiber selection

Conventionally, the LIM operates with a single multi-mode fiber coupled to a partially coherent LED source. This raises the question of optimal fiber parameters to ensure the most efficient readouts, especially in terms of final resolving capability and measured light intensity.

First, a series of optical fibers (described in Table 4.1) was tested with a reflective collimator (RC12SMA-P01 (beam diameter 12 mm), *Thorlabs*).

As can be seen on Fig. 4.5, a measurement of the USAF resolution target was taken for each fiber core while preserving all the other parameters of setup.

Illumination with the smallest core fiber (25 μm) resulted in increased occurrence of coherence-related artifacts (like background interference fringes) for each color

fiber product name	core diameter	NA	length
Thorlabs **M68L01**	25 μm	0.10	1 m
Thorlabs **M14L01**	50 μm	0.22	1 m
Thorlabs **M15L01**	105 μm	0.22	1 m
Thorlabs **M25L01**	200 μm	0.22	1 m

Table 4.1: Parameters of tested multi-mode optical fibers.

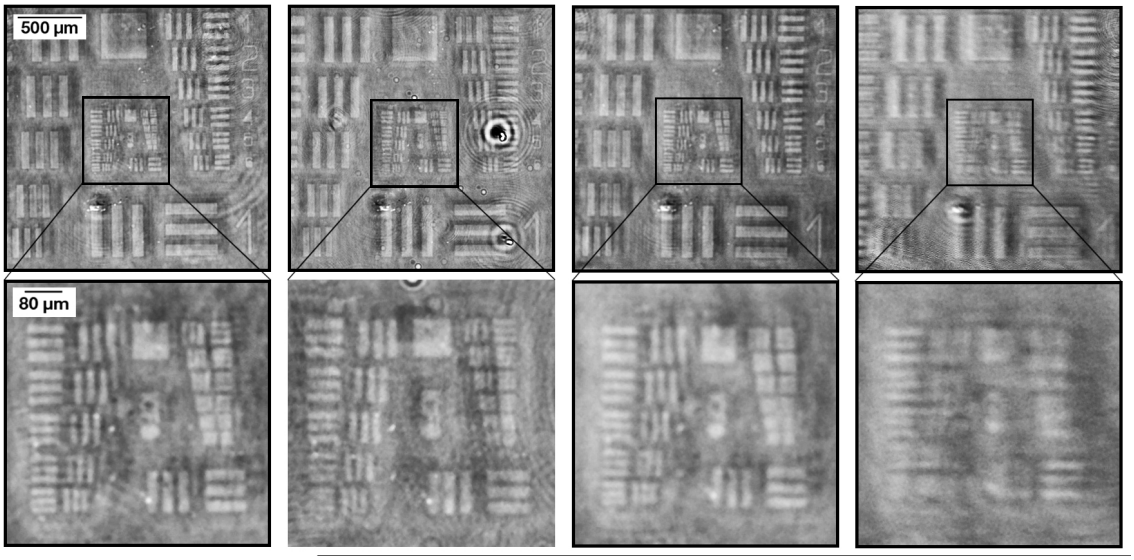

Figure 4.5: Multispectral (R+G+B average) OPD maps of USAF resolution test taken with different fibers. Left to right: 25 μm, 50 μm, 105 μm, 200 μm cores, each with detailed zoom on small features. Large fiber core lead to noticeable smearing of images.

channel. The fiber core output actually acts as a spatial filter, modifying the coherence of light (see Chap. 2.5), with smaller pinhole providing higher coherence. This is in agreement with the measurements (finer details are visible). In addition, the overall intensity output of the small diameter fiber was significantly lower (not enough light intensity passes through the small core) and thus very high exposure times had to be used with modification to pixel-clocking frequencies of the camera. This resulted in lower maximal frames-per-second readouts, occasional occurrence of image readout errors and general slowing down the measurements. On the other hand, the largest fiber core exhibited significant smearing of the image and diminished resolution. These effects are in agreement with expected decrease in spatial coherence due to "wider pinhole" at the fiber end.

For the reasons stated above, the 50 μm optical fiber core was deemed as optimal for the LIM due to sufficiently high amount of reproduced details while providing reduced coherence-related artifacts and sufficient intensity of the output light compared to the 25 μm core.

4.3.2 Multicore fiber bundle

To further advance the possibilities of the LIM setup towards higher-resolution and depth enabled imaging, an optical fiber bundle was used with the aim of providing multiple illumination angles while preserving the collimated character of light. Following the previous results, a custom-made 1-to-7 optical bundle with 50 μm core (*Thorlabs*) was used in conjunction with a reflective collimator.

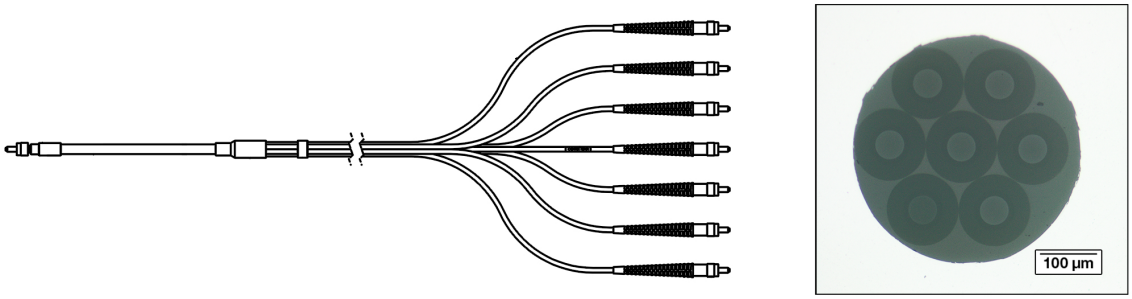

Figure 4.6: Drawing of the fiber bundle *(left)* and microscope image of the fiber bundle connector *(right)*.

As shown in the image taken with an optical microscope (Fig. 4.6), the fiber cores are evenly separated from the central core by a distance of $100\mu m$. Since the reflective collimator effectively behaves as a lens with source in the focal plane, it was assumed that a small displacement of the fiber core output (=point source) in the focal plane of the collimator will result in collimated beam with new propagation direction $\vec{k}_n$ (Fig. 4.7). It was also assumed that the angle θ between $\vec{k}_0$ and $\vec{k}_n$ will be constant for all the six cores thanks to the equal spacing between cores.

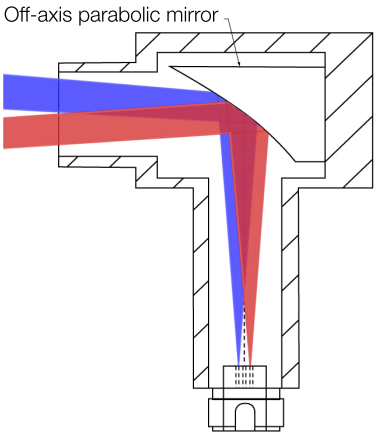

Figure 4.7: Scheme of a reflective collimator in conjunction with multicore fiber bundle. Varying the position of light source in the focal plane of the collimator results in different direction of the collimated beam.

This assumption was verified in a simple setup consisting of reflective collimator, followed by 100 μm pinhole and a digital camera, without Savart plates. Using

different cores, the image of the pinhole (modulated by the point-spread function) moved on the field-of-view with the shifts vectors forming a perfect hexagon (Fig. 4.8). This experiment verified the constant angle assumption.

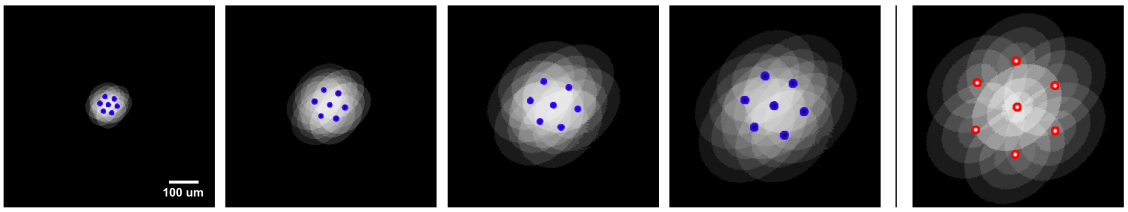

Figure 4.8: Overlay of multiple LFM captures of a pinhole, illuminated with angled illuminatin beams. The images were processed with posterizing filter to enable better spot center localization. The spot centers are shown with colored dots. As the pinhole was gradually moved away from the camera, the projections moved further from the center in a linear fashion. Rotation of the collimator resulted in different orientation of the hexagon, while preserving the equal distance between projections *(right)*.

Second assumption was that the use of collimator with smaller *reflected focal length* (RFL) will result in higher "tilt" angle for the same displacement of source in the focal plane, with the image shift ratio between two used collimators being equal to the ratio of the RFL values. This was experimentally verified using two reflective collimators (RC08APC-P01 and RC12SMA-P01, *Thorlabs*). The RFL ratio for this pair is:

$$r = \frac{RFL_{08}}{RFL_{12}} = \frac{33\ mm}{50.8\ mm} = 0.649 \tag{4.1}$$

which is in very good agreement with experimentally measured value (0.657) for a pinhole in simple LFM setup. The small discrepancy between the numbers is most likely caused by the non-precise estimation of center of the diffracted image of the pinhole, which would result in different measured distance between the beam centers. The beam angle from the optical axis of the setup can be easily calculated using the principles of geometrical optics. The ratio between collimator focal length F_{coll} and core displacement d_c must be equal to the ratio between object projection displacement $|\delta|$ and object height z:

$$\frac{d_c}{F_{coll}} = \frac{|\delta|}{z} \tag{4.2}$$

This is result of triangle congruency. From this, the relation between object projection displacement and object height can be easily expressed as:

$$z = \frac{F_{coll}}{d_c} \cdot |\delta| = \kappa \cdot |\delta| \tag{4.3}$$

where $\kappa = \frac{F_{coll}}{d_c} \approxeq \frac{33000\ \mu m}{150\ \mu m} \approxeq 220$ is the proportionality constant. It's important to use displacement in metric units (not pixels) to also obtain propagation distance in metric units. By calculating the ratio of in-focus planes to displacements from experiments, the value was confirmed to be $\kappa \approxeq 230$, about 4.5% different from the theoretical value and thus in very good agreement. Finally, the angle between the setup optical axis and angled beam direction θ is simply equal to:

$$\theta = \arctan\left(\frac{d_c}{F_{coll}}\right) \approxeq 0.260^\circ \tag{4.4}$$

4.3.3 Digital camera selection

As mentioned in Sec. 2.5, digital camera is required to acquire and further process the interferograms. In an ideal case, the LIM requires a raw output from the imaging sensor without any further post-processing. Ideally, the sensor should have a small pixel size (to attain higher spatial resolution) and high sensitivity (for improved s/n ratio), while real-time performance capabilites (such as maximum FPS rate) are not of high importance in this project. To obtain high dynamic range, the camera should operate with high bit depth. Since the active area of the imaging sensor governs the field-of-view, it should be evaluated what sensor size is optimal for the operation of the device. Very large sensors are expensive and produce significantly larger datasets, which may in turn noticeably increase the post-processing times and hardware requirements. Simultaneously, for large field-of-view, the pixel size often increases.

In the LIM setup, two different cameras were tested, each in both monochromatic and RGB-enabled version (Table 4.2).

Producer	Model	Sensor area	Resolution	Pixel size	Color mode
Basler AG	daA2500-14uc	24.4 mm^2	2592×1944	2.20 μm	RGB
	daA2500-14um	24.4 mm^2	2592×1944	2.20 μm	B/W
IDS GmbH	UI-3882LE-C	36.9 mm^2	3088×2076	2.40 μm	RGB
	UI-3882LE-M	36.9 mm^2	3088×2076	2.40 μm	B/W
	UI-3202SE-M	146.81 mm^2	4104×3006	3.45 μm	B/W

Table 4.2: List of cameras tested in the LIM setup.

The sensor of the largest FoV camera (UI-3202SE-M, *IDS*) proved to be larger than the used collimated beam diameter, meaning there was no way to utilize the full sensor area. This camera also proved challenging in terms of significantly increased data bandwidth and data storage requirements. These two facts, combined with very high cost, led to shift of focus to the smaller-sensor alternatives. The larger FoV could be interesting in future stages of the project, but can not be properly utilized in current proof-of-concept stage. Both the smaller IDS and Basler cameras

delivered very similar image quality and performance. However, after measuring for some time with both cameras, a decision was made to keep using the IDS models due to much better software support, officially available Python wrapper from the manufacturer and larger FoV. On the other hand, the Basler camera could find its use in low-cost models, thanks to its more attractive price (3- 4× cheaper). Since the color sensitivity in these cameras is realized by added Bayer filter array (RGBG) on top of the pixels, all of the RGB cameras effectively have only 25% red, 50% green and 25% blue pixels,. This virtually increases the effective pixel size by the factor of four (R,B) and two (G), which leads to reduced resolving capabilities. Since solely monochromatic illumination at a time is used in the current LIM, color-enabled imaging is not required and therefore not worth the trade-off in resolution. Comparison of captures of the same target with monochromatic and IDS camera models cane be seen in Fig. 4.9.

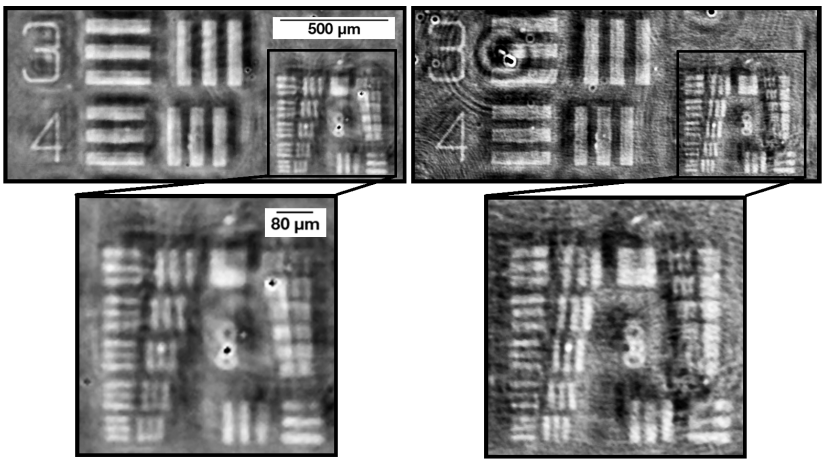

Figure 4.9: Multispectral (R+G+B average) OPD maps of 10 *nm* features of USAF target taken with IDS UI-3882LE-C (RGB camera, *left*) and IDS UI-3882LE-M (monochromatic camera, *right*). Smaller effective pixel size in case of the monochromatic camera leads to finer resolution.

4.3.4 Operating distances evaluation

Since the LIM is based on the the geometry of the LFM, there's a distance between light source and camera Z, a distance between the light source and sample Z_1 and a distance between the sample and camera Z_2 so that $Z = Z_1 + Z_2$ (Fig. 4.10). To maximize the available distance options and make the optical alignment easier, the oriented polarizers were glued directly onto the Savart plates. In the first test, Z_2 was changed, while keeping Z constant, i.e. moving the sample in the space between the Savart plates. The resolution target with 5 *nm* high silica structures was placed in three different distances from the camera: 26 *mm*, 15 *mm* and 5 *mm* (as close as allowed by the sample holder and Savart plate **SP2**). The captures (always back-propagated to correct distance) are shown in Fig. 4.11. There is a clear trend

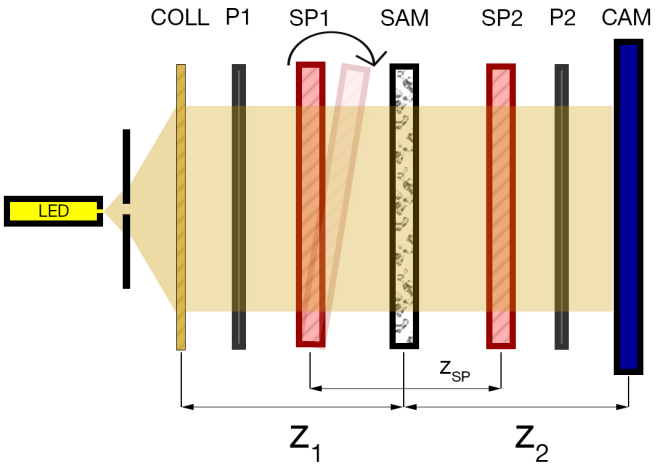

Figure 4.10: The LIM optical setup with highlighted distances between components.

between the distance from the sensor and the overall image quality. For the furthest distance of 26 *mm*, a loss of details and decrease in sharpness and resolution are significant and the small features can no longer be resolved. One of the explanations could be that the diffracted patterns propagate over a larger distance, therefore get very large and can not actually fit all the visible diffraction rings in the sensor field-of-view. That would lead to loss of higher-frequency elements of the signal and lacking reconstruction of details in the images.

This measurement confirmed that very low distances from camera improve the microscope readouts. However, there are still two limits imposed on the proximity of the sample and camera: **(i)** for the LIM configuration, a stack of polarizer and second Savart plate needs to be placed after the sample and **(ii)** non-zero distance from the sensor plane is needed to allow formation of Gabor hologram between the scattered and background light (see Chap. 2.5). Thankfully, those two requirements match well together. Therefore, the distance Z_2 in the final prototype design was be minimized and the sample was placed to the closest vicinity of the Savart plate **SP2** with glued polarizer, which in turn was placed directly on the camera sensor.

The second distance which was evaluated was Z_1, i.e. the separation between light source and sample. A temporary setup with easily movable upper block (containing collimator and Savart plate) was built to facilitate the experiment. The distance Z_2 was, in accordance with previous findings, minimized to 5 *mm* and the upper block was moved so that the reflective collimator distance (measured from the lip right above the threading) to sample plane was 4 *cm*, 6 *cm* and 8 *cm*. The results are shown on Fig. 4.12.

Fig. 4.12 does not show any strong correlation between the resolving power and light-sample distance. Compared to other images of the USAF resolution target, the overall quality of the captures is lower. This is mainly due to two reasons: **(i)** moving

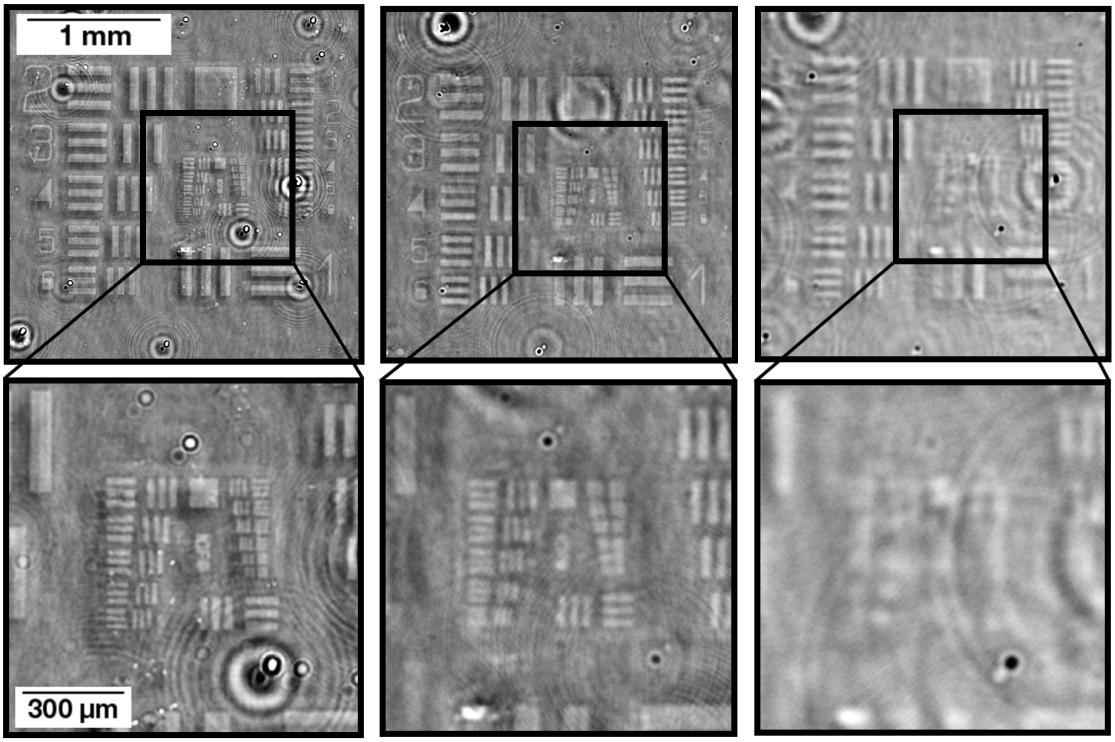

Figure 4.11: Multispectral (R+G+B average) OPD maps of 5 *nm* high silica structures of the resolution target placed 5 *mm (left)*, 15 *mm (middle)* and 26 *mm (right)* from the camera. There is a visible degradation in quality and resolution as the sample is moved further from the camera.

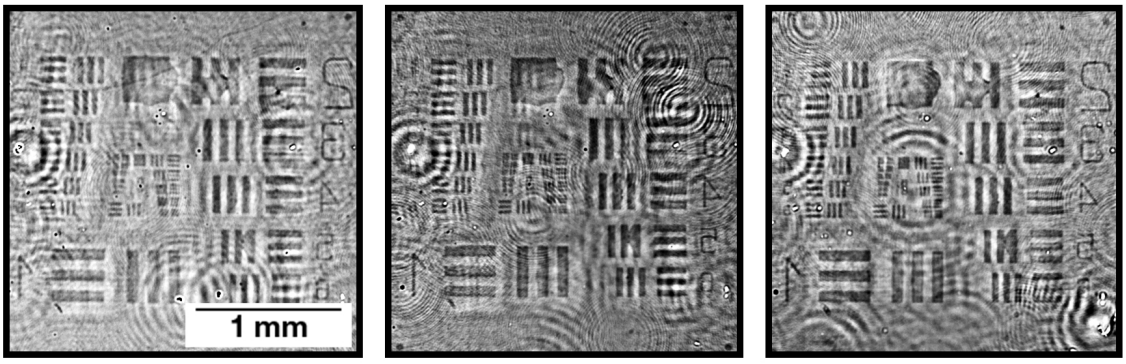

Figure 4.12: Single color OPD maps (green, $\lambda = 530$ *nm*) of 5 *nm* high silica structures of the resolution target with light source placed 4 *cm (left)*, 6 *cm (middle)* and 8 *cm (right)* from the camera. There is no visible degradation in quality and resolution as the light source is moved further from the camera.

the upper block inevitably causes a misalignment of the optics, slightly hindering the quality between measurements; **(ii)** only one illumination color (M530F2 ($\lambda = 530$ *nm*), *Thorlabs*) was used in this temporary setup, not allowing to average over multiple wavelengths to improve the signal-to-noise ratio. Some papers proposed

that longer distance between light source and sample leads to improved image quality in LFM since it increases the spatial coherence of non-coherent illumination [22]. In case of the LIM, no significant image quality change with different Z_1 distances was observed. The most likely reason for not observing improvement of resolving capabilites with higher distances (as was noticed by other authors in case of the LFM) is the use of collimated light in case of the LIM. Conventional LFM setups always use spatially filtered LEDs, which can be thought of as point sources. As the propagation distance increases, the spherical wavefront radius also increases and the wavefronts can be considered more planar with higher Z_1 distance. This is however not the case of LIM, where the wavefronts are planar independently to the propagation distance thanks to the collimation.

Based on the results, Z_1 distance can be selected based on the device size requirements, without any significant effect on imaging quality. Again, there are constraints limiting the minimal distance in the final device (such as tilting stage with **SP1**).

4.3.5 Thermal stability

During continuous measurements in a previous fully-enclosed prototype, gradually increasing artifacts were occasional observed. These artifacts had a signature of a profile gradient and dust particles were appearing over the field-of-view. This is a highly undesired effect hindering the measurement quality, as can be seen on Fig. 4.13.

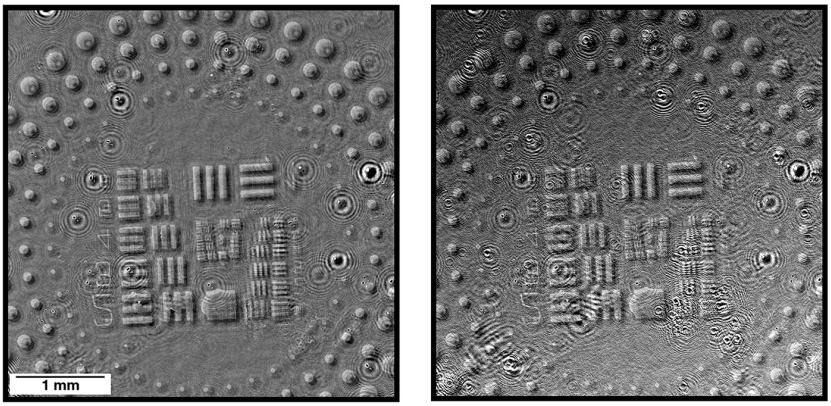

Figure 4.13: First image taken right after the reference (*left*) and image taken after 12 consecutive measurements (approx. 1 hour later). There is a significant increase in noise and the gradient appears across the field-of-view.

Because the LIM is a differential technique, every measurement is a result of the sample signal being subtracted from a reference (background) signal. During data acquisition, the camera heats up significantly and very quickly, as was verified by temperature probe measurements (Fig. 4.14). Assuming a start of the device with not warmed-up camera and taking a reference measurement, this reference is then subject to significantly different temperature conditions compared to the subsequent

measurements. Since the Savart plate **SP2** is in close vicinity to the camera, the heat could easily transfer to the stack of birefringent crystals and modify the birefringence of each of them to a various extent. As was experimentally verified by [55] and [56], the magnitude of birefringence $|\Delta n|$ of calcite crystals increases with increasing temperature. Presence of changing temperature gradients in the Savart plate could then cause a birefringence imbalance between the two joined crystals, modifying the shearing properties and optically misaligning the setup. This seems to be the case as such misalignment would explain sudden appearance of dust particles (improper subtraction) and increased overall noise level. It was also observed that the gradient is always in the same direction as the shear, further hinting on temperature-dependent birefringence being the cause.

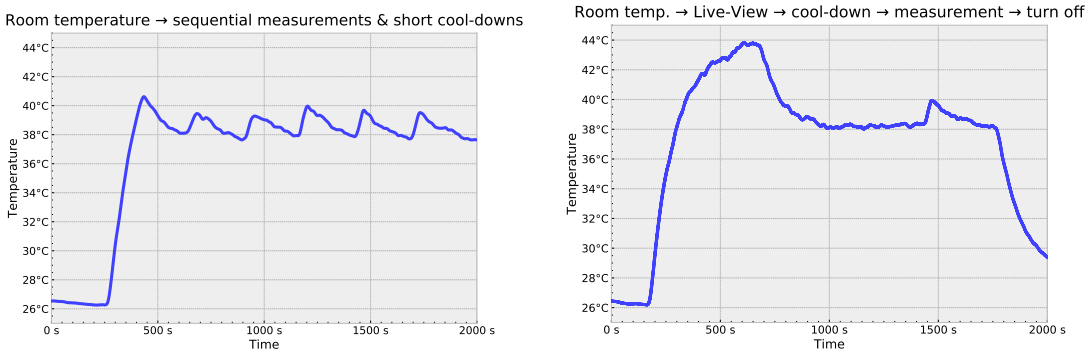

Figure 4.14: Starting from cold state of the camera, temperature was measured for multiple consecutive measurements (*left*) and when high-load "Live-View" was turned on (*right*). The increase of temperature in the initial phase is very steep.

For reasons stated above, temperature is the most likely explanation of the observed efects To alleviate the issue without the need for active cooling, the camera was placed in a free space, allowing surrounding air to cool it down. The reference measurement was always done after the camera was plugged in for short period of time and the time between subsequent measurements was set to be at least five minutes to allow the system to cool down to the standby state. After the implementation of these solutions, the effects were not observed anymore. For potential higher-frequency imaging, further passive (heat sink) or active (fan, thermoelectric cooler) elements could help stabilize the camera heating.

4.3.6 Extending software capabilities

The process steps of operating the LIM, including measuring and sample analysis, are fully automated using a Python software previously developed by members of my group (Optoelectronic, *ICFO*). To further extend the capabilities of the software suite, the code was rewritten from Python2 to Python3 and added some new functions:

i) **New camera drivers**, where the support was extended from one camera manufacturer to three by adding new control modules (IDS, Basler). The IDS module *IDSPyCam* was released on GitHub [57] as an open-source code to enable others programmers to use it.

ii) **LED and motor drivers** for the Upboard2 single board computer (with Linux) based on available open-source Python driver wrappers, enabling full control over the measurements from only one single computer and one single app.

iii) **Exporting capabilities** for image profiles (.csv files) and full captured images (graphics and array formats), to enable additional data processing.

iv) **Manual refocusing GUI** to give the end-user more convenient way to digitally refocus the acquired images. The advantage of this new GUI lies in the fact that it enables to refocus only on a desired part of a recorded image, greatly enhancing the focusing speed and user experience. Area-of-interest is simply selected by click-n-drop selection in the GUI and then, the refocusing uses the same back-propagation algorithm as the full-field, only on selected subset of the electric field. Once the correct focus is found, it can be easily applied to the full field-of-view.

v) **AutoExposure** function that automatically sets the optimal exposure times for specific camera and illumination. This is performed by measuring without any sample present in the device, computing the OTF curves and rescaling the camera exposure parameters based on the maxima of the curves for each color. The goal is to have mean pixel value of the brightest frame at 85% of camera's full dynamic range (see Fig. 4.15).

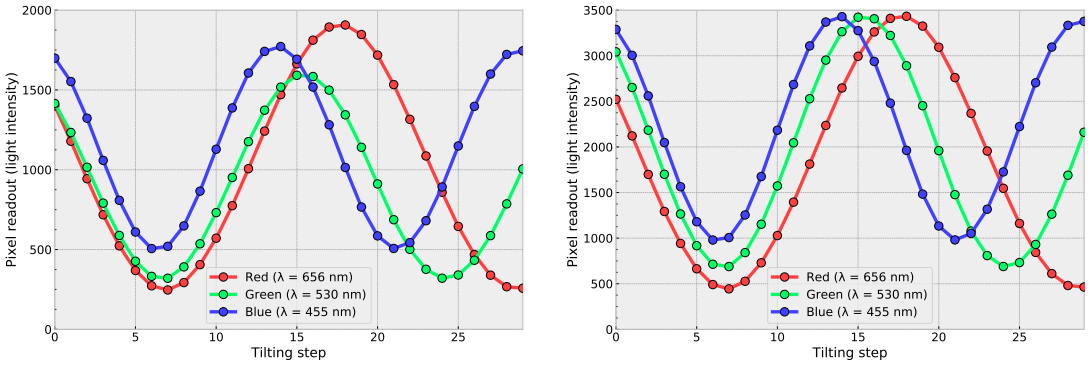

Figure 4.15: An example of a set of OTF curves with manually determined non-optimized exposure time (*left*) and when the exposure time is determined by the AutoExposure function (*right*).

Various other minor functions (optional scale bars for images, quick sample/project delete buttons for unsuccessful measurements, camera pixel binning) were also added to the software suite.

4.3.7 Summary of setup optimizations

Based on the results from previous sections, the final setup version was built with collimator-to-sample distance $Z_1 = 8cm$ and sample-to-camera distance $Z_2 = 5mm$. The IDS UI-3882LE-M monochromatic camera was used, with extra space left below the chip to improve heat dissipation. The multicore fiber bundle (core diameter 50 μm) was used for all the measurements, with only central core being used for measurements that didn't require angled illumination. The camera exposure time was adjusted for each color automatically prior to the measurement by using the AutoExposure function. The whole optical setup can be seen in Fig. 4.16.

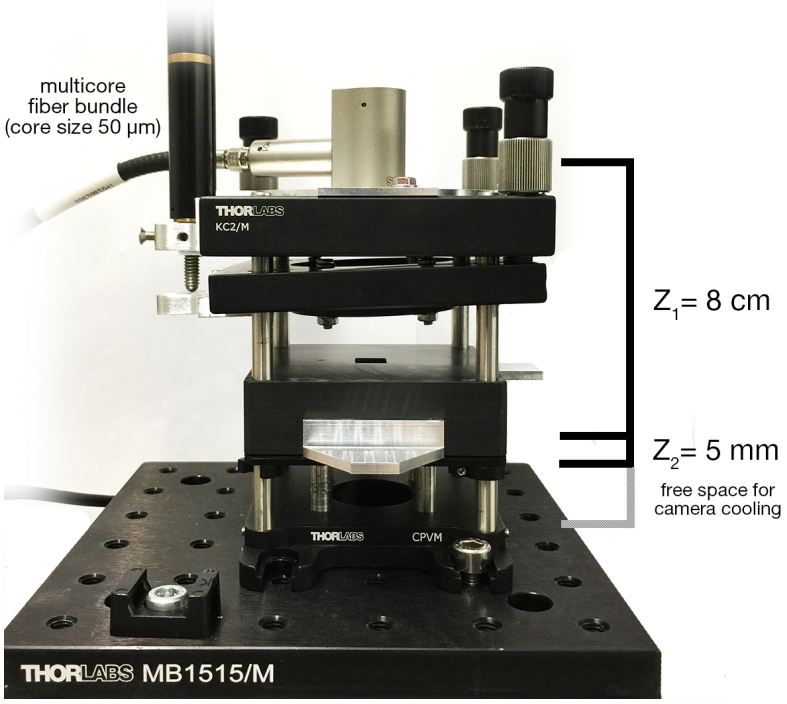

Figure 4.16: Photo of the final optical LIM prototype with highlighted distances.

4.4 Holographic autofocusing

To obtain optimal signal-to-noise ratio and readouts accurately describing the measured sample, proper focus of the reconstructed OPD maps is necessary. Focusing can be either done manually by the user, or automatically by a program. Unfortunately, autofocusing using conventional focusing algorithms might not work properly for holograms. Unlike in photography, the out-of-focus image is diffracted instead of blurry (the rings on image change size, but remain sharp).

There are less robust, but very fast approaches in case some assumptions can be made about the measured objects. For example, for well defined structures such as microdots, simple pixel value thresholding followed by counting the amount of pixels above the threshold can provide instant focus distance estimate. This is based on

the fact that out of focus features blur into the background, gradually losing feature height. By setting the threshold slightly below expected feature height h, only in focus objects will have higher number of above-threshold pixels around the feature height. These can be counted and used to estimate the focused distance z_f. This approach is demonstrated in Fig. 4.17.

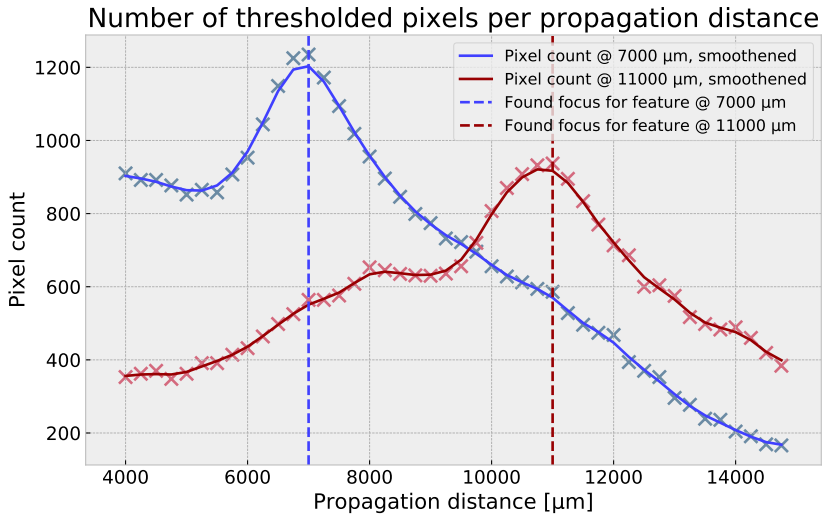

Figure 4.17: Plots for thresholded pixel count ($OPD > 3\ nm$) in relation to the propagation distance, tested on two features (10 nm silica dots ($\varnothing = 200\ \mu m$), expected OPD $\approx 4\ nm$) in one sample, each with different focus height. The graphs show highest number of pixels above the threshold in the focus distance z_f for both the features. The curves were smoothened with one-dimensional Gaussian filter.

Since this approach is very quick (calculation on pre-propagated data takes $< 1\ s$), the thresholding parameter can be adjusted by the user with quick response time until the focus plane estimate is returned. This approach performs really well mainly on smaller areas of interest. The Gaussian-like shape of the curves around the peaks also seems to get more narrow for closer focus distances, hypothetically offering higher focusing precision for lower propagation distances. In similar fashion, calculation of pixel value variance for images processed with edge-enhancing filters (such as Sobel filter) also works as a quick estimate for focus plane. This approach is later utilized in Chap. 5 (Sec. 5.2.1).

In more robust approach developed by Terborg [43], the focus plane z_f is found automatically by looking at the rate of change between OPD and transmittance maps in two consecutive focus planes z_n, z_{n+1} while scanning over a given range of focus distances z (see Fig. 4.18). This method uses both OPD and transmittance maps in conjunction to reach higher accuracy in estimating the focus plane. First, mean pixel differences Δ_{OPD} and Δ_{Trans} are calculated for consecutive frames for both OPD and transmittance maps. The curves are then smoothened using one-dimensional Gaussian filter (Fig. 4.18, *upper part*). Both the curves are normalized

using formula:

$$\hat{\Delta} = \frac{\Delta - \mu(\Delta)}{\sigma(\Delta)} \tag{4.5}$$

where Δ represents the differences, $\mu(\Delta)$ is the mean value of these difference values and $\sigma(\Delta)$ is the standard deviation of the difference values. Following that, second derivatives of the normalized curves Δ''_{OPD} and Δ''_{Trans} are numerically calculated for visualization Simultaneously, the second derivative Δ''_{comb} of the combined function

$$\Delta_{comb} = \pm\frac{\hat{\Delta}_{OPD} - \hat{\Delta}_{Trans}}{2} \tag{4.6}$$

is calculated. The sign of the fraction depends on the predominant nature of detected features (+ for phase objects or − for intensity objects). In the final step, maximal value of the set $\max(\Delta''_{comb})$ is found and its argument is returned as the focus value (Fig. 4.18, *lower part*).

There is also wide array of different approaches already available for autofocusing digital holography that utilize more complex and robust methods. These include (among others) sparsity-based methods [58, 59, 60] and deep learning based methods [61].

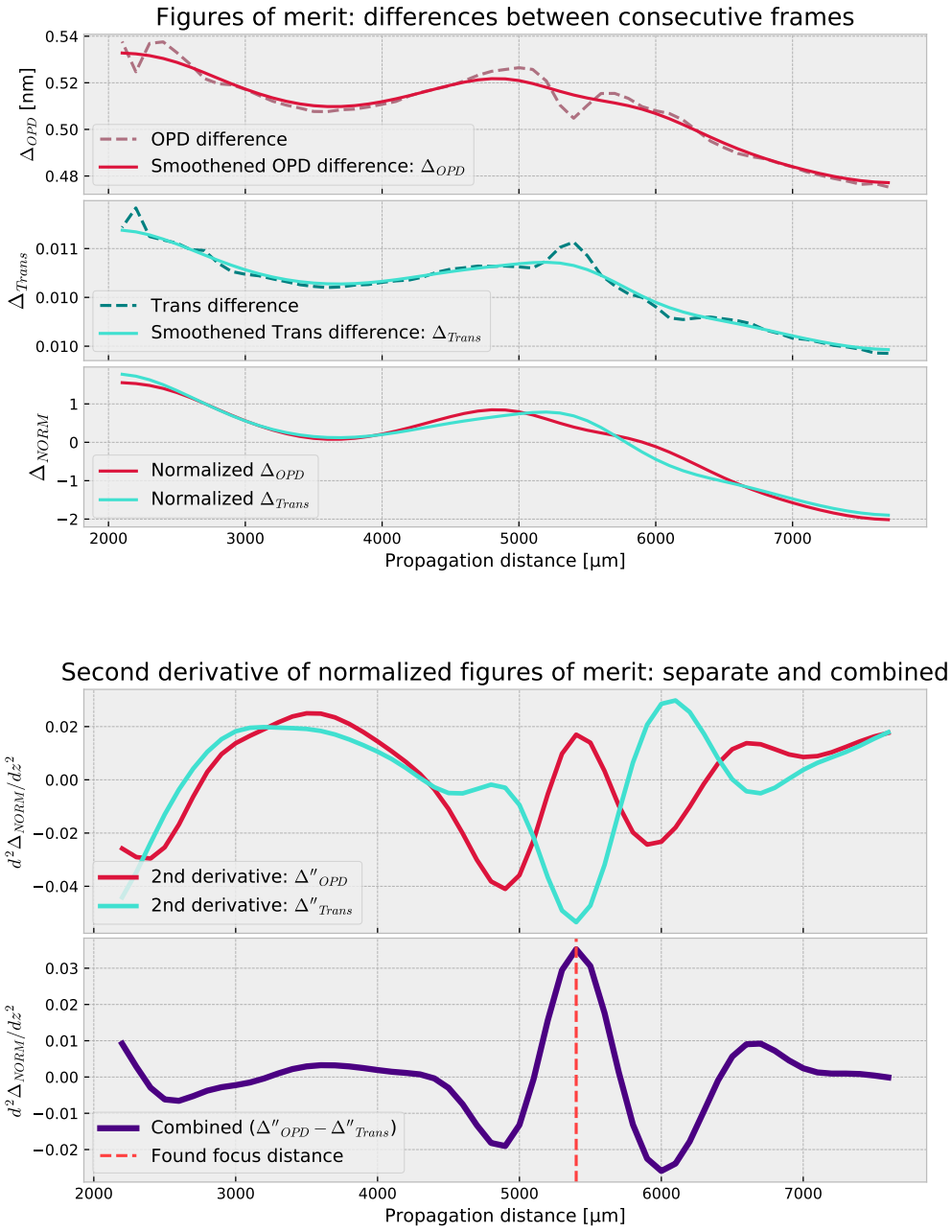

Figure 4.18: Figures of merit for the robust autofocusing approach.

4.5 Enhancing resolution in single-plane LIM imaging

To further increase the resolving power and signal-to-noise ratio, multicore fiber bundle (Sec. 4.3.2) can be utilized. Using the bundle, the full measurement (with and without sample) was repeated seven times (once for each core) using batch capture

algorithm. Optimal exposure time was estimated beforehand and set constant for all the captures. The 21 electric fields (7 fibers, 3 colors each) were calculated after measuring using the PSI method. Each electric field was then propagated to $\pm z_f$ to enable twin image suppression. In each of these two focus distances, the colors were first combined together by averaging to obtain multispectral maps. Following that, the shifts between multispectral maps were calculated for each fiber core using cross-correlation with subpixel precision, both in $+z_f$ and $-z_f$. Following that, all the frames were upsampled (x2) using cubic interpolation and unshifted using the previously found shift values with Fourier-domain based shifting algorithm to enable subpixel shifts. The unshifted upsampled multispectral frames from angled illumination and central frame were then all combined together and averaged to obtain high-resolution maps in both $\pm z_f$ focus distances. In last step, twin image suppression algorithm (described in 3.4) was applied, combining images from both real and conjugate plane and resulting in one clean high resolution OPD and transmittance map in the desired focus distance. The full procedure is illustrated on Fig. 4.19.

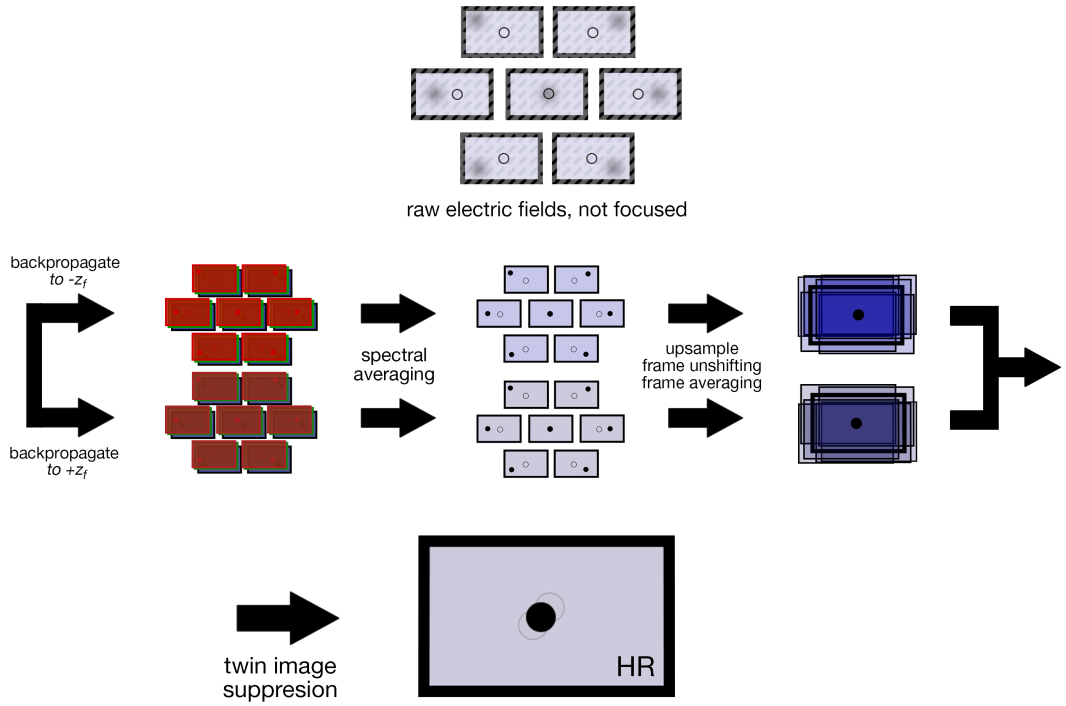

Figure 4.19: Data processing steps of improved single-depth LIM imaging.

4.6 Results and discussion

Using the measurement procedure described in Sec. 4.2, OPD maps were recorded for the resolution target (Sec. 4.1) with feature height $h = 5\ nm$ using three illumination colors: red ($\lambda = 656\ nm$), green ($\lambda = 530\ nm$) and ($\lambda = 455\ nm$). A simplified data processing steps scheme can be seen in Fig. 4.20. As can be

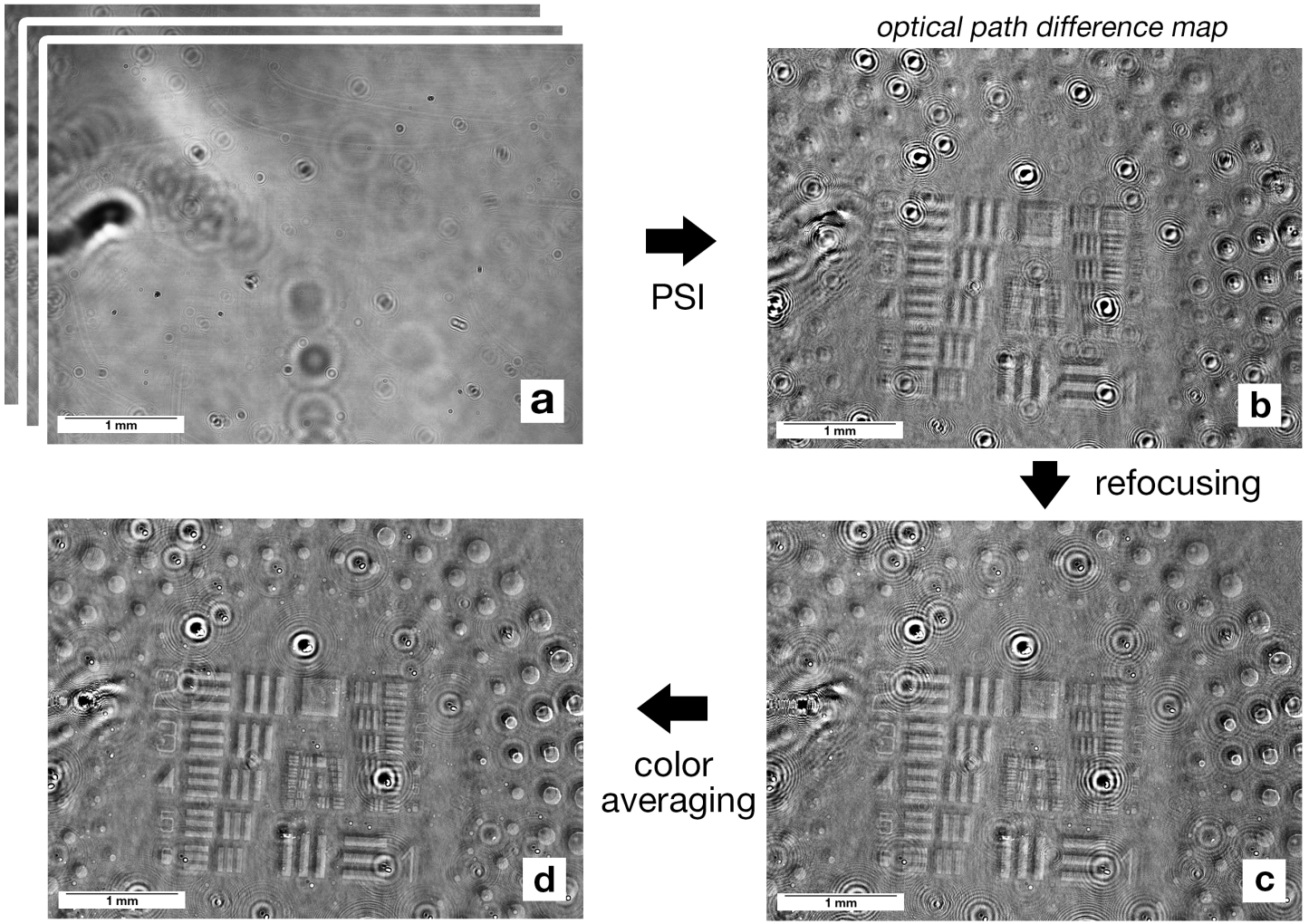

Figure 4.20: Data processing steps in the LIM. The raw hologram (a) is processed by in multiple steps.

clearly seen on Fig. 4.20(a), the transparent silica structures are basically invisible for a non-interferometric lensfree microscope. The most notable features in the first frame are diffraction rings created by absorptive dust particles in the setup, while the absorption of silica patterns is below the noise level. In the second frame, reconstructed (unfocused) OPD map is returned by the PSI method. This optical path difference is directly proportional to the phase difference introduced in the sample

$$OPD = h \cdot \Delta n = \frac{\lambda \cdot \Delta\varphi}{2\pi} \tag{4.7}$$

where h is the feature thickness, Δn is the refractive index difference between examined material and surrounding medium, λ is the illumination wavelength and $\Delta\varphi$ is the phase shift introduced by the material. Using this formula, the phase shift can be easily calculated from the OPD with the knowledge of illumination wavelength. The reason OPD maps are returned instead of pure phase maps is the OPD independence on used illumination. Since the LIM is mainly used to measure height profiles of transparent structures with multiple illumination wavelengths, use of OPD enables multispectral averaging and allows direct readout of feature height with the use of simple calculations. In this OPD map, silica features are already significantly more pronounced and easily visible. However, the whole image is out of focus since the PSI method reconstructs the light electric field in the camera plane $z = 0\ \mu m$. Because of that, the readout of values does not represent the real measured values and small features are completely diffracted and hence not visible. The next step is focusing of the image using the numerical Fresnel diffraction backpropagation. To focus correctly, the knowledge of focus plane z_f is needed. As stated previously, this can be found by manual focusing or automatically using autofocusing algorithms. The propagation distance was found manually to be at $z_f = 5500\ \mu m$, while the robust autofocusing approach used on the central part of target returned focus value of $z_f = 5400$, which is in very good agreement. Finally, all three colors were propagated to z_f and combined by averaging. It can be easily seen that the color averaging significantly improves the signal-to-noise ratio of the readouts. One of the reasons is that out-of-focus features exhibit differently sized diffraction rings for different illumination colors. When diffraction rings of the same feature for multiple (indivisible) wavelengths are summed up, they effectively cancel each other out due to the different spatial frequencies of the fringes. The OPD profile of a set of features is shown on Fig. 4.21.

It is clearly visible that the response of a LIM has a form of two shifted images, separated by the shear distance s and having the same magnitude and opposite sign. Each of these rectangular features can be seen as the peak from 0 nm to approx. 2.5 nm, while the twin images show as valleys from 0 nm to approx. -2.5 nm. This means the optical path difference introduced by these features is ≈ 2.5 nm. Knowing the refractive index for silica ($n_{SiO2} = 1.46$ for $20°C$ and $\lambda = 530$ nm), the

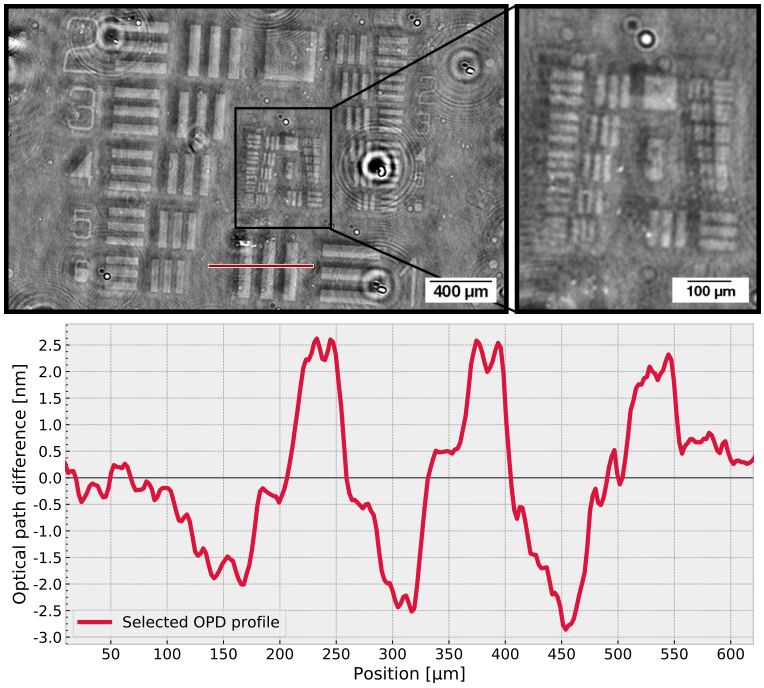

Figure 4.21: Multispectral average OPD map of the resolution target, with cutout of central part to show the smaller resolvable features *(left)* and shown OPD profile *(bottom)*. It can be seen that the real image peaks are in the range of $\approx 2 - 2.5\ nm$, which is the expected response of features of height $h = 5\ nm$.

feature height can be estimated from the formula:

$$h = \frac{OPD}{|n_{air} - n_{SiO2}|} = \frac{2.5\ nm}{0.46} = 5.43\ nm \tag{4.8}$$

The expected value for $h = 5\ nm$ would be $\approx 2.3\ nm$. Simultaneously, the feature height was not tested using high precision methods (such as AFM) and therefore is only estimated from the parameters during the making process. The finest resolvable spatial features (Fig. 4.21, *right*) are in the range of $\approx 25\ \mu m$, which is significantly below the resolving capability of ordinary light microscopes. Unfortunately, this is a trade-off in all kinds of lensfree microscopy due to the use of non-focused light beams. To improve the resolution of the single-plane images, additional data from multicore fiber bundle can be used. Following the steps highlighted in Sec. 4.5, upsampled (x2) high-resolution map with twin image suppression were constructed. The difference is shown on Fig. 4.22 with the zoom in on all image processing steps (single color capture, multispectral average and multicore enhanced resolution) shown on Fig. 4.23.

It can be seen that the multicore enhanced OPD map has increased resolution, with the small ICFO letters clearly visible and features with smaller dimension in the range $\approx 10\ um$ being resolvable in the zoomed in cutouts. Simultaneously, due to

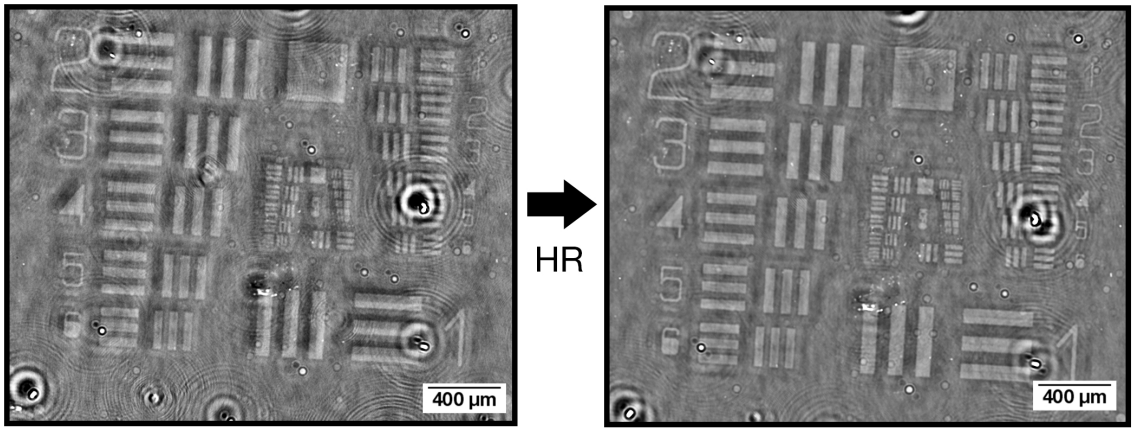

Figure 4.22: Comparison of image quality prior and after enhancing the resolution using data from multicore fiber bundle.

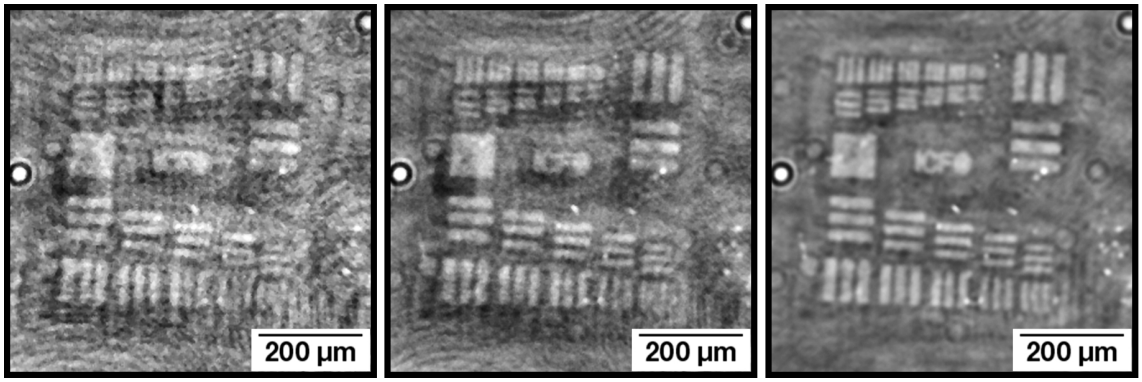

Figure 4.23: OPD map cutouts (scale -5 to 5 nm) from single frame and single color *(left)*, single frame multispectral average *(middle)* and upsampled high-resolution reconstruction *(right)*.

the averaging nature of the process, the noise was lowered over the whole field-of-view. The twin image suppression step makes the shape of features more defined, especially for the small ones. The out-of-focus dust particles clearly show how the twin image suppression algorithm creates a second twin image while improving the signal-to-noise ratio. When feature profile is rendered (Fig. 4.24), it can be seen that the twin image values (under zero) now have lower magnitude. The peak value readouts are also lower, peaking at OPD values of $\approx 2\ nm$.

To investigate this phenomena, OPD profiles were rendered for the real image plan ($z = z_f$, Fig. 4.25), conjugate image plane ($z = -z_f$, Fig. s4.26) and for the final step of twin image suppression (Fig. 4.27, where the twin image is shifted and subtracted from the real image.

From the process steps, it can be seen that the reduced values occur in the last step and not in the multiframe averaging. One of the possible explanations could be the presence of two negative (half-magnitude) twin images in the background that

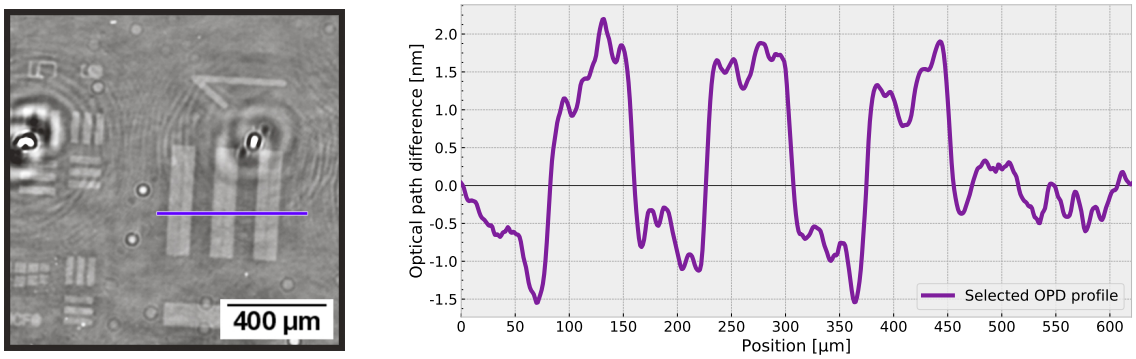

Figure 4.24: Cutout from the high-resolution reconstructed OPD map with twin image suppression. It can be seen that the profile height is lower in comparison to the non-cleaned version

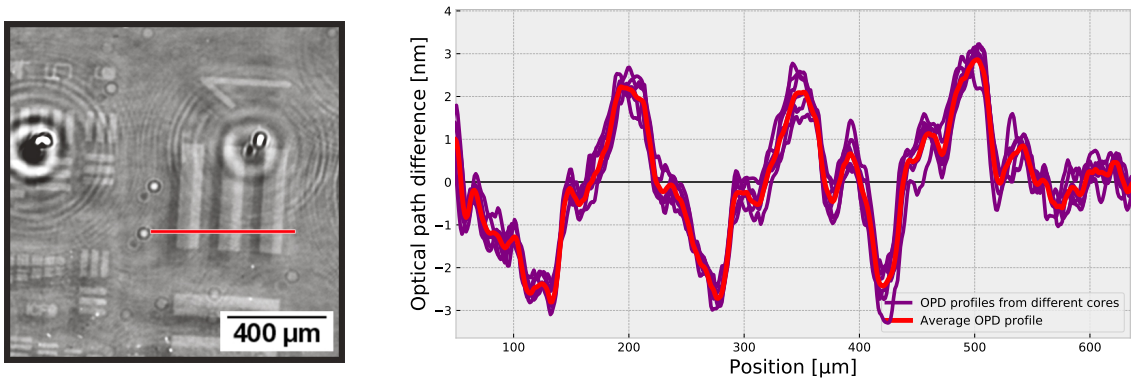

Figure 4.25: Cutout from the enhanced resolution OPD map, focused in real plane *(left)* and OPD profile of highlighted area for all the fiber cores (purple) and their average (red) *(right)*. It can be seen that the fiber average does not significantly reduce the readout values.

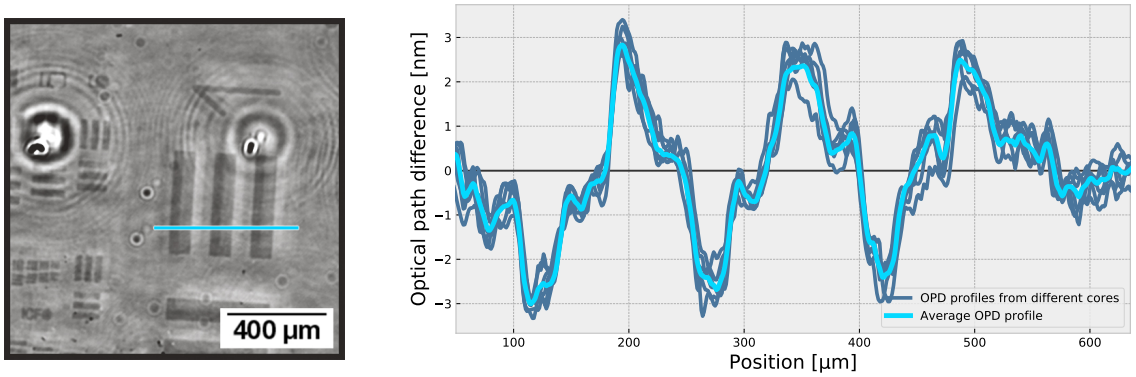

Figure 4.26: Cutout from the enhanced resolution OPD map, focused in conjugate plane *(left)* and OPD profile of highlighted area for all the fiber cores (gray blue) and their average (blue) *(right)*. It can be seen again that the fiber average does not significantly reduce the readout values.

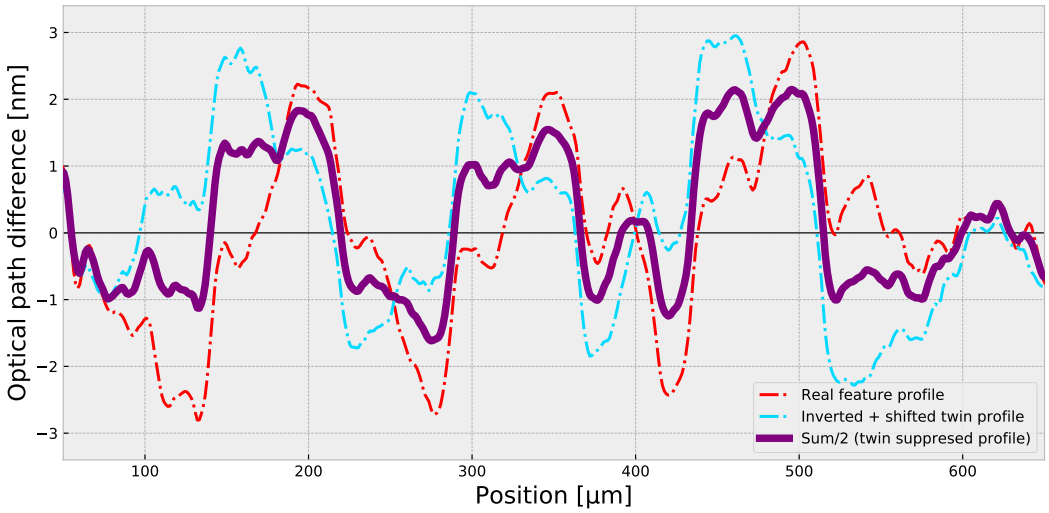

Figure 4.27: Plot of real plane profile (red), inverted and shifted conjugate plane profile (light blue, see Sec. 3.4 for more information) and their average (purple), which is equal to the profile of image with applied twin image suppression It can be seen that the lower readout values are caused by this twin suppression step.

overlay with the feature from two sides and reduce the OPD profile. This shows that further fine tuning is needed for the algorithm to reproduce real values. In case more precise OPD readouts are needed, the advantage of higher resolution from multiframe averaging can still be used, without the final unghosting step.

5 Depth-resolved LIM imaging

The main goal of this chapter is to introduce depth resolving for objects and structures imaged in the LIM. The capability to resolve the depth information of objects is the first step towards full three-dimensional tomographic imaging. Generally speaking, there is a multitude of approaches that can be applied to reconstruct 3D information of a sample in lensfree microscopy, such as:

i) classical tomography, relying on filtered backpropagation (inverse Radon transform) and rotation of imaged object [62];

ii) acquiring images with multiple-angle illuminations and using filtered back propagation [28, 63, 64, 65];

iii) shifting of samples in the z-direction [30]

iv) wavelength scanning [66];

v) reconstruction of the z-stack via backpropagation and use of feature recognition [67, 68, 51];

vi) iterative methods (such as Fourier Ptychography) [69].

Since the LIM is based on the LFM, these methods offer interesting research directions for enabling three-dimensional quantitative phase imaging. Utilizing the LIM components not present in the general lensfree setups, multiple depth resolved imaging approaches are developed and discusses in this Chapter.

5.1 Measured multilayered 3D sample

To verify the method for depth resolving, special 3D specimen was designed that consisted of multiple (up to 4) layers of glass substrate. In each layer, a simple non-periodic pattern of transparent silica dots is evaporated in such a pattern that the dots don't overlay when stacking. Those glass substrates are then stacked using aluminum holders and measured with the LIM. The spacing can be adjusted to suit the needs and desired sample separation. Two batches were prepared, first with dot diameter $\varnothing = 200\ \mu m$ and second with $\varnothing = 50\ \mu m$.

5.1.1 Computer-simulated multilayered datasets

Using models described in Sec. 3.5, a synthetic representation of a multilayered sample is created. In the first step, a planar wavefront with modified Gaussian profile is generated. Then, the wavefront is propagated through a sequence of free

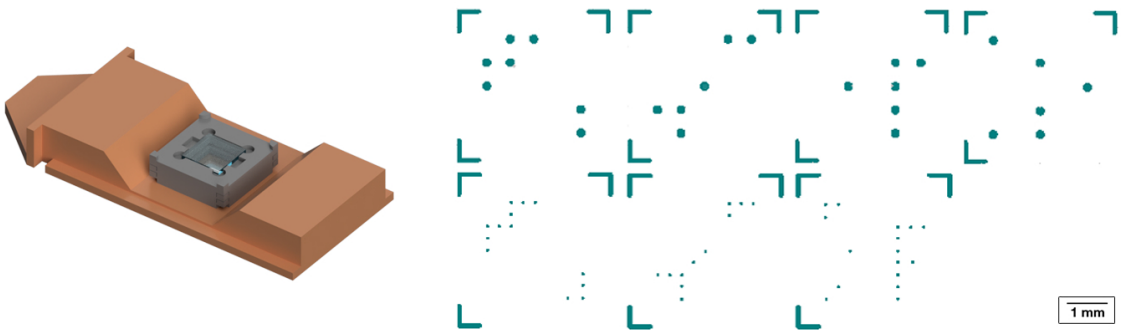

Figure 5.1: Render of designed 3D sample holder *(left)* and lithography mask showing all the dot patterns *(right)*.

spaces, optical components and phase delays $\Delta\varphi$, representing the behavior of a real sample.

First, the reference wavefront was synthesized for single illumination wavelength using following simplified pseudocode:

```
EField = Collimated_Light(wavelength)
EField.Polarizer(45 deg)
EField.Propagate(4000 um)
EField.Polarizer(45 deg)
EField.Propagate(7000 um)
EField.AddNoise()
return EField
```

Following that, the synthetic sample measurement was generated. First, two binary masks with dot patterns (upper and lower layer) were created in graphical editor to represent the location of the dots. Then, the electric field was constructed using following pseudocode:

```
EField = Collimated_Light(wavelength)
EField.Polarizer(45 deg)
EField.Phase_Step(OPD_Step=10 nm, Mask=upper_sample_mask)
EField.Propagate(4000 um)
EField.Phase_Step(OPD_Step=10 nm, Mask=lower_sample_mask)
EField.Polarizer(45 deg)
EField.Propagate(7000 um)
EField.AddNoise()
return EField
```

The resulting OPD maps for in-focus points can be seen in Fig. 5.2.

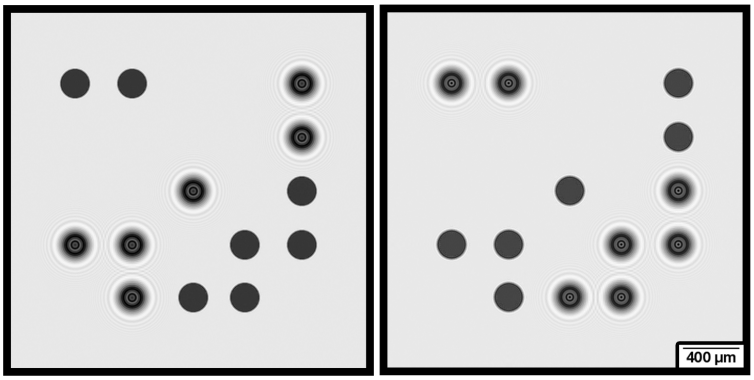

Figure 5.2: OPD maps of simulated two-layer dataset (feature OPD = 10 nm) with same dot pattern as the real sample. Focused in $z = 7000$ μm *(left)* and $z = 11000$ μm *(right)*.

5.2 Single-frame depth resolving *via* backpropagation

In this section, the data from single illumination angle are used to resolve the distribution of multiple phase objects, located in different z planes in the sample value. The three-dimensional positions of the objects are determined using the autofocus approach, first introduced in Chapter 4.

5.2.1 $M \times N$ sliding window autofocusing

As was shown in Sec. 4.4, it is possible to algorithmically find a focus plane of the whole OPD map. However, such approach is suitable only when **all** of the sample features are in single focus plane. To extend the autofocusing approach to multiple objects in different planes, a *sliding window* method can be used. In computer vision, a sliding window is a sub-list that runs over an underlying list [20]. This method can be used to scan over the whole field-of-view, finding the focus position for each sliding windows position.

In the first approach, the light electric fields U obtained from simulations and PSI method were backpropagated using the numerical backpropagation algorithm to n evenly distributed focus planes covering the full volume of the sample. Each of the n images was then divided into $M \times N$ smaller regions and scanned through by the sliding window. The next task was to find the best focused z-distance for each of the regions. To accomplish this, the maps were convolved with a Sobel operator to pronounce edges (see Sec. 2.4), followed by total variance measurements for each region along z. This is based on the assumption that in ideal case, focused OPD images consist only of pixel values equal to either zero (background) or h (feature). Assuming the feature fills 50% of the sliding windows, there is equal amount of 0 and h pixel values. Statistically, values of such dataset are all spread far from the

average $h/2$, which results in high variance. On the other hand, OPD profiles around diffracted features can be approximated by the square of first kind, first order Bessel functions [70]. The behavior of these functions can be (for simplicity) likened to the behavior of attenuated sine functions. In such case, more values are spread closer to the average and the variance of such set is thus lower. For this reason, the z-distance with maximal variance was selected as the focused plane for each sliding window position.

First, the method was tested on a **simulated** dataset consisting of two layers of dots. The algorithm scanned through the picture with $M = N = 10$ (in total 100 sliding window positions). For each position of the sliding window, the Sobel filter was applied and the overall variance of the window was calculated. The region variance values along the stack were recorded and the highest variance was returned as the focus position, as depicted on Fig. 5.3).

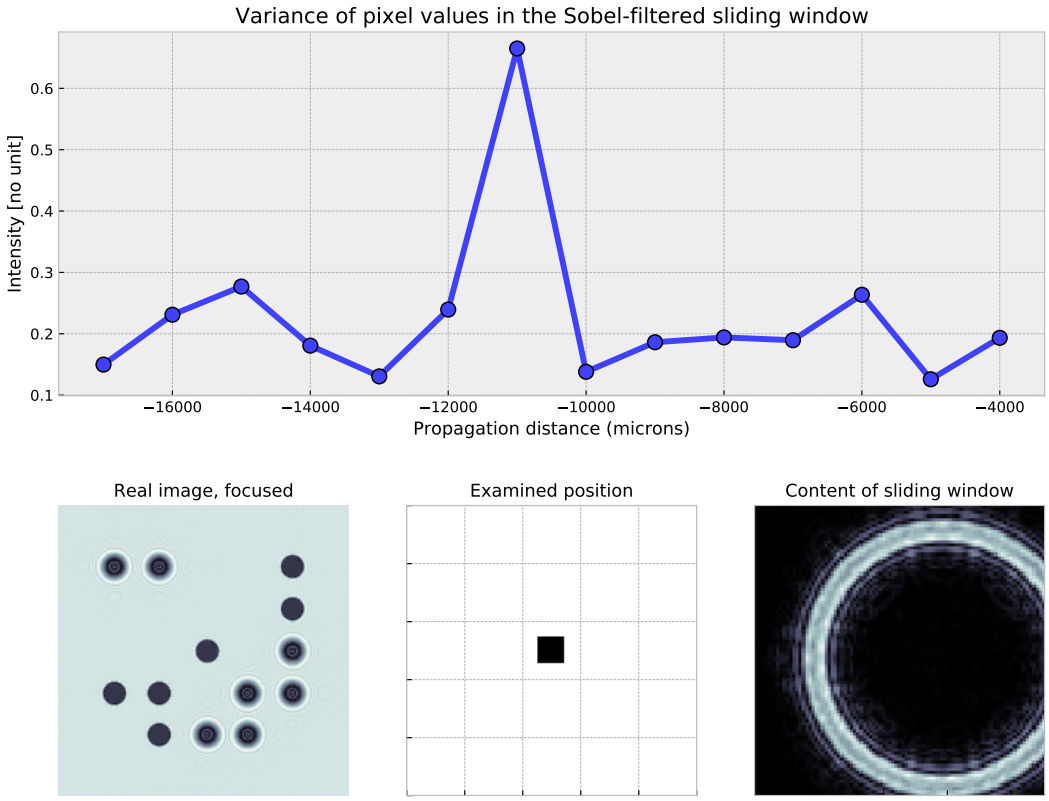

Figure 5.3: Schematic of the $M \times N$ scanning algorithm used on simulated dataset. The variance of all pixels in the edge-enhanced sliding window *(bottom right)* is calculated, and the maxima is used to return the focused plane of the sliding window (position shown *middle bottom*). The whole image, focused to the same propagation distance, is also shown on the *bottom left*. The dimensions of the full field-of-view of the simulated image are 2.4×2.4 *mm*.

It's clearly visible that when a focus plane for a simulated feature is encountered

by the sliding windows algorithm, the pixel value variance returns a maximal value. After the focus plane was calculated for every position of the sliding window, a layer-by-layer view of the sample was constructed from the acquired data by stitching all the in-focus parts of the image (Fig. 5.4).

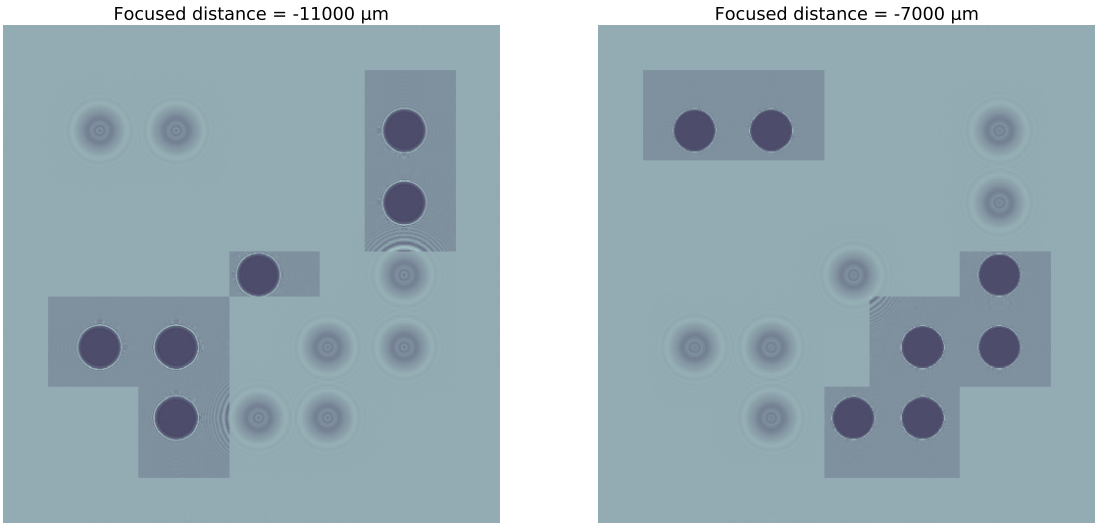

Figure 5.4: Areas detected as being in focus by the algorithm ($M = N = 10$) are highlighted by darker color.

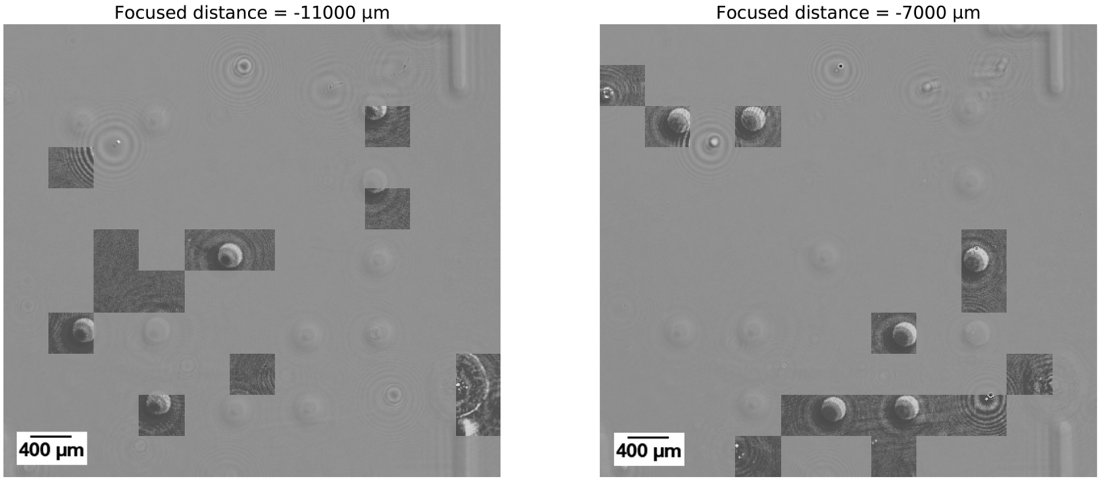

Figure 5.5: Areas detected as being in focus by the algorithm ($M = N = 10$) are highlighted by darker color. Some of the features were not detected.

Significant advantage of this method is in the execution speed. While calculations of the back-propagated stack are time-consuming, the algorithm is capable to perform the sliding windows operation, autofocusing and stitching in the matter of seconds. As can be seen on Fig 5.4, the algorithm performed very well on the simulated dataset using the Sobel filter and variance maxima lookup. Unfortunately, the performance on a real dataset (with same pattern) was weaker, as depicted on Fig.

5.5. While the method was capable of finding most of the dots (four out of five in one propagation distance and six out of seven in the other), it didn't find all of them in both cases. Some false positives (background) were also returned. Currently, the approach is mainly constrained by the used non-robust autofocusing method. Improvement of the quick autofocusing algorithm would give this method a very high potential for quick (albeit rough, thanks to the use of sliding windows) feature depth recognition. Second possible improvement could be in use of multiple sliding windows sizes and then crosschecking the results for those as verification. This approach was also tested and preliminary results were obtained (Fig. 5.6), however, further work on it is required.

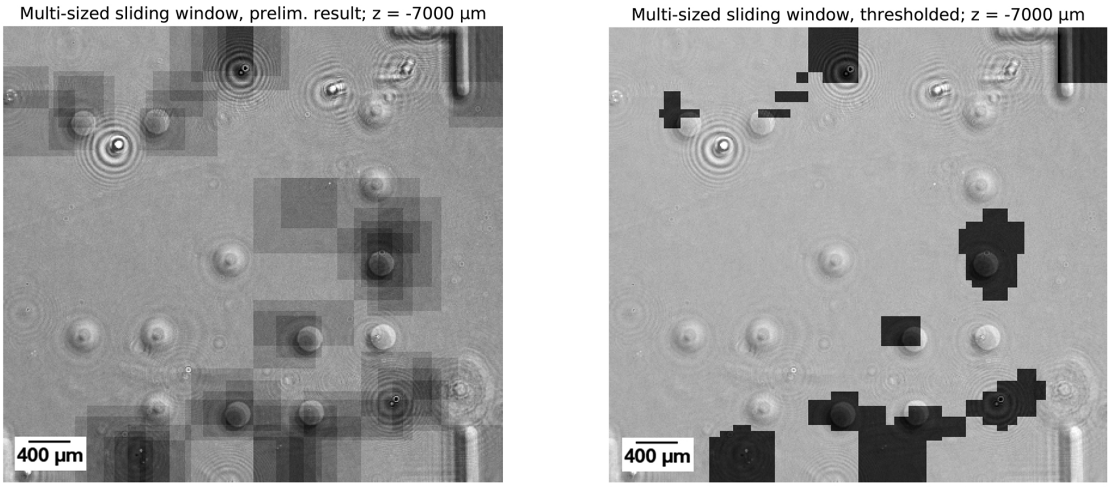

Figure 5.6: Overlay of selected areas *(darker)* and the real image on the background for comparison. Some of the features were not detected.

5.3 Multi-frame depth resolving *via* shift tracing

With the use of a multicore fiber bundle (Sec. 4.3.2) and reflective collimator, we can extend the imaging capabilities of the LIM and acquire images of measured sample from multiple angles without the need to employ any additional moving stages or other mechanical or electro-optical elements. These extended datasets contain additional information about the spatial distribution of features in the sample. The multiframe models proposed in this Section rely on following assumptions:

i) Illumination with different fiber cores coupled to reflective collimator creates angled collimated beams with slightly different propagation direction (see Section 4.3.2).

ii) The propagation direction angle, measured from the central beam direction, is the same for all the angled beams.

iii) Illumination from different cores provides the same overall light intensity. This means that a pixel projected by the certain position in the sample should have the same readout value across all the measurements with angled illumination.

iv) Illumination from different cores causes object projections to shift, with the magnitude of the shift being linearly dependent on the distance of the object from the camera.

v) For a given illumination angle, the direction of the projection shift for all the objects is the same.

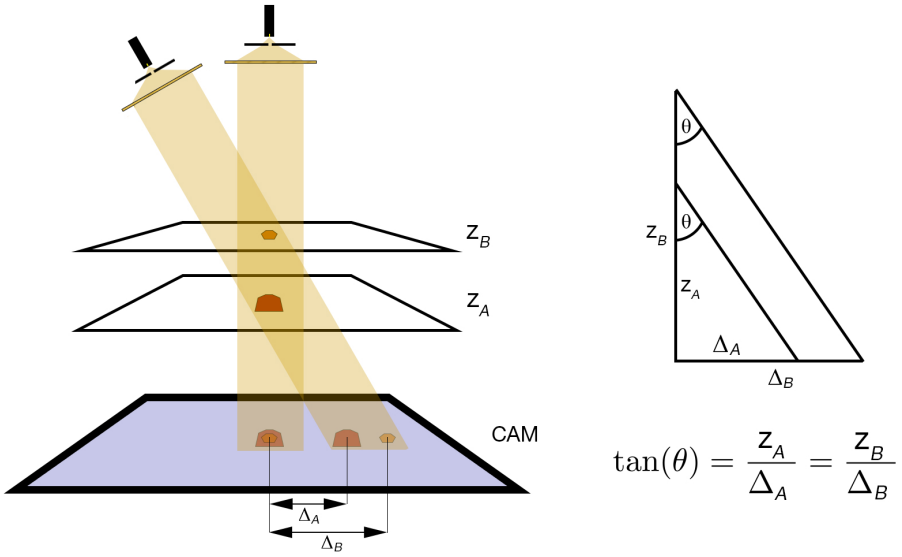

Figure 5.7: Schematic showing how different illumination angles cause different shifts of features in the camera plane *(left)* and simple geometrical model of the situation *(right)*.

All these assumptions combined mean that the projection of every feature with non-zero distance from the camera will be shifted in all the angled illumination frames. The displacements of feature projections created by different fibers can be used to calculate the feature distance from the camera (Fig. 5.7). For each illumination angle, each feature's projections will move further from the center as the feature-camera distance increases, with the movement for given illumination angle being in one particular direction.

Obtaining the information of these geometrical shift for feature projections thus gives the ability to resolve the depth position of the feature. In the following sections, different approaches are proposed to obtain this information.

5.3.1 Uniform shift tracing method

The simplest method assumes that all the features of interest are in a single focal plane z_f. Then, the algorithm takes all electric fields, extracts the OPD maps and calculates the shift between those (Fig. 5.8). Using the known relation between shift magnitude and z-distance (Eq. 4.3), the focus plane can be estimated.

To find the shift $\delta = (\delta_X, \delta_Y)$, multiple approaches were tested:

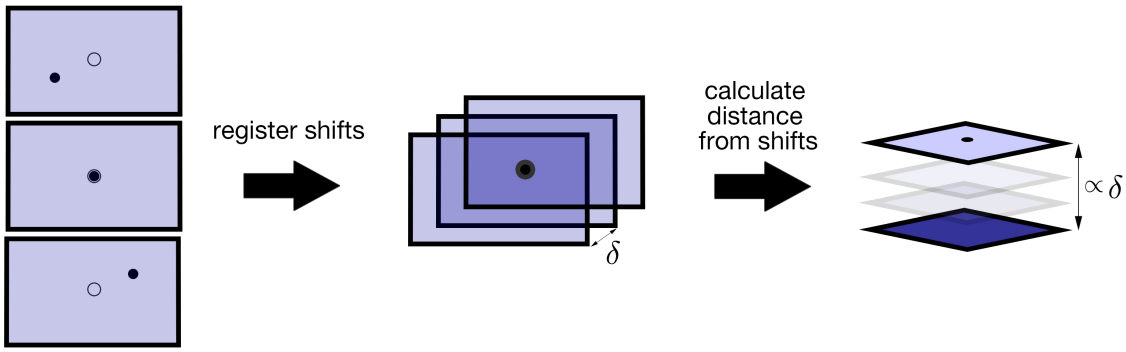

Figure 5.8: Steps of the uniform unshifting algorithm.

i) *subtractive approach*, where one image is kept static while second image is moved with pixel increments around in a user-defined range. For every movement, the images are subtracted and the overall pixel value sum of the difference is recorded. After scanning, the position with lowest sum is returned (best subtraction);

ii) *cross-correlation in Fourier space* as proposed by [71] and implemented in the *scikit-image* Python library [72].

First, an unfocused ($z = 0\ \mu m$) OPD map obtained for each illumination angle was calculated by the PSI algorithm. The sample was a resolution target placed around $z = 5500\ \mu m$ from camera. The algorithm then finds the relative pixel shift distance δ of each of the six angled-illumination frames with respect to the central frame. This is done using the cross-correlation method. The total shift magnitude $\|\delta\|$ is calculated as a simple Euclidean norm $\|\delta\| = \sqrt{\delta_X^2 + \delta_Y^2}$. This is done for each color separately (δ_R for red ($\lambda = 656\ nm$), δ_G for green ($\lambda = 530\ nm$), δ_B for blue ($\lambda = 455\ nm$)) to provide the algorithm with non-averaged data. The resulting shifts are then averaged for each fiber core and used to calculate the final distance z of the features from the camera plane. The formula for the estimation of distance z (introduced in Eq. 4.3) is:

$$z = \kappa \cdot d_{pix} \cdot \|\delta\|_{RGB} \tag{5.1}$$

where $\kappa = 230$ is the experimentally verified proportionality constant (see Sec. 4.3.2) and $d_{pix} = 2.40\ \mu m$ is the pixel size of the camera sensor. All the results for both the shift finding methods can be found in Tab. 5.1 and Tab. 5.2.

Using the cross-correlation based unshifting algorithm proved to be a better solution to the problem. The first reason is that the algorithm is much faster, the second reason is that it also supports sub-pixel shifting precision, which is crucial for high precision of the estimation. Employing this algorithm, the distance of a focus plane can be found in a matter of seconds. The average value $5337 \pm 77\ \mu m$ returned by the algorithm with the use of cross-correlation method is in very good agreement with the estimated value of $5500\ \mu m$, which was found by visual refocusing. A

fiber core	$\|\delta_B\|$	$\|\delta_G\|$	$\|\delta_R\|$	average $\|\delta\|_{RGB}$	calculated z from $\|\delta\|$
core A	8.486 px	8.486 px	9.220 px	8.730 px	4819 μm
core B	9.220 px	9.220 px	9.900 px	9.447 px	5214 μm
core C	9.220 px	9.220 px	9.220 px	9.220 px	5089 μm
core D	9.220 px	9.220 px	9.220 px	9.220 px	5089 μm
core E	9.220 px	9.220 px	9.487 px	9.309 px	5138 μm
core F	9.220 px	9.220 px	9.220 px	9.220 px	5089 μm

Table 5.1: Results for unshifting based on difference (pixel precision) for a test sample placed at $z \approx 5500$ μm. Average z distance for all the fibers is $z = 5073 \pm 123$ μm.

fiber core	$\|\delta_B\|$	$\|\delta_G\|$	$\|\delta_R\|$	average $\|\delta\|_{RGB}$	calculated z from $\|\delta\|$
core A	9.364 px	9.477 px	9.577 px	9.473 px	5229 μm
core B	9.462 px	9.575 px	9.646 px	9.561 px	5277 μm
core C	9.721 px	9.791 px	9.906 px	9.806 px	5413 μm
core D	9.566 px	9.644 px	9.731 px	9.647 px	5325 μm
core E	9.773 px	9.873 px	9.993 px	9.880 px	5454 μm
core F	9.595 px	9.626 px	9.713 px	9.645 px	5324 μm

Table 5.2: Results for unshifting based on cross-correlation (sub-pixel precision) for a test sample placed at $z \approx 5500$ μm. Average z distance for all the fibers is $z = 5337 \pm 77$ μm.

comparison of the results obtained by manual and automatic focus finding can be seen in Fig. 5.9.

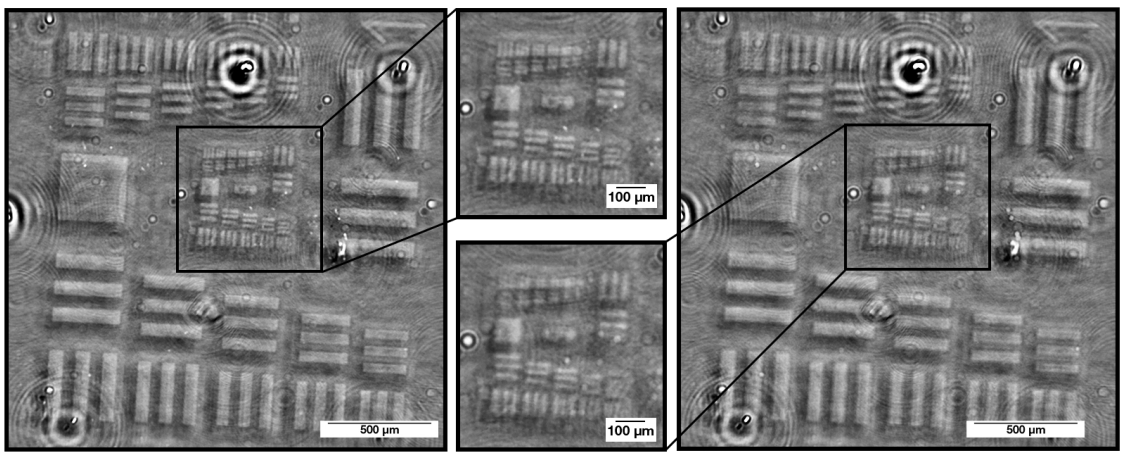

Figure 5.9: Comparison of manual focusing ($z_f = 5500$ μm, *left*) and focusing done by the uniform shift tracing method ($z_f = 5330$ μm, *right*), with zoom in on detailed features.

Focusing by eyes, which requires calculating a back-propagated image for many different planes of interest, is very often dependent on finding specific features (such as numbers made by lithography) to allow very precise focusing. In contrast, the uniform shift tracing method is very quick and doesn't require any special skills from the user. The downside of this method is a possible significant decrease in performance in case of samples with very pronounced sources of noise (such as big dust particles). Nevertheless, even in such cases, thanks to the ease of use and fast processing, the algorithm can easily be used in conjunction with the user, quickly offering a first estimation for the focus distance, which can be then easily verified or fine-tuned by the user.

5.3.2 Pixel-by-pixel (PbP) verification method

Based on the assumptions stated in Section 5.3, it can be expected that each object in the central image has its counterpart in each of the other six angled illumination images. The separation between these projection is then equal and proportional to the physical distance between feature-camera. This creates a regular hexagon of projections over all the angled illumination measurements (Fig. 5.10).

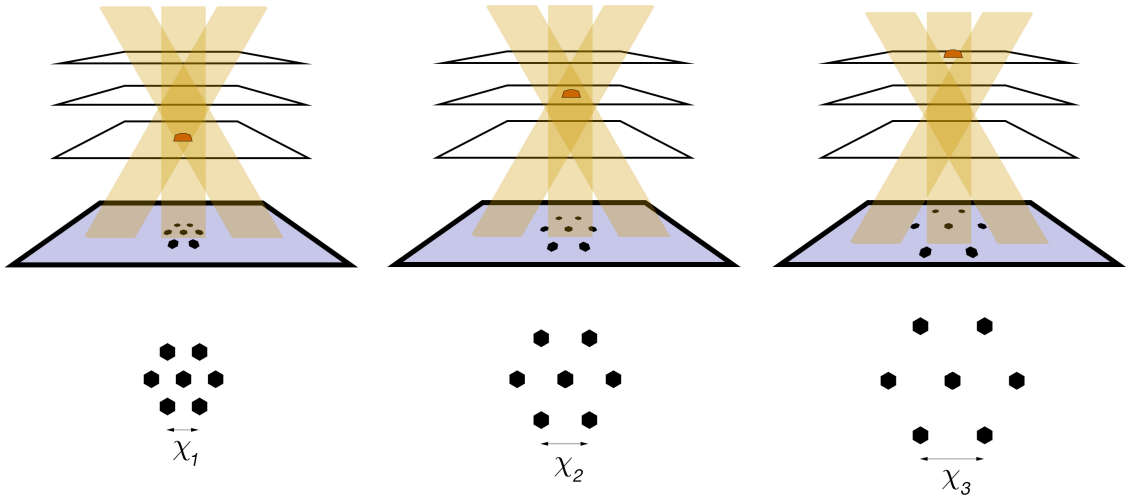

Figure 5.10: Schematic depiction of the hexagonal projections of single feature when using angled illumination. Thanks to the principles of geometrical optics, the further an object is from the camera, the larger hexagon (with size χ_n) will be created.

If, for a given pixel representing part of a feature, we are capable of find six matching pixels in the six angled-illumination captures, we can propose that the feature is in specific distance from the camera. By scanning all the images on a *pixel-by-pixel* basis, reading specific pixel values (lookup) and comparing the pixels in specific positions (verification), it is possible to recover the sample depth information on per-pixel basis. This method is called *pixel-by-pixel verification method* **(PbP)**.

To realize this approach, the knowledge of shift directions for each of the 6 angled illumination frames is required. This can be both known *a priori* (since it remains constant for a given setup) or estimated from the currently measured frames. To highlight the robustness of the method, the shift directions were always calculated directly from the data, without prior knowledge.

Step 1: Pixel set lookup

In the first *(lookup)* step, six relative pixel positions $(\Delta X_i, \Delta Y_i)$ from the central pixel $p_0(X, Y)$ are calculated based on the shift directions and expected displacement χ_n. All the seven images are then scanned on pixel-by-pixel basis. For every central pixel $p_0(X, Y)$, one pixel value $p_i(X + \Delta X_i, Y + \Delta Y_i)$ is returned from each of the angled illumination images. In total, for seven used fiber cores, this step returns seven pixel values p.

Step 2: Pixel set verification

In the second *(verification)* step, specific conditions have to be met for the set of values p in order to accept or reject the pixels as matching through all the frames. There is multitude of possible approaches:

i) **thresholding**: all the seven pixels have to have higher value than a threshold: $p_i > T \ \forall p_i \in p$,

ii) **distance from reference**: all the pixels from angled cores have to be close to the reference pixel: $|p_i - p_0| < T \ \forall p_{i \neq 0} \in p$,

iii) **total variance thresholding**: the total variance of given set p has to be below given threshold T: $\sigma^2(p) < T$,

iv) **distance variance thresholding**: variance of distances from reference p_0 for all angled cores has to be below a threshold T: $\sigma^2(|p - p_0|) < T$,

v) **feature descriptor distance**: using feature descriptors such as BRIEF [73], the similarity between central pixel and all the neighbors can be assessed and accepted the pixels are similar enough. Since BRIEF is a binary descriptor, the common approach uses Hamming distance d_H between descriptors $B_i = BRIEF(p_i)$ to assess the similarity: $d_H(B_i, B_0) < T \ \forall B_{i \neq 0}$. This approach requires extraction of pixels with it's neighborhood, is extremely computationally demanding and doesn't provide significantly better recognition in comparison to the simple approaches above.

When the pixel is accepted by comparing with selected conditions, the position is written into a binary map of matches with size equal to the original picture. This binary map can be then used as a mask on the OPD maps. This whole process is then repeated with varying pixel positions to reconstruct objects in different distances from the camera.

Results

To verify the **PbP** method, two layers of 10 nm thick silica dots ($\varnothing = 200\ \mu m$) were measured. The first layer focus plane was at $z_{f1} = 7000\ \mu m$, while the second layer was focused at $z_{f2} = 11000\ \mu m$. First, the shift directions from the center were found in $z_{f1} = 7000\ \mu m$ for each angled illumination frame and saved. Following this registration step, all the angled illumination frames in z_{f1} and z_{f2} were scanned on pixel-by-pixel basis, distances χ. The pixel sets p in each case were verified against a set of conditions: **(i)** *thresholding* of values $p_i > 1\ (nm)\ \forall\ p_i \in p$ and **(ii)** and *distance from reference* $|p_i - p_0| < \frac{p_0}{4}\ \forall\ p_{i\neq 0} \in p$. Using these conditions, binary map of accepted pixels was created for both z_{f1} and z_{f2}. The complete results are shown on Fig. 5.11.

5.3.3 Backpropagated pixel-by-pixel (β-PbP) verification method

Based on the approach previously highlighted in Sections 5.2 and 5.3.2, both the backpropagation and the pixel-by-pixel verification approaches were combined to devise a new, hybrid depth resolving method that fully utilizes all the data available from measuring with the multicore fiber bundle. The technique is called *backpropagated pixel-by-pixel verification method* (**β-PbP**) and is schematically depicted in Fig. 5.12.

The **β-PbP** method takes the full multi-angled illumination dataset (7 measurements, each done with different illumination angle). These measurements, after being processing with the PSI method (Sec. 3.2), produce complex electric fields in the camera plane $z = 0\ \mu m$. Those serve as an input to the function, together with a depth range to be investigated.

Step 1: Backpropagation

In the first step, these electric fields were backpropagated to n evenly distributed focus planes covering the full inspected volume of the sample. This process results in seven stacks of images (one for each fiber) focused in all z_n distances. As mentioned in the introduction to Section 5.3, an object that is in specific distance z_n from the camera will project as a hexagon of unique size across the six angled-illumination frames (Fig. 5.10). Based on the non-diverging propagation behavior of collimated beams, it can be assumed that the hexagon will linearly increase in size for features separated further from the camera (as depicted on Fig 5.10). At the same time, any object existing in a distance z_n from camera will be in focus only in the frame back-propagated to the $\pm z_n$ distance.

Thanks to this behavior of the system, a linear relation can be made between the back-propagation distance z_n and the hexagonal projection size χ_n. As was already

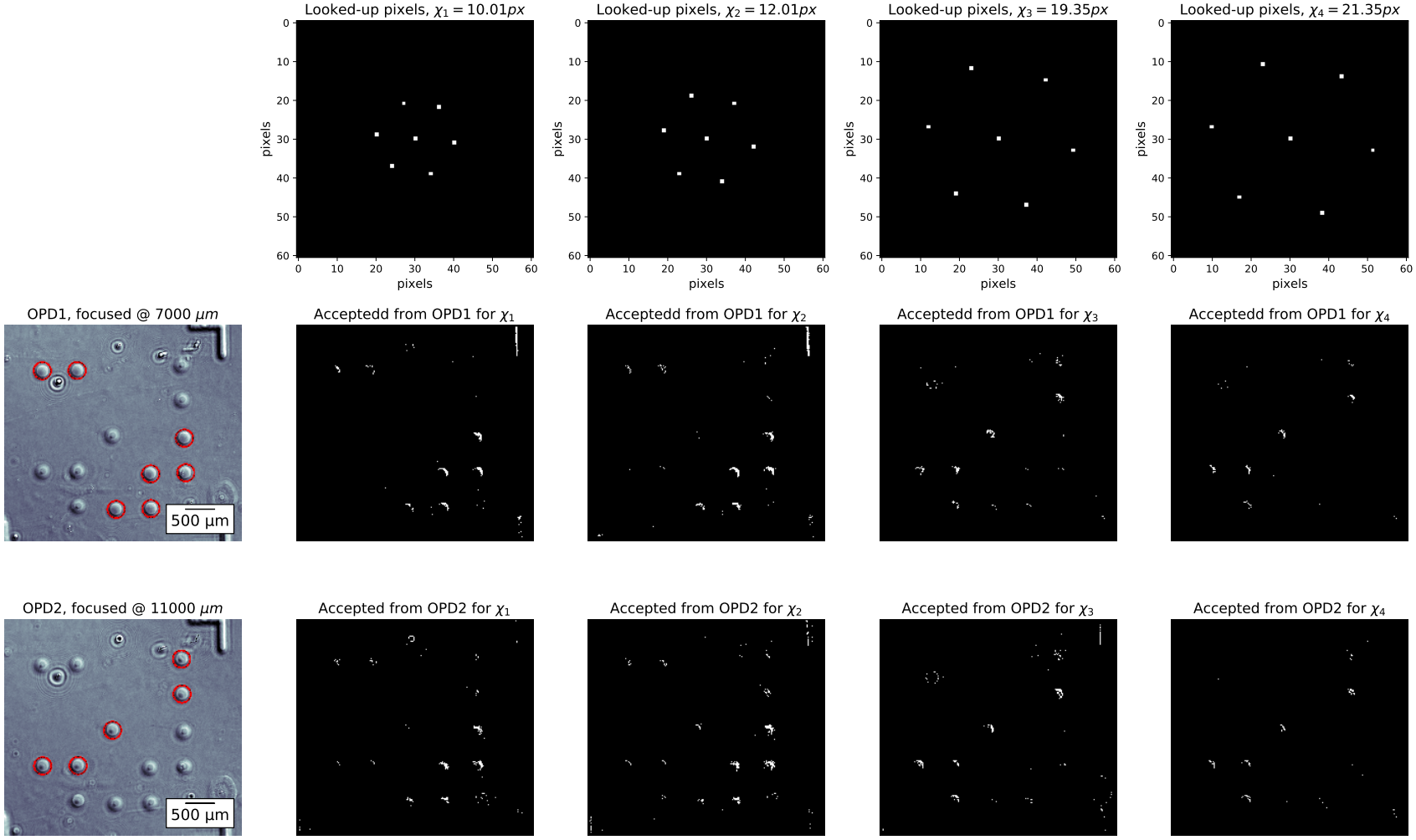

Figure 5.11: Results of the **PbP** shift verification method used on two stacked arrays of $\varnothing = 200\ \mu m$ silica dots. The first row shows how the pixel lookup positions gradually increase. Each row shows pixels that were found in the positions specified by the hexagon and accepted using given conditions. In ideal case, the maps showing accepted pixels should show only the features highlighted with red circles in one of the OPD maps.

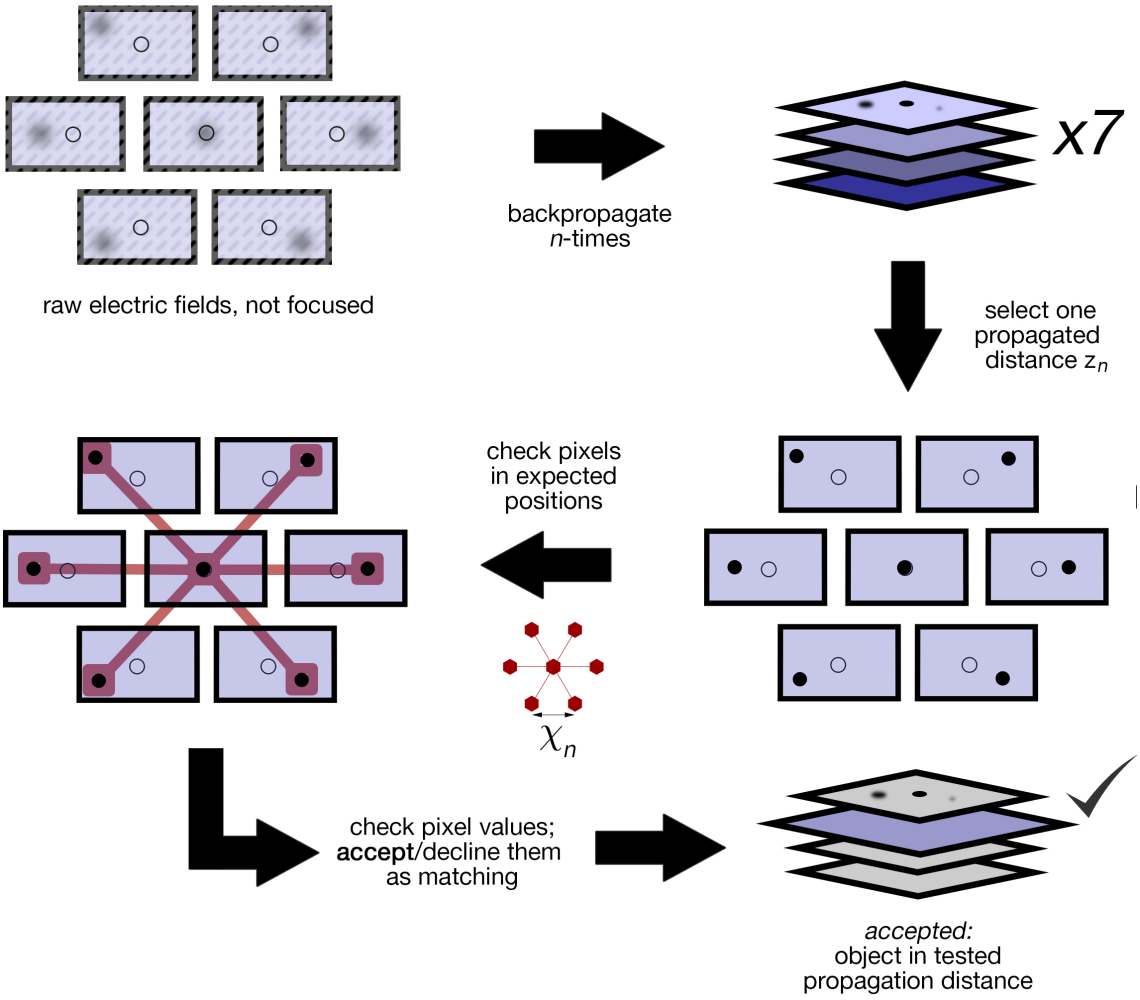

Figure 5.12: Data processing schematic of the backpropagated pixel-by-pixel verification method.

mentioned, the ratio between $\frac{z_n}{\chi_n}$ remains constant for given setup and can be assessed by measuring known sample or by calculation (Eq. 4.3). Then, for each propagation distance z_n, only one unique χ_n needs to be tested. The orientation of the hexagon is always the same (for given setup) and can be estimated from the images or known *a priori*. To demonstrate the robustness of the method, the shift directions were always calculated in the first step of the process. It is also worth mentioning that this methods is enabled by implementation of the backpropagation algorithm that undoes the effects of diffraction while it does not displace the object, even when illuminated with beam non-perpendicular to the sensor plane.

After the propagation, the algorithm loops through all the z_n distances in the stack. For each propagation distance z_n, all seven images are taken from the stack and unique χ_n is calculated. All the images are then pre-processed using threshold-based masking approach to segment the features from the background. Two masking formulas were created for this method.

Step 2: Feature segmentation by thresholding

The first formula (called *LogMask*) simply takes all positive pixel values (equal to positive OPD measured in the pixel area), applies natural logarithm to pronounce lower values and then shows only pixels above given threshold T.

$$p_{mask}(X,Y) = \begin{cases} 1 & \text{if } p > 0 \wedge \ln(p+c) > T \\ 0 & \text{else} \end{cases} \tag{5.2}$$

where ln is the natural logarithm (with base of e) and $c = 0.1$ and $T = 0.4$ are shifting constant and thresholding coefficient that were derived empirically.

The second formula (called *LogMaskAbs*) is very similar to the first one, except for returning values also for negative pixels (negative OPD) by using the absolute value. In a same fashion, it also applies natural logarithm to pronounce low values. This approach is better suited for the LIM, where every feature has the form of (overlaying) real and twin image. By taking the negative values into account, some information about the feature position can be additionaly extracted also from the twin image.

The *LogMaskAbs* algorithm then creates a binary mask using following criteria for each pixel $p(X,Y)$

$$p_{mask}(X,Y) = \begin{cases} 1 & \text{if } \ln(|p|+c) > T \\ 0 & \text{else} \end{cases} \tag{5.3}$$

where ln is the natural logarithm (with base of e) and $c = 0.1$ and $T = 0.4$ are shifting constant and thresholding coefficient that were derived empirically.

Step 3: Improved pixel set lookup and verification

After processing the data with masking, the algorithm then searches on *pixel-by-pixel* basis through the images, extracting the pixel values in expected positions (same as in **PbP** method, Sec. 5.3.2). Since this approach is inherently limited by the pixel grid, the algorithm uses the distance between opposite points of the hexagon instead of comparing each point only with the center. This effectively doubles the measured distance, which increases the precision. Each of these extracted pixel sets p is then verified using some of the criteria introduced in Sec. 5.3.2. Since the images are prone to noise, the lowest of the six values $p_{i\neq 0}$ is removed prior to the calculations to make the conditions less restrictive. Then, same as in the previous case, when a pixel in reference frame is crosschecked against all of its five counterparts and accepted, it is written in a binary map.

Step 4: Binary map denoising and refilling

To highlight the features and suppress the noise, each completed binary map is treated with custom-designed *noise-reducing* and f*eature-refilling* algorithms. In the first (denoising) step, the image is scanned with a 5×5 px sliding window. If less than $T_{noise} = 13$ pixels in the sliding window contain a binary 1, the central pixel is set to 0. This reduces the amount of lone (noise) pixels. In the second (refilling) step, the denoised image is scanned with 9×9 px sliding window. Every time the sliding window area contains at least $T_{fill} = 9$ pixels with binary 1, the central pixel is set to 1 too. Using this approach, this step refills the areas where pixels are already present. Both of the threshold values T_{noise} and T_{fill} for denoising and refilling were selected empirically based on their performance. The final binary maps contain information about the objects in each analyzed focus distance and can be used further, for example for volume visualizations.

Results

In first experimental verification of the β-**PbP** method, two layers of 10 nm thick silica dots ($\varnothing = 200\ \mu m$) were measured. First layer focus plane was at $z_{f1} = 7000\ \mu m$, while second layer was focused at $z_{f2} = 11000\ \mu m$. First, the shift directions for each OPD frame and for opposite frame pairs were estimated from the data and normalized to obtain shift directions (Fig 5.13). The algorithm was set to scan through distances $z = [3000\ \mu m, 15000\ \mu m]$ with increments of 2000 μm. The preprocessing masking filter *LogMaskAbs* was used with $c = 0.1$ and $T = 0.4$. The original OPD map was then multiplied with the the calculated mask to segment the features while keeping their profile information. The relation between hexagon size (=shift) χ_n for given plane z_n is in accordance with Eq. 4.3:

$$\chi_n = \frac{z_n}{\kappa \cdot d_{pix}} \tag{5.4}$$

where $\kappa = 230$ is the proportionality constant and $d_{pix} = 2.40\ \mu m$ is pixel size of the camera sensor. The acceptance conditions for the inspected set of pixels p were: **(i)** *thresholding* of values $p_i > 1\ (nm)\ \forall\ p_i \in p$ and **(ii)** and *distance from reference* $|p_i - p_0| < \frac{p_0}{5}\ \forall\ p_{i \neq 0} \in p$. Using these conditions, binary map of accepted pixels was created for each z_n and processed with denoising and refilling algorithm. The complete results are shown on Fig. 5.14. The same approach (with same parameters) was also applied on second sample, consisting of similar dot pattern with ($\varnothing = 50\ \mu m$). The results from this sample can be seen on Fig. 5.15. In both the figures, the OPD map was propagated to multiple z distances (first row) with features in two focus planes ($z_{f1} = 7000\ \mu m$ and $z_{f2} = 11000\ \mu m$). The thresholding filter effect can be seen on the second row. Following that, the thresholded maps were scanned across all the frames and thee binary maps (third row) show pixels

accepted by checking across the frames. The last row shows the effect of denoising and refilling algorithms.

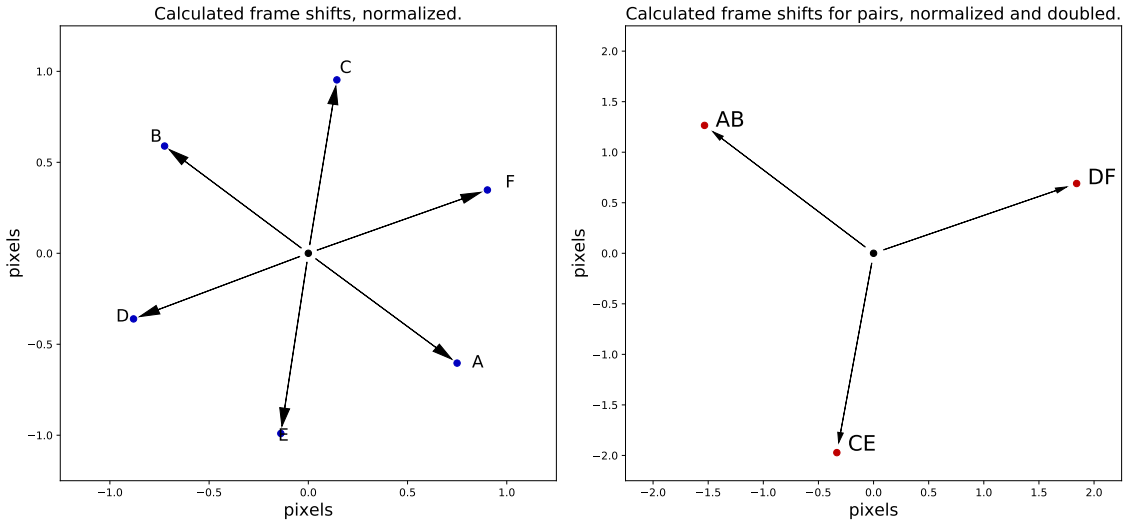

Figure 5.13: Visualization of the detected shift directions between the angled illumination frames (normalized, *left*) and between the opposite frames (normalized and doubled to preserve scale against the first set of shift, *right*).

5.4 Discussion

In the introduction part of this chapter, a summary of methods for three-dimensional imaging in LFM was provided. Unfortunately, most of these approaches can not be used with the LIM. The main limitation present in the LIM is the maximal beam angle available for multi-angle illumination. To obtain a full information about the sample in the LFM, a range of up to ±50° illumination angle is usually used [28]. However, this is not possible in the LIM, mainly due to the use of Savart plates.

Taking these limits into account, multiple methods were proposed for object depth resolving (Tab. 5.3). These approaches were realized using both single core fiber

	Single illumination angle	Multiple illumination angles
resolving single depth in one FoV	*Holographic autofocusing*	*Uniform shift tracing*
resolving multiple depths in one FoV	M×N *sliding window autofocusing*	*Pixel-by-pixel verification* (PbP) *Backpropagated pixel-by-pixel verification* (β-PbP)

Table 5.3: Table of developed depth-resolving methods.

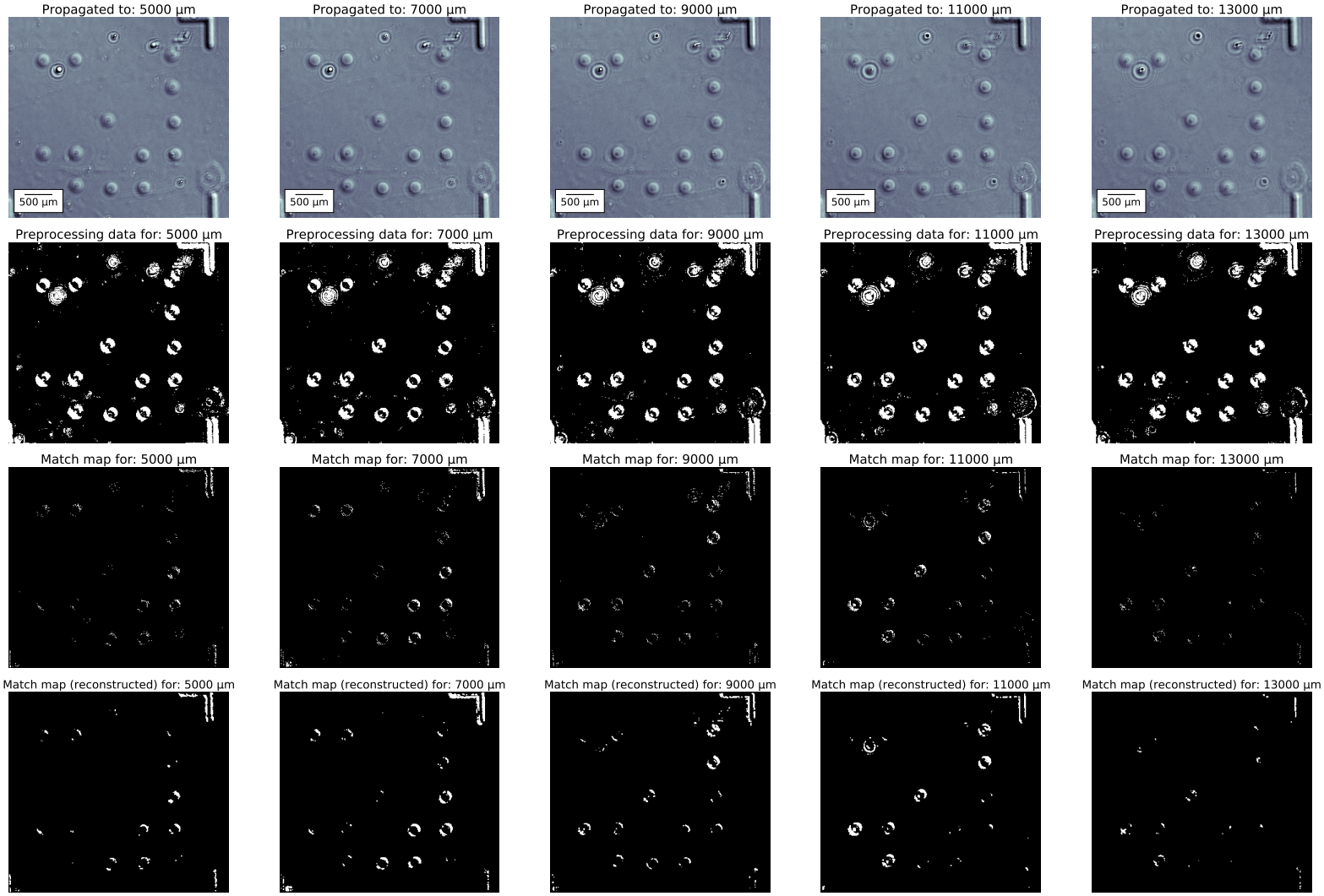

Figure 5.14: The **β-PbP** verification approach on $\varnothing = 200\ \mu m$ silica dots showing propagated OPD maps (first row) with thresholding (second row), accepted pixels (third row) and reconstruction (fourth row).

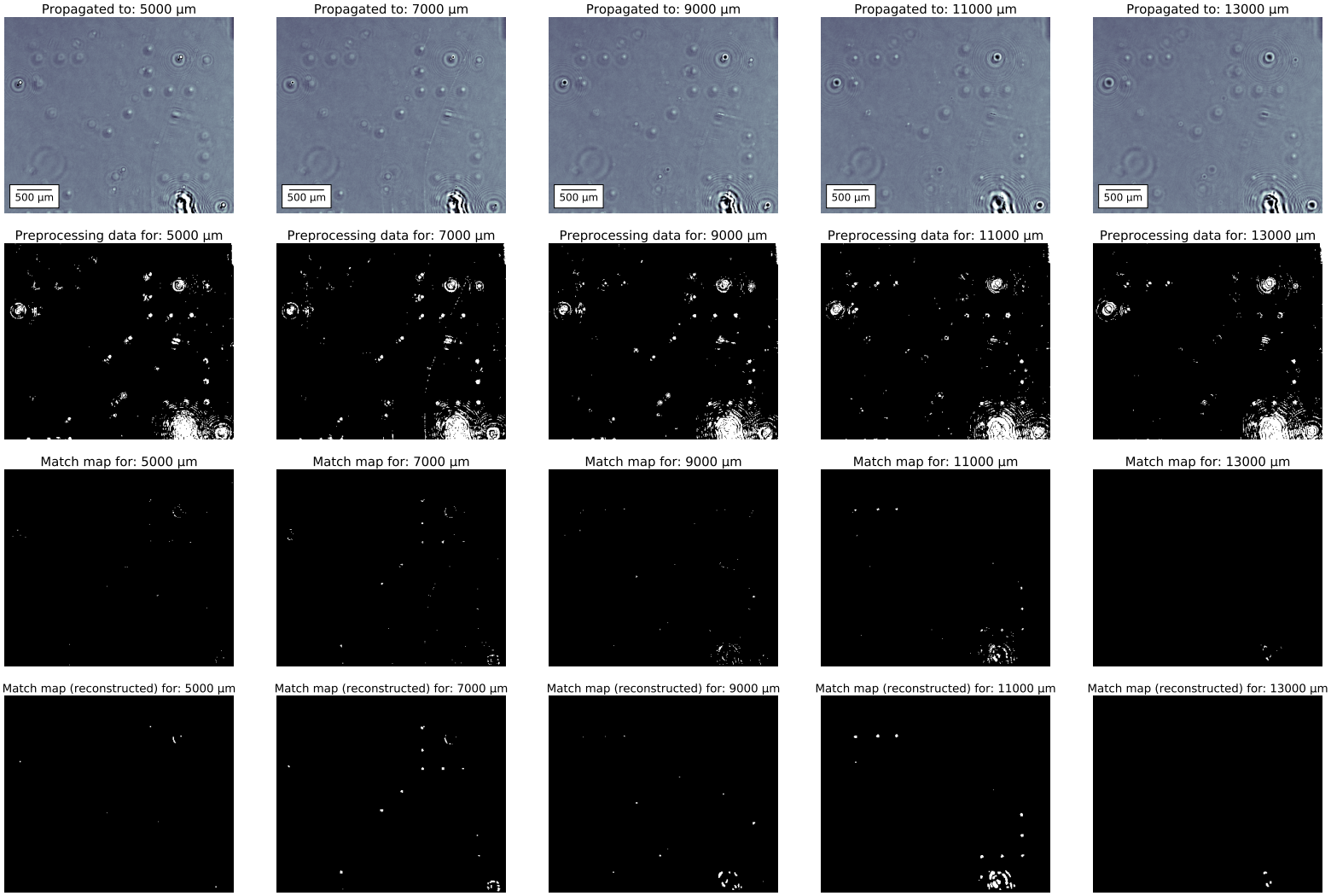

Figure 5.15: The β-**PbP** verification approach on $\varnothing = 50\ \mu m$ silica dots showing propagated OPD maps (first row) with thresholding (second row), accepted pixels (third row) and reconstruction (fourth row)

and multicore fiber bundle. The advantage of using one single core fiber is in greatly increased measurement speed (seven times faster in comparison to the full multicore bundle measurement) and significantly lower computation time. Single illumination depth resolving uses **(i)** the information from reconstructed OPD maps propagated into multiple z-planes, **(ii)** scanning the images with a sliding window and **(iii)** quick autofocusing or each of the $M \times N$ sliding windows positions. It was found that the robust autofocusing introduced in Sec. 4.4 didn't perform very well on small areas while also being computationally intensive. For this reason, less robust approaches were used in conjunction with the $M \times N$ scanning method. While the *thresholded pixel counter* approach (Fig. 4.17) offered good performance, prior assumptions about the sample were needed for it to function properly. For this reason, a new approach using Sobel edge-pronouncing filter was developed. This method didn't require assumptions about the sample character (such as expected feature height h) and returned very good results for simulated samples and feasible results for real dot arrays. With further tunning of the quick autofocusing approach and use of multi-scaled sliding windows, this technique shows potential as a very quick focus estimation method. Since it is bound to the rectangular sliding window, it will always provide more rough feature focusing, without respect to the actual feature shape. This behavior can be improved by the use of multiple sizes of the sliding windows (Fig. 5.6), the "pixelation" is however still apparent. Alternative approach to replace the sliding window could be to use statistical methods for segmentation of the image to isolate the regions where objects of interest (e.g. micro-organisms) reside [51]. However, it is important to keep in mind that holography is generally not an ideal three-dimensional imaging method because it can suffer from spatial artifacts due to absorption and/or phase aberrations within the volume of a sample. As noted by Zhang et al. [30], different layers of the sample should experience the same illumination wavefront that is only phase-shifted due to wave propagation inside the sample volume. In other words, if there's a region of the sample with overlaying modulation of the refractive index, all the bottom layers will experience modified illumination wavefront with different phase and amplitude.

The multicore fiber bundle (coupled to reflective collimator) was first used to estimate the focus plane of a whole frame, offering an alternative to autofocusing algorithms. While the image acquisition process requires more time, the estimation of the focus plane is very quick thanks to optimized unshifting algorithms. By experimentally finding the proportionality constant κ, subsequent sample depth estimations can be done with high speed and accuracy. This approach (finding shifts) was also tested in conjunction with the $M \times N$ scanning (frame shift lookup for each sliding windows position), but the performance was below acceptable. The most probable explanation for the sub-standard performance of this approach is the need for the shift estimation algorithm to operate on larger image areas with enough significant features to properly calculate the shift. These was not provided with the sliding window, where only fractional image areas were provided.

The main depth resolving methods in this chapter were the two pixel-by-pixel scanning methods. First, the concept of *pixel-by-pixel verification method* **(PbP)** proved

that combining information from all the angled illumination frames in a specific way has a potential for estimating the depth of an object. Unfortunately, this method was inherently limited by the need of providing it with in-focus frames. While the pixel lookup mechanism works to a certain extent even for non-focused images (hypothetically allowing depth estimation using unfocused images at $z = 0\ \mu m$), the out-of-focus features are both smeared over larger area than the actual feature size and have decreased profile height, which is crucial for the approach to successfully separate features from noise.

The solution to these limitations was offered with the *backpropagated pixel-by-pixel verification* β-**PbP** method, which utilizes a single focus plane associated to each expected feature shifting distance χ. This combined method presents multiple improvements over the previous one:

i) it has increased shifting sensitivity by looking up for opposite pixels of the hexagon on pairwise basis,

ii) it is significantly faster thanks to the rewritten pixel lookup algorithm (using single unshifting per frame for each lookup distance, instead of computationally intensive array-array multiplication),

iii) it is self-sustained, with all the data processing done automatically in one go, including propagating all the fields and averaging the colors for higher signal-to-noise ratio.

As can be seen in Fig. 5.14 and Fig. 5.15, the algorithm performed better on smaller sized features. There are two explanations for this behavior:

i) large, flat features don't offer enough signature pixels for precise resolving. Thanks to this, such features get spread over higher z distance.

ii) The differential nature of the LIM means that basically for features larger than the shear distance s, only some edges are visible. By this account, the LIM generally performs better while measuring objects smaller than s.

One of the advantages of both the **PbP** and β-**PbP** methods is that they do not rely heavily on the accuracy of the unshifting algorithm, which is always subject to limited precision. The methods only require detection of shift directions, but later use normalized direction vector and rescaling, depending on the investigated propagation distance. The second advantage is that both these approaches enable the use of kernels (small matrices) when scanning through the images. Acquiring the information from all the frames using for example 5×5 px kernel instead of just a single pixel value might offer more data (from neighboring pixels) to properly verify that the inspected pixel (or image section) belongs to the same object. The downside of such an approach would be again an increased computational difficulty and the need to develop new pixel acceptance criteria that would properly handle the returned set of 2D arrays. Nevertheless, this alternative scanning method is something that should be examined in future research.

However, all of the methods developed in this chapter have one inherent limitation. Since they always compare pixel values amongst the frames, they essentially scan the maps and look for notable features. In this manner, they are basically limited in a fashion similar to the human eye. If a set of overlaid features is presented to the algorithm, these methods will most likely not be able to correctly resolve it. This is the same for people as our brain is not capable to distinguish which feature is in which distance by seeing their overlaid projection. If any two (or more) features are overlaying and are separated by very low distance (such that the angled illumination will not separate their projections), they will not be accurately resolved with the algorithms. More sophisticated implementation of the pixel verification criteria may pave the way towards improved resolving of overlaid features, however, the general scope of multi-angled illumination for depth resolving of these features seems to be limited. One of the possible ways to enable proper depth resolving and tomography of overlaying features might be in utilizing methods such as iterative multislice approach [69]. There, the volume distribution of sample features is acquired by iteratively propagating a light field through a set of estimated $z-$planes and modifying the estimations of the layers to match the real image readout after propagating through the stack. A second viable way of acquiring the depth information could be in use of state-of-the-art machine learning approaches [61]. Machine learning could also alleviate the need of numerical refocusing, which is very demanding in respect to the computational resources, mainly for large (multiple megapixel) arrays.

Since the range of illumination angles available in the LIM is restricted by design of the device ($\theta < 5°$), true tomographic imaging is a challenging goal. One of the solutions to this limitation could be by introduction of a special, sample moving mechanism that would tilt or rotate the sample while the illumination would be kept in the same place. Although the use of mechanical components always brings more demand on alignment and movement precision, this solution has a potential to solve the scanning angle limitation.

6 Conclusions

Microscopy techniques that allow three-dimensional imaging are of high importance in both laboratory research and industrial applications. This Master thesis introduced means of enabling quantitative phase imaging in different sample sections with the lensfree interferometric microscope (LIM) by using angled, partially-coherent collimated beams. The information obtained in measurements with multiple beam angles was utilized for:

i) **improved single-plane quantitative phase imaging** (Chapter 4), where the multi-angle dataset was processed with a sequence of algorithms (including interpolated upsampling, frame shift registration and averaging) with the aim of increasing resolution;

ii) **phase-object depth resolving**(Chapter 5), where multiple self-developed methods were implemented, using both the full holographic information, the angled beams and their combination.

All of the proposed methods were implemented in the Python programming language. The improved single-plane imaging method was tested with a custom-made USAF1951 resolution target consisting of silica structures. When compared to non-processed measurements, the resulting phase maps had increased spatial resolution of $\sim 10\ \mu m$, axial resolution of $\sim 0.5\ nm$, improved signal-to-noise ratio and suppressed holographic twin images. The depth-resolving methods were tested by measuring a sample consisting of two layers of 10 nm thick silica dots of different diameter. The performance of each method was evaluated and compared, with advantages, drawbacks and comparison provided. While the $M \times N$ *sliding window autofocusing* method proved to be a very quick and potentially viable solution to object depth estimation, it is inherently limited by the square shape of the sliding window. Also, it doesn't utilize the extra information encoded in measurements from angled beams. The most promising depth-resolving performance was delivered by the *backpropagated pixel-by-pixel verification method* (β-**PbP**) that calculates the depth for each image pixel over the whole field-of-view. By combining the two dimensional maps of sample-induced phase shifts with information of object depth obtained by the depth-resolving methods, three-dimensional sections of refractive index distribution were reconstructed for samples with volume of $V \approx 0.5\ cm^3$ and depth sensitivity below 1 nm. It was also observed that smaller features were more suitable for analysis using this method.

To optimize the microscope performance in depth-resolving, the effect of various setup parameters (such as operating distances between the elements, camera model, optical fiber properties) on image quality was evaluated. Simultaneously, the hardware controllers enabling the measurements (such as camera drivers and actuator

drivers) were implemented in the Python-based controlling software to enable cross-platform measurement automation. Complete acquisition controls and subsequent data processing were realized using a Linux-running single-board computer.

Combining the developed imaging methods, the setup optimizations and the all-in-one device automation enables the LIM to be used in both point-of-care imaging or continuous production line monitoring. This opens the door towards new applications of the device, such as optical data storage reading, 3D localization of transparent structures or verification of holographic security elements. Systems utilizing information encoded in glass are nowadays of significant interest for long-term, cold data storage. On the other hand, localization of transparent structural elements (such as micro-sized defects) is essential for quality control, for example in smartphone display manufacturing.

The results of this thesis are very promising for the above mentioned real world applications. Nevertheless, further investigation and work is needed to realize the full potential of these techniques. The proposed algorithms need to be tested with different kinds of transparent samples to assess the overall performance, and also further optimized in accordance with the results of these tests. The ability of these approaches to properly handle overlaying structures in the sample also needs to be evaluated. An appropriate, automated approach to acquire images using the multicore fiber bundle needs to be implemented, to make the measurements less laborious. There are also different techniques (such as iterative multislice reconstruction or Fourier ptychography) that are promising for the 3D LIM imaging and should be evaluated. To reduce the post-processing time, parallelization or use of GPU clusters could offer significant improvements. Last but not least, machine learning algorithms show a great potential for use in microscopy techniques, and as such should also be tested for data processing of the LIM measurements.

References

1. CROFT, William J. *Under the Microscope: A Brief History of Microscopy*. 1st Ed. WSPC, 2006. Series in Popular Science. ISBN 9789814338042.
2. MIR, M.; BHADURI, B.; WANG, R.; ZHU, R.; POPESCU, G. Quantitative Phase Imaging. In: *Progress in Optics*. Elsevier, 2012, pp. 133–217. Available from DOI: 10.1016/b978-0-44-459422-8.00003-5.
3. NIKNEJAD, Ali M. *mm-Wave Silicon Technology: 60 GHz and Beyond*. 1st Ed. Springer US, 2008. ISBN 9780387765617.
4. KIM, M. K. *Digital Holographic Microscopy: Principles, Techniques, and Applications*. 1st Ed. Springer-Verlag GmbH, 2011. ISBN 1441977929.
5. WU, Y.; OZCAN, A. Lensless digital holographic microscopy and its applications in biomedicine and environmental monitoring. *Methods*. 2018, vol. 136, pp. 4–16. Available from DOI: 10.1016/j.ymeth.2017.08.013.
6. VOELZ, D. G. *Computational Fourier Optics: A MATLAB Tutorial (SPIE Tutorial Texts Vol. TT89)*. 1st Ed. SPIE Press, 2011. ISBN 978-0-8194-8204-4.
7. CAULFIELD, H. J. *Handbook of Optical Holography*. 1st Ed. Academic Press, 1980. ISBN 978-0-12-165350-7.
8. GOODMAN, J. W. *Introduction to Fourier Optics*. 3rd Ed. W.H.Freeman & Co Ltd, 2004. ISBN 0974707724.
9. GABOR, D. Holography, 1948-1971. *Science*. 1972, vol. 177, no. 4046, pp. 299–313. Available from DOI: 10.1126/science.177.4046.299.
10. HARIHARAN, P. *Basics of Holography*. 1st Ed. Cambridge University Press, 2002. ISBN 9780521002004.
11. YAROSLAVSKY, L. *Introduction to Digital Holography*. 1st Ed. Bentham Science Publishers, 2009.
12. CUCHE, E.; BEVILACQUA, F.; DEPEURSINGE, Ch. Digital holography for quantitative phase-contrast imaging. *Optics Letters*. 1999, vol. 24, no. 5, pp. 291. Available from DOI: 10.1364/ol.24.000291.
13. KEMPER, B.; BAUWENS, A.; VOLLMER, A.; KETELHUT, S.; LANGEHANENBERG, P.; MÜTHING, J.; KARCH, H.; BALLY, G. von. Label-free quantitative cell division monitoring of endothelial cells by digital holographic microscopy. *Journal of Biomedical Optics*. 2010, vol. 15, no. 3, pp. 036009. Available from DOI: 10.1117/1.3431712.
14. LUO, W.; ZHANG, Y.; FEIZI, A.; GÖRÖCS, Z.; OZCAN, A. Pixel superresolution using wavelength scanning. *Light: Science & Applications*. 2015, vol. 5, no. 4, pp. e16060–e16060. Available from DOI: 10.1038/lsa.2016.60.

15. CHEN, G.L.; LIN, C.Y.; KUO, M.K.; CHANG, C.C. Numerical reconstruction and twin-image suppression using an off-axis Fresnel digital hologram. *Applied Physics B*. 2008, vol. 90, no. 3-4, pp. 527–532. Available from DOI: 10.1007/s00340-007-2910-5.

16. STOYKOVA, E.; KANG, H.; PARK, J. Twin-image problem in digital holography—a survey (Invited Paper). *Chinese Optics Letters*. 2014, vol. 12, no. 6, pp. 060013–60024. Available from DOI: 10.3788/col201412.060013.

17. KOREN, G.; POLACK, F.; JOYEUX, D. Iterative algorithms for twin-image elimination in in-line holography using finite-support constraints. *Journal of the Optical Society of America A*. 1993, vol. 10, no. 3, pp. 423. Available from DOI: 10.1364/josaa.10.000423.

18. LATYCHEVSKAIA, T.; FINK, H.-W. Solution to the Twin Image Problem in Holography. *Physical Review Letters*. 2007, vol. 98, no. 23. Available from DOI: 10.1103/physrevlett.98.233901.

19. DENIS, L.; FOURNIER, C.; FOURNEL, T.; DUCOTTET, C. Numerical suppression of the twin image in in-line holography of a volume of micro-objects. *Measurement Science and Technology*. 2008, vol. 19, no. 7, pp. 074004. Available from DOI: 10.1088/0957-0233/19/7/074004.

20. KLETTE, R. *Concise Computer Vision*. 1st Ed. Springer London, 2014. ISBN 9781447163206.

21. MCLEOD, E.; LUO, W.; MUDANYALI, O.; GREENBAUM, A.; OZCAN, A. Toward giga-pixel nanoscopy on a chip: a computational wide-field look at the nano-scale without the use of lenses. *Lab on a Chip*. 2013, vol. 13, no. 11, pp. 2028. Available from DOI: 10.1039/c3lc50222h.

22. DENG, Y.; CHU, D. Coherence properties of different light sources and their effect on the image sharpness and speckle of holographic displays. *Scientific Reports*. 2017, vol. 7, no. 1. Available from DOI: 10.1038/s41598-017-06215-x.

23. SU, T.-W.; ISIKMAN, S. O.; BISHARA, W.; TSENG, D.; ERLINGER, A.; OZCAN, A. Multi-angle lensless digital holography for depth resolved imaging on a chip. *Optics Express*. 2010, vol. 18, no. 9, pp. 9690. Available from DOI: 10.1364/oe.18.009690.

24. GREENBAUM, A.; LUO, W.; SU, T.-W.; GÖRÖCS, Z.; XUE, L.; ISIKMAN, S. O.; COSKUN, A. F.; MUDANYALI, O.; OZCAN, A. Imaging without lenses: achievements and remaining challenges of wide-field on-chip microscopy. *Nature Methods*. 2012, vol. 9, no. 9, pp. 889–895. Available from DOI: 10.1038/nmeth.2114.

25. SHIMOBABA, T.; TANIGUCHI, Y.; SHIRAKI, A.; MASUDA, N.; ITO, T. Portable and low-cost digital holographic microscopy using web camera, point light source LED and open-source libraries. In: *Biomedical Optics and 3-D Imaging*. OSA, 2012. Available from DOI: 10.1364/biomed.2012.jm3a.50.

26. BISHARA, W.; SIKORA, U.; MUDANYALI, O.; SU, T.-W.; YAGLIDERE, O.; LUCKHART, S.; OZCAN, A. Holographic pixel super-resolution in portable lensless on-chip microscopy using a fiber-optic array. *Lab on a Chip*. 2011, vol. 11, no. 7, pp. 1276. Available from DOI: 10.1039/c0lc00684j.

27. WANG, M.; FENG, S.; WU, J. Pixel super-resolution in digital in-line holography. In: SHENG, Yunlong; YU, Chongxiu; ZHOU, Changhe (eds.). *Holography, Diffractive Optics, and Applications VII*. SPIE, 2016. Available from DOI: 10.1117/12.2245969.

28. ISIKMAN, S. O.; BISHARA, W.; MAVANDADI, S.; YU, F. W.; FENG, S.; LAU, R.; OZCAN, A. Lens-free optical tomographic microscope with a large imaging volume on a chip. *Proceedings of the National Academy of Sciences*. 2011, vol. 108, no. 18, pp. 7296–7301. Available from DOI: 10.1073/pnas.1015638108.

29. MICÓ, V.; GRANERO, L.; ZALEVSKY, Z.; GARCÍA, J. Superresolved phase-shifting Gabor holography by CCD shift. *Journal of Optics A: Pure and Applied Optics*. 2009, vol. 11, no. 12, pp. 125408. Available from DOI: 10.1088/1464-4258/11/12/125408.

30. ZHANG, Y. et al. 3D imaging of optically cleared tissue using a simplified CLARITY method and on-chip microscopy. *Science Advances*. 2017, vol. 3, no. 8, pp. e1700553. Available from DOI: 10.1126/sciadv.1700553.

31. LAN, H.-C.; WU, M.-L.; YEATMAN, E. M. Non-mechanical sub-pixel image shifter for acquiring super-resolution digital images. *Optics Express*. 2009, vol. 17, no. 25, pp. 22992. Available from DOI: 10.1364/oe.17.022992.

32. BALCI, M.; FOROOSH, H. Estimating sub-pixel shifts directly from the phase difference. In: *IEEE International Conference on Image Processing 2005*. IEEE, 2005. Available from DOI: 10.1109/icip.2005.1529936.

33. VANDEWALLE, P.; SUSSTRUNK, S.; VETTERLI, M. A Frequency Domain Approach to Registration of Aliased Images with Application to Super-resolution. *EURASIP Journal on Advances in Signal Processing*. 2006, vol. 2006, no. 1. Available from DOI: 10.1155/asp/2006/71459.

34. SONG, J.; SWISHER, C. L.; IM, Hy.; JEONG, S.; PATHANIA, D.; IWAMOTO, Y.; PIVOVAROV, M.; WEISSLEDER, R.; LEE, H. Sparsity-Based Pixel Super Resolution for Lens-Free Digital In-line Holography. *Scientific Reports*. 2016, vol. 6, no. 1. Available from DOI: 10.1038/srep24681.

35. IRANI, M.; PELEG, S. Super resolution from image sequences. In: *[1990] Proceedings. 10th International Conference on Pattern Recognition*. IEEE Comput. Soc. Press, 1990. Available from DOI: 10.1109/icpr.1990.119340.

36. ELAD, M.; HEL-OR, Y. A fast super-resolution reconstruction algorithm for pure translational motion and common space-invariant blur. *IEEE Transactions on Image Processing*. 2001, vol. 10, no. 8, pp. 1187–1193. Available from DOI: 10.1109/83.935034.

37. CRISTÓBAL, G.; GIL, E.; ŠROUBEK, F.; FLUSSER, J.; MIRAVET, C.; RODRIGUEZ, F. B. Superresolution imaging: a survey of current techniques. In: LUK, Franklin T. (ed.). *Advanced Signal Processing Algorithms, Architectures, and Implementations XVIII*. SPIE, 2008. Available from DOI: 10.1117/12.797302.

38. NASROLLAHI, K.; ESCALERA, S.; RASTI, P.; ANBARJAFARI, G.; BARO, X.; ESCALANTE, H. J.; MOESLUND, T. B. Deep learning based super-resolution for improved action recognition. In: *2015 International Conference on Image Processing Theory, Tools and Applications (IPTA)*. IEEE, 2015. Available from DOI: 10.1109/ipta.2015.7367098.

39. OZCAN, A.; MCLEOD, E. Lensless Imaging and Sensing. *Annual Review of Biomedical Engineering*. 2016, vol. 18, no. 1, pp. 77–102. Available from DOI: 10.1146/annurev-bioeng-092515-010849.

40. SU, T.-W.; XUE, L.; OZCAN, A. High-throughput lensfree 3D tracking of human sperms reveals rare statistics of helical trajectories. *Proceedings of the National Academy of Sciences*. 2012, vol. 109, no. 40, pp. 16018–16022. Available from DOI: 10.1073/pnas.1212506109.

41. GREENBAUM, A.; ZHANG, Y.; FEIZI, A.; CHUNG, P.-L.; LUO, W.; KANDUKURI, S. R.; OZCAN, A. Wide-field computational imaging of pathology slides using lens-free on-chip microscopy. *Science Translational Medicine*. 2014, vol. 6, no. 267. Available from DOI: 10.1126/scitranslmed.3009850.

42. KESAVAN, S. Vinjimore et al. High-throughput monitoring of major cell functions by means of lensfree video microscopy. *Scientific Reports*. 2014, vol. 4, no. 1. Available from DOI: 10.1038/srep05942.

43. TERBORG, R. A. *Lens-Free Interferometric Microscope for Transparent Materials*. 2018. PhD thesis. Universitat Politècnica de Catalunya.

44. SIROHI, R. *Optical Methods of Measurement*. 1st Ed. CRC Press, 2018.

45. TRINH, H.; LIN, S.; CHEN, L.; YEH, S.; CHEN, C. Differential interference contrast microscopy using Savart plates. *Journal of Optics*. 2017, vol. 19, no. 4, pp. 045601. Available from DOI: 10.1088/2040-8986/aa5d62.

46. GREENBAUM, A.; OZCAN, A. Maskless imaging of dense samples using pixel super-resolution based multi-height lensfree on-chip microscopy. *Optics Express*. 2012, vol. 20, no. 3, pp. 3129. Available from DOI: 10.1364/oe.20.003129.

47. TERBORG, R. A.; PELLO, J.; MANNELLI, I.; TORRES, J. P.; PRUNERI, V. Ultrasensitive interferometric on-chip microscopy of transparent objects. *Science Advances*. 2016, vol. 2, no. 6, pp. e1600077. Available from DOI: 10.1126/sciadv.1600077.

48. KIM, J.-H.; YOON, S.-W.; LEE, J.-H.; AHN, W.-J.; PAHK, H.-J. New algorithm of white-light phase shifting interferometry pursing higher repeatability by using numerical phase error correction schemes of pre-processor, main processor, and post-processor. *Optics and Lasers in Engineering*. 2008, vol. 46, no. 2, pp. 140–148. Available from DOI: 10.1016/j.optlaseng.2007.08.008.

49. YESILKOY, F.; TERBORG, R. A; PELLO, J.; BELUSHKIN, A. A; JAHANI, Y.; PRUNERI, V.; ALTUG, H. Phase-sensitive plasmonic biosensor using a portable and large field-of-view interferometric microarray imager. *Light: Science & Applications*. 2017, vol. 7, no. 2, pp. 17152. Available from DOI: 10.1038/lsa.2017.152.

50. MALACARA, D.; SERVÍN, M.; MALACARA, Z. *Interferogram Analysis For Optical Testing*. 2nd Ed. CRC Press, 2005. ISBN 9781574446821.

51. MOON, I.; DANESHPANAH, M.; JAVIDI, B.; STERN, A. Automated Three-Dimensional Identification and Tracking of Micro/Nanobiological Organisms by Computational Holographic Microscopy. *Proceedings of the IEEE*. 2009, vol. 97, no. 6, pp. 990–1010. Available from DOI: 10.1109/jproc.2009.2017563.

52. SCHWIEGERLING, J. *Optical Specification, Fabrication, and Testing*. 1st. Ed. SPIE Press, 2014. ISBN 9781628413663.

53. JACKSON, J. D. *Classical Electrodynamics*. Wiley & Sons Inc., 1998. ISBN 978-0471309321.

54. LIU, J.-P. Controlling the aliasing by zero-padding in the digital calculation of the scalar diffraction. *Journal of the Optical Society of America A*. 2012, vol. 29, no. 9, pp. 1956. Available from DOI: 10.1364/josaa.29.001956.

55. TOYODA, T.; YABE, M. The temperature dependence of the refractive indices of fused silica and crystal quartz. *Journal of Physics D: Applied Physics*. 1983, vol. 16, no. 5, pp. L97–L100. Available from DOI: 10.1088/0022-3727/16/5/002.

56. IVANOV, V.; LEVICHEV, M.; NOZDRIN, Y.; NOVIKOV, M. Temperature dependence of electro-optic effect and natural linear birefringence in quartz measured by low-coherence interferometry. *Applied Optics*. 2015, vol. 54, no. 33, pp. 9911. Available from DOI: 10.1364/ao.54.009911.

57. HEJDA, Matěj. *PyIDSCam* [GitHub repository]. 2018. Available also from: https://github.com/mhejda/PyIDSCam.

58. ZHANG, Y.; WANG, H.; WU, Y.; TAMAMITSU, M.; OZCAN, A. Robust Holographic Autofocusing Based on Edge Sparsity. In: *Conference on Lasers and Electro-Optics*. OSA, 2018. Available from DOI: 10.1364/cleo_at.2018.am1j.7.

59. TAMAMITSU, M.; ZHANG, Y.; WANG, H.; WU, Y.; OZCAN, A. Comparison of Gini index and Tamura coefficient for holographic autofocusing based on the edge sparsity of the complex optical wavefront. 2017. Available from arXiv: http://arxiv.org/abs/1708.08055v1 [physics.optics].

60. MEMMOLO, P.; PATURZO, M.; JAVIDI, B.; NETTI, P. A.; FERRARO, P. Refocusing criterion via sparsity measurements in digital holography. *Optics Letters*. 2014, vol. 39, no. 16, pp. 4719. Available from DOI: 10.1364/ol.39.004719.

61. WU, Y.; RIVENSON, Y.; ZHANG, Y.; WEI, Z.; GÜNAYDIN, H.; LIN, X.; OZCAN, A. Extended depth-of-field in holographic imaging using deep-learning-based autofocusing and phase recovery. *Optica*. 2018, vol. 5, no. 6, pp. 704. Available from DOI: 10.1364/optica.5.000704.

62. DEVANEY, A. J. *Mathematical Foundations of Imaging, Tomography and Wavefield Inversion*. 1st Ed. Cambridge University Press, 2012. ISBN 978-0521119740.

63. ISIKMAN, S. O.; BISHARA, W.; SIKORA, U.; YAGLIDERE, O.; YEAH, J.; OZCAN, A. Field-portable lensfree tomographic microscope. *Lab on a Chip*. 2011, vol. 11, no. 13, pp. 2222. Available from DOI: 10.1039/c1lc20127a.

64. ISIKMAN, S. O.; GREENBAUM, A.; LUO, W.; COSKUN, A. F.; OZCAN, A. Giga-Pixel Lensfree Holographic Microscopy and Tomography Using Color Image Sensors. *PLoS ONE*. 2012, vol. 7, no. 9, pp. e45044. Available from DOI: 10.1371/journal.pone.0045044.

65. BISHARA, W.; ISIKMAN, S. O.; OZCAN, A. Lensfree Optofluidic Microscopy and Tomography. *Annals of Biomedical Engineering*. 2011, vol. 40, no. 2, pp. 251–262. Available from DOI: 10.1007/s10439-011-0385-3.

66. YU, L.; KIM, M. K. Wavelength-scanning digital interference holography for tomographic three-dimensional imaging by use of the angular spectrum method. *Optics Letters*. 2005, vol. 30, no. 16, pp. 2092. Available from DOI: 10.1364/ol.30.002092.

67. JAVIDI, B.; MOON, I.; YEOM, S.; CARAPEZZA, E. Three-dimensional imaging and recognition of microorganism using single-exposure on-line (SEOL) digital holography. *Optics Express*. 2005, vol. 13, no. 12, pp. 4492. Available from DOI: 10.1364/opex.13.004492.

68. MOON, I.; JAVIDI, B. 3-D Visualization and Identification of Biological Microorganisms Using Partially Temporal Incoherent Light In-Line Computational Holographic Imaging. *IEEE Transactions on Medical Imaging*. 2008, vol. 27, no. 12, pp. 1782–1790. Available from DOI: 10.1109/tmi.2008.927339.

69. TIAN, L.; WALLER, L. 3D intensity and phase imaging from light field measurements in an LED array microscope. *Optica*. 2015, vol. 2, no. 2, pp. 104. Available from DOI: 10.1364/optica.2.000104.

70. DRIGGERS, R. G. *Encyclopedia of Optical Engineering, Vol. 3*. 1st Ed. CRC Press, 2003. ISBN 9780824742522.

71. GUIZAR-SICAIROS, M.; THURMAN, S. T.; FIENUP, J. R. Efficient subpixel image registration algorithms. *Optics Letters*. 2008, vol. 33, no. 2, pp. 156. Available from DOI: 10.1364/ol.33.000156.

72. WALT, S. van der; SCHÖNBERGER, J. L.; NUNEZ-IGLESIAS, J.; BOULOGNE, F.; WARNER, J. D.; YAGER, N.; GOUILLART, E.; YU, T. scikit-image: image processing in Python. *PeerJ*. 2014, vol. 2, pp. e453. Available from DOI: 10.7717/peerj.453.

73. CALONDER, M.; LEPETIT, V.; STRECHA, C.; FUA, P. BRIEF: Binary Robust Independent Elementary Features. In: *Computer Vision – ECCV 2010*. Springer Berlin Heidelberg, 2010, pp. 778–792. Available from DOI: 10.1007/978-3-642-15561-1_56.

List of Figures

List of Tables